Department of Precision and Microsystems Engineering

Probing nanomotion and comparing antibiotic efficacy of a single *E. coli* bacterium on silicon and graphene

Stef Rodenhuis

Report no	:	2021.098
Coach	:	Ir. I.E. Roslon
Professor	:	Prof. dr. ir. F. Alijani
Specialisation	:	Engineering Dynamics
Type of report	:	Master of Science Thesis
Date	:	14 December 2021

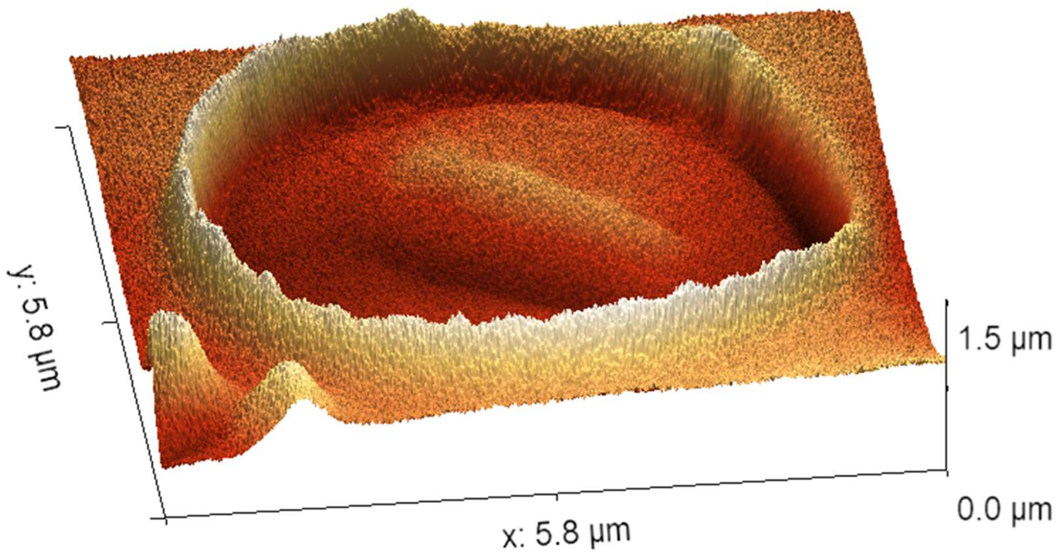

Delft University of Technology

Challenge the future

PROBING NANOMOTION AND COMPARING ANTIBIOTIC EFFICACY OF A SINGLE *E. COLI* BACTERIUM ON SILICON AND GRAPHENE

A thesis submitted to the Delft University of Technology in partial fulfillment
of the requirements for the degree of

Master of Science in Mechanical Engineering

by

Stef Rodenhuis

December 2021

Stef Rodenhuis: *Probing nanomotion and comparing antibiotic efficacy of a single E. coli bacterium on silicon and graphene* (2021)
An electronic version of this thesis is available at:
http://repository.tudelft.nl/.

The work in this thesis was made in the:

Group of Dynamics of Micro and Nanosystems (DMN)
Department of Precision and Microsystem Engineering (PME)
Faculty of Mechanical Engineering
Delft University of Technology

Thesis Committee:	Prof Dr. Cees Dekker Prof Dr. Farbod Alijani Prof Dr. Murali Ghatkesar Dr. Aleksandre Japaridze Ir. Irek Roslon
Supervisors:	Prof Dr. Farbod Alijani Prof Dr. Murali Ghatkesar Dr. Aleksandre Japaridze Ir. Irek Roslon

ABSTRACT

With the incline of multidrug resistant bacteria due to the widespread use of antibiotics, there has been an ongoing search for a faster and more effective method to test the effect of antibiotics on bacteria. With current techniques for investigation of bacterial resistance requiring a minimum of 24 hours to complete, a new technique is essential to reduce the widespread misuse of antibiotics worldwide. In the last decade, new methods of this so-called Antibiotic Susceptibility Testing have been on the rise, with an emphasis on the use of nanomechanical oscillators as highly sensitive sensors. In this thesis, a novel method based on cavities in silicon substrates is introduced to detect the motion of a single motile bacterium and is compared to a highly sensitive sensor based on graphene membranes. A sensor with bacteria attached will exhibit random oscillations and these oscillations can be monitored with a laser. The rigid silicon substrates are intuitively not showing any oscillations. Nonetheless, the motility of a bacterium can still be observed by the changes in the laser path. By using an interferometric setup and monitoring the fluctuation in the voltage signal, coming from bacterial biophysical processes, the Signal-to-Noise-Ratio is determined. The amplitude increase in the fluctuation of the signal is evidently correlated with the motility of the bacteria and is demonstrated to show an increasing trend when presented with a deterministically known topographical location of the bacteria. Subsequently, the ability to detect motile cells enables the capabilities of Antibiotic Susceptibility Testing on these substrates, by monitoring the change in motion of the bacteria prior and post exposure to an effective antibiotic. The motion change, due to antibiotic exposure, is observed to show a significant difference even for a single bacterium, which opens up opportunities for an elementary non-invasive monitoring tool based on silicon.

PREFACE

Here I am, writing my final words as a student at the university of technology in Delft. After years of studying in Delft, I feel ready to take on a new challenge and I am eager to apply the learned knowledge in practice as a engineer. Over the years I learned that discipline and hard work helps you to reach your goals, especially in the weird situation of working from home most of the year. Of course, I also learned that nobody can do it alone. Therefore, I would like to express my gratitude to everyone whom contributed directly or indirectly to my personal and academic growth.

Firstly, I would like to express my gratitude to my thesis supervisors for their guidance and endless cool discussions on a broad spectrum of topics. Foremost, I would like to thank my daily supervisor Irek for his positive energy, availability around the labs in times of need and his interest in my work.

I would also like to express my gratitude to the technical support staff for their help on designing and building experimental setups. Especially Spiridon for his help with my endless endeavour on 3D-printing designs.

I would like to thank the enthusiastic professors that taught me courses throughout the years to become a Mechanical Engineer.

I would like to thank all fellow students, for the interesting discussions on my projects and all the fun we had in those years.

I would like to thank Professor Cees Dekker for being part of my thesis committee.

Finally, I would like to thank my parents, friends and above all my girlfriend. Without your support, this would not have been possible.

Stef Rodenhuis

Delft, December 2021

CONTENTS

LIST OF FIGURES

LIST OF TABLES

ACRONYMS

AST	Antibiotic Susceptibility Testing	1
AMR	Antimicrobial Resistance	3
AFM	Atomic Force Microscopy	3
CVD	Chemical Vapour Deposition	21
FIB	Focused Ion Beam	21
LB	Lysogeny Broth	5
MEMS	Microelectromechanical Systems	6
MIC	Minimum Inhibitory Concentration	27
NEMS	Nanoelectromechanical Systems	6
PDMS	Polydimethylsiloxane	13
PMMA	Polymethyl Methacrylate	47
PPC	Polypropylene Carbonate	47
PSD	Power Spectrum Density	65
RMS	Root Mean Square	27
SEM	Scanning Electron Microscope	16
SNR	Signal-to-Noise-Ratio	26

1 INTRODUCTION

With the incline of multiresistant bacteria due to widespread use of antibiotics, there has been an ongoing search for a faster and more effective method to test antibiotics on bacteria [1]. Current techniques on detection of bacterial resistance requiring a minimum of 24 hours to complete, a new technique is essential to reduce the widespread misuse of antibiotics worldwide to combat the incline of multiresistant bacteria [2]. In the last decade a new method of this so called Antibiotic Susceptibility Testing (AST) has been on the rise, where it emphasises on the use of nanomechanical oscillators as highly sensitive sensors [3, 4]. Moreover, the door is opened to extraordinary materials for realizing novel sensors in this field of research, such as graphene, due to its unique mechanical properties[5]. Interestingly, due to the high sensitivity of these nanomechanical oscillators, they do not only restrict to multiresistant bacteria but could also have an enormous impact on cancer treatment therapies and outer space microbiology exploration[6, 7].

1.1 RESEARCH OBJECTIVE

In literature, there has been shown that in the field of AST already broad research has been conducted on the tools for these tests, its readout techniques, and materials for a few decades now (Appendix J). All these different tools and methods have their limitations. However, the nanomotion detection toolbox is the most promising in terms of sensitivity. Moreover, these different nanomechanical oscillators have their own limitations in the design (i.e. reusability, implementation for parallelization or high-throughput), raising the question of whether there can be a more elementary technique developed to perform AST. Recently, the study by Roslon et al. [8] shows that graphene membranes do properly function for AST and reach a distinguished performance in terms of sensitivity. This is the starting point of this research. The graphene membrane is one atom thick and so the process of fabrication and handling of these substrates during and before experiments are very fragile. The use of a flexible sensing device is leaving room for improvement since the failure of these membranes can be observed. Additionally, the graphene membranes can be used one time only. Conclusively, this brings into question whether a rigid device could be designed, with single-cell sensitivity, to eliminate the limitations of reusability and failure.

Another point of improvement, not only for the new design but also for the graphene membranes, is the need to obtain a fast($<$8 hours) and precise measurement, e.g. single bacteria sensitivity. Graphene is sensitive enough to notice a change in deflection caused by a single bacterium. However, still a high number of bacteria is used to deposit a bacterium on the membrane and uses sedimentation to adhere a bacterium on a membrane. Instead of using a cultured batch with a high number of bacteria (colony forming units), trapping a cell on a desired location would increase the motion detection and time consumption. Furthermore, the use of a rigid substrate increases the options for cell trapping, as the induced stresses have negligible effect compared to membranes.

1.2 OUTLOOK

This thesis is composed of multiple topics accounted through-out the year towards understanding, modelling or measuring of graphene transfers, cell trapping and/or nanomotion detection. The reader is firstly introduced to background information on the current AST in chapter Chapter 2 to emphasise the importance of a novel and rapid method. Also, the basic theory behind graphene membranes, cell trapping and the readout technique are discussed in the same chapter. Next, the different trapping techniques are evaluated in Chapter 3. This is followed by the probing of nanomotion using silicon in Chapter 4, which is compared to the highly sensitive graphene membranes. Finally, the results are discussed and concluded in Chapter 5 and recommendations for future research are given. The different topics combined into one device thereby demonstrate a simple yet elegant method for AST.

2 THEORY

This chapter discusses the background and theory of topics used throughout this thesis to gain a deeper understanding of the working principles. This section starts with a background on AST and the working principles behind the current techniques. Next, the concept of a harmonic oscillator is described, as the equations of motions are of paramount importance to understand the graphene membrane. This is followed by a short explanation on flows through a pore as described by different models and its resulting affect on graphene. Lastly, this chapter ends with the theory behind the reflection intensity of the interferometer and how to apply this to different materials/media.

2.1 ANTIBIOTIC SUSCEPTIBILITY TESTING

Antibiotics are the so-called ”wonder drugs” to combat microbes. For decades this wonder drug has been overused, not only in the therapeutic field but also in other industries such as agriculture[9]. Unaware of these dangers, the microbes have obtained resistance to antibiotics over the years, as shown in Figure 2.1. The variation of bacteria over the years and the vast misuse of antibiotics has created two fields of research as has been described by Belkum et al. [10]. These two fields are summarised in a schematic overview in Figure 2.2. The field of Antimicrobial Resistance (AMR) focuses on the prediction of antimicrobial resistance and is of paramount importance for the future antibiotics and its use. The field of AST focuses on the misuse of antibiotics and the importance of a new, rapid and affordable AST technique has prudently been implied. Moreover, the AST research is called phenotypic, which is a procedure whereby an antibiotic is added to the medium containing a certain bacteria. Figure 2.2 shows the classical methods of phenotypical research. However, to obtain a rapid method for AST, which is defined as being feasible within a normal 8 hours working shift, a new method is of great necessity[11].

2.1.1 Cantilevers

The most promising field is the sensing of living cells using cantilevers, or nanomechanical sensors, due to its already extensive field of research and favorable time consumption for AST [12, 13]. The nanomechanical sensors used in AST evolved from Atomic Force Microscopy (AFM), as they currently reach a distinguished performance in terms of sensitivity. This means that even thermal and Brownian motion will be detected by the cantilevers, therefore they will spontaneously oscillate[14]. These oscillations have a very low amplitude and hence the influence of a living sample can drastically been seen. The nanomotion of bacteria on the nanomechanical oscillators can be measured either in the dynamic or in the static mode.

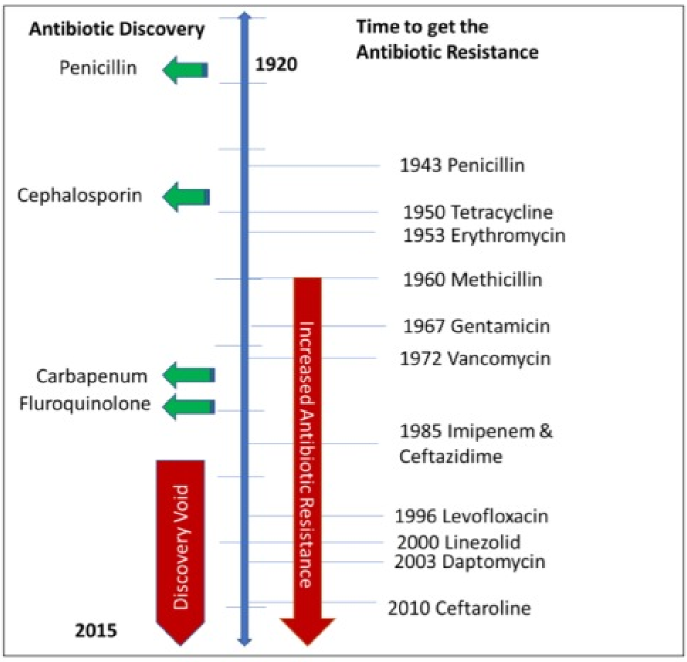

Figure 2.1: A graphical representation of onset of anitbiotic resistance versus time to get antibiotic resistance. Figure reproduced from Zaman et al. [9]

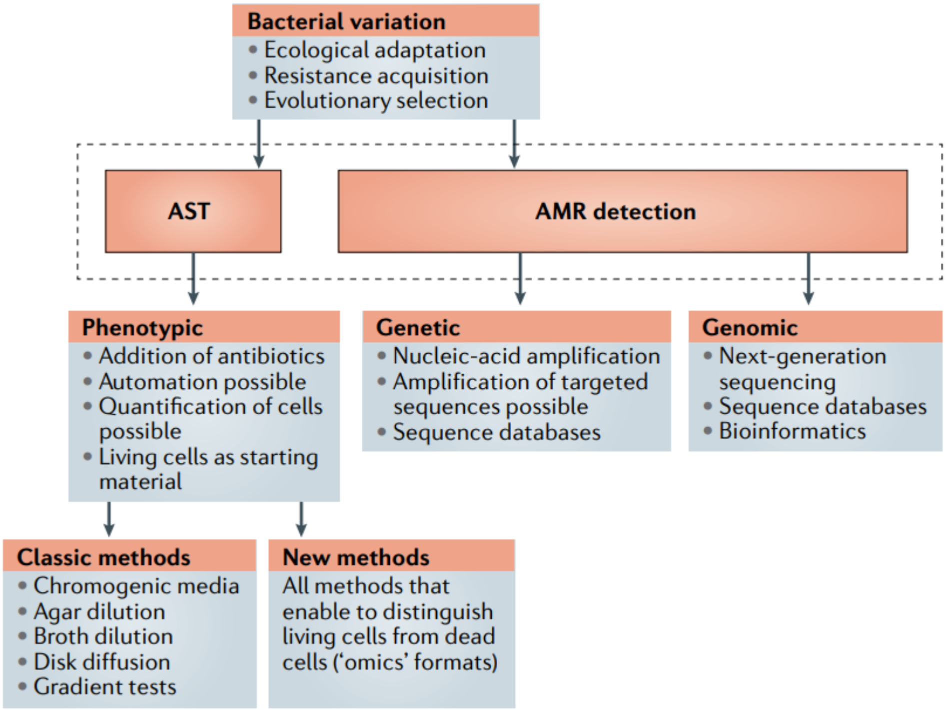

Figure 2.2: Schematic overview of antimicrobial susceptibility testing and antimicrobial resistance detection methods. Figure reproduced from Belkum et al. [10].

In the dynamic mode, the cantilever is driven at its resonance frequency. Note that there will be a more in depth discussion on this topic in the next section, as the resonance frequency is of paramount importance for the characterisation and understanding of the membranes. As soon as a bacterium is attached to this cantilever, there will be a shift in resonance frequency due to the added mass. In this mode the sensitivity of the performance depends on the resonance frequency and the quality factor, which depends on the sensing medium. Meaning that the sensing medium can strongly influence the dynamics of the cantilever (e.g. viscous damping [15]). Due its simplicity the cantilever can be modelled as a harmonic oscillator and the frequency can be calculated as follows:

$$f = \frac{1}{2\pi}\sqrt{\frac{k}{m}} \tag{2.1}$$

where k is the cantilever spring constant and m the effective mass.

In the static mode a bacterium attaches to the surface of the nanomechanical sensor and the deflection can be derived from the change in the surface stress, of course being either compressive or tensile. The surface stress in caused by interaction between the cell and the cantilever i.e. electrostatic, entropy and more [16]. In the static mode the sensing medium has a negligible influence on the measurement and hence is preferable when working in a liquid environment. The surface stress can be described by Stoney's equation[17]:

$$\Delta\sigma = \frac{Et^2}{3(1-\nu)L^2}\Delta z \tag{2.2}$$

where E is the Young's modulus, t the thickness of the cantilever, ν the Poisson coefficient and L the length of the cantilever.

2.1.2 Nanomotion detection

Extensively, one can say a third mode is present based on the nanomotion of bacteria. This approach does not focus on the deflection due to surface stress or on the frequency shift due to change of mass but merely on the amplitude increase of the oscillations due to biophysical processes. After functionalizing (changing the surface charge) the cantilever, resulting in bacteria or other living cells, adhering to the nanomechanical oscillators, the amplitude of the oscillations increase vividly. Moreover, nanomechanical sensors convert the biological motion, which mainly comes from metabolism, into mechanical motion [18]. This motion can be measured, including the exposure to antibiotics, within 60 minutes after adding the sample with the bacteria. An exemplary figure is shown in Figure 2.3, where the difference in motion amplitude can clearly be noted[19]. In panels a-a′ the fluctuation in nanomechanical motion is due to the living bacteria on the cantilever. Next, in panels b-b′ Lysogeny Broth (LB) has been added, which is a growth medium and the motion amplitude increases drastically due to the increasing metabolism. In panels c-c′ two different kinds of antibiotics have been added to the bacteria. The change in motion amplitude suggest that the bacteria has been killed by ampicilline (top panel) and not by kanamycin (lower pannel). Finally, this hypotheses was tested by adding again the growth media, confirming the previous assumptions as can be seen in the change in motion amplitude.

The field of AST has been under a tremendous development over the last few decades. The demand for a rapid AST due to the misuse of antibiotics and the variation of bacteria is forcing this rapid development. Though there are many fields or tools applicable and many methods have been proposed, all lack either affordability, high throughput or rapid AST.

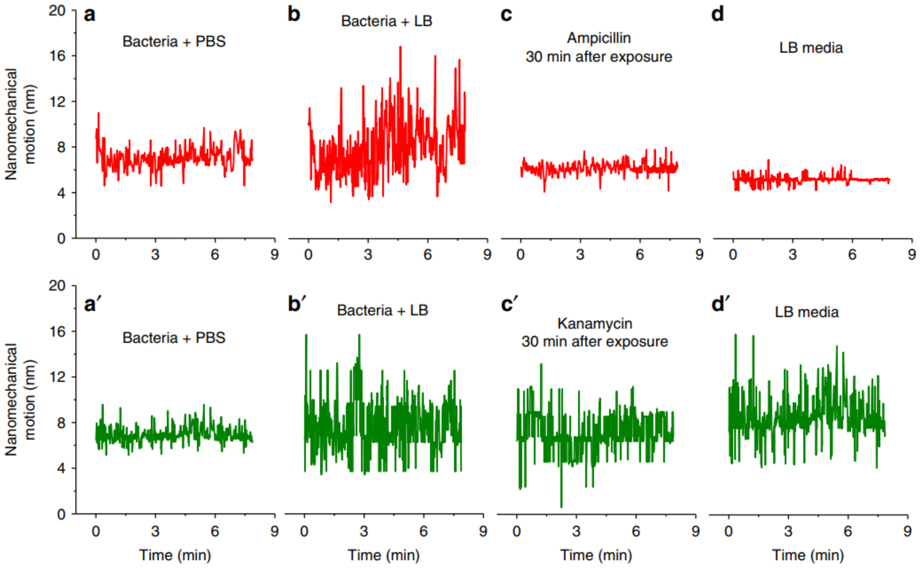

Figure 2.3: Nanomechanical motion shows bacterial susceptibility to ampicillin (upper panel) and kanamycin (lower pannel). Figure reproduced from Etayash et al. [20]
.

The cantilever or nanomotion toolbox has a interesting stance in terms of the most important aspect: rapid measurements and therefore is favorable. However, the current state-of-the-art often needs to have a high dose of bacteria, which in practise needs culturing of cells prior to the experiments, resulting in an increasing time duration. Also, to obtain multiple measurements an array of cantilevers is needed, which is rather difficult to implement and quite space-consuming. The current state-of-the-art AST techniques show there is optimistic perspective for a rapid AST, when not merely focusing on one toolbox. There has been shown that there is big room for improvement not only in a hybrid of the toolboxes but also in the material and design of the nanomechnical oscillator.

2.2 GRAPHENE NANODRUMS

The unique mechanical, electrical and optical properties of graphene, a single-atom layer of graphite, makes them promising for realizing novel sensors [21]. Though graphene is one layer of carbon atoms, it is the strongest material known, with its Young's Modulus and tensile strength being around 1 TPa and 100-130 GPa, respectively[22, 23]. These astonishing characteristics have been utilized in the field of Nanoelectromechanical Systems (NEMS) and Microelectromechanical Systems (MEMS) and can be found in readily available applications such as pressure sensors [24], biosensors [25] and photo-detectors [26].

2.2.1 Equation of motion

The nanodrum is equivalent to a regular percussion drum but on nanoscale. The theory behind a nanodrum can be obtained from the classical problem in mechanics describing the motion of a mass on a spring. When the mass is set in motion it will move back and forth, creating a repeating motion. This motion is called an oscillation. This oscillation is due to the force exerted by the spring pulling the mass back to its starting position. Before the mass m is set to motion, the mass is at rest at its so-called equilibrium position and the displacement between the position of the mass after exerting a force and this equilibrium position is z. The relation between the extering force F, the displacement z and the spring stiffness k was first described by Hooke's law in the late 1600's[27]. By applying the well-known Newton's second law of motion, one can obtain[28]:

$$\Sigma F_{mass} = m\frac{d^2z}{dt^2} + kz$$

This equation of motion shows no damping parameter, what would mean the motion would be indefinite. In reality the amplitude of the motion will slowly decay due to the damping constant c or moreover due to energy loss from the system. Taking into account the damping constant, which is related to the velocity of the mass, the system can be written as:

$$\Sigma F_{mass} = m\frac{d^2z}{dt^2} + c\frac{dz}{dt} + kz$$

These energy losses would mean there is no motion and the mass would be at equilibrium position. Thus to drive the system an external force is needed. The displacement of the mass on a spring can be finalised in the following formula:

$$\Sigma F_{ext}(t) = m\frac{d^2z}{dt^2} + c\frac{dz}{dt} + kz \tag{2.3}$$

This rather simple equation is of paramount importance in the current field of mechanics. Not only does it describe the motion of the mass on the spring but also extends to more difficult problems such as car suspensions and membranes. Hence this equation is also of paramount importance to the suspended graphene membranes.

2.2.2 Characterisation of the nanodrum

The solution to the motion, or trajectory of the mass, can be described by sinusoids and is therefore called an harmonic oscillator. In this thesis the displacement of the graphene membrane can be obtained through this formula. Figure 2.4 shows the classic model for deriving the equations of the system and its frequency response of a simple problem. The importance of the resonance peak ω_0 can not be stressed enough as it can be used to obtain the characteristics of the graphene membranes. The resonance frequency is related to the stiffness and mass of the system, similarly to the previous section, through:

$$\omega_0 = \sqrt{\frac{k}{m}}$$

The dynamics of the suspended graphene drums is dominated by the tension N and their fundamental resonance frequency f depends on the diameter D of the membrane. By using the theory for circular membranes the equation gives the following expression[29]:

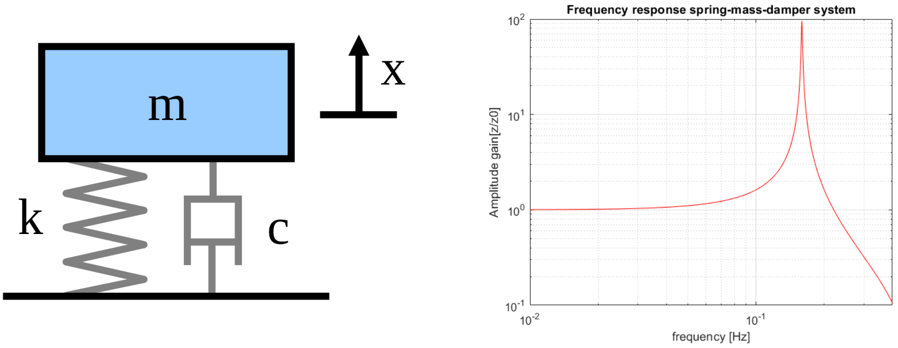

(a) The classic model of the system

(b) Frequency response of the classical model

Figure 2.4: The classical model for deriving the equations of motion for a mass-spring-damper system and its frequency response.

$$f = \frac{1}{2\pi}\sqrt{\frac{k}{m}} = \frac{2.4}{\pi D}\sqrt{\frac{N}{\rho t}} \tag{2.4}$$

where $k = \pi N$, ρ the mass density of graphene and t the thickness of graphene.

Moreover, the dynamic behavior of mechanical resonators can be characterized by two fundamental properties: the resonance frequency and dissipation (energy loss). The resonance frequency, as described above, is related to dissipation, as dissipation is commonly expressed as the inverse of the quality factor Q, or Q-factor. The Q-factor is a dimensionless parameter that describes how underdamped an oscillator is. Meaning that a higher Q indicates a lower rate of energy loss and the oscillations die out more slowly. An example of such an oscillation is shown in Figure 2.5, where one can see the oscillation dying out due to the damping. The definition of Q-factor is obtained from the frequency-to-bandwidth ratio of the oscillator:

$$Q = \frac{\omega_0}{\Delta\omega} \tag{2.5}$$

where the resonance peak is expressed in full bandwidth at half maximum (FBHM) of the magnitude $\Delta\omega = \omega_{right,HM} - \omega_{left,HM}$

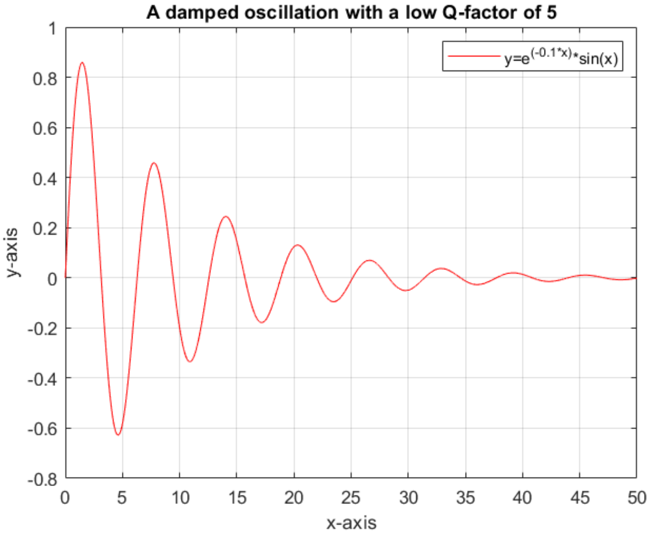

Figure 2.5: An example of a damped oscillation

2.3 MICROPOROUS SIEVING

To reduce the duration of the AST, single-cell isolation is of paramount importance. Not only do current methods need time consuming culturing of cells, increasing the number of bacteria exponentially, a bacteria has to adhere on top of a graphene nanodrum to observe the nanomotion. In this thesis the field of microfluidics has been evaluated to achieve the desired location for the bacteria, as sieving has shown to be a promising technique[30, 31].

This technique can best be elucidated by a flow through a small channel (or pore). A plane with small pores is subjected to a small negative pressure beneath the plane, initiating a flow through the pores. The suspension on top of the plane, containing the bacteria, is flowing through these pores until a bacterium is trapped on said pore. According to Swennenhuis et al. the probability for seeding single cells can be calculated using Poisson statistics [30]:

$$P = e^{-\lambda}\frac{\lambda^N}{N!} \tag{2.6}$$

where in case of gravity seeding λ is equal to the number of cells in the sample divided by the number of wells, or in case of self-seeding λ equals the number of cells present in the sample divided by the number of volume units of a single microwell and N is the number of cells per well. The figure can be seen in Figure 2.6 and is purely theoretical as the walls are assumed to be infinite thin.

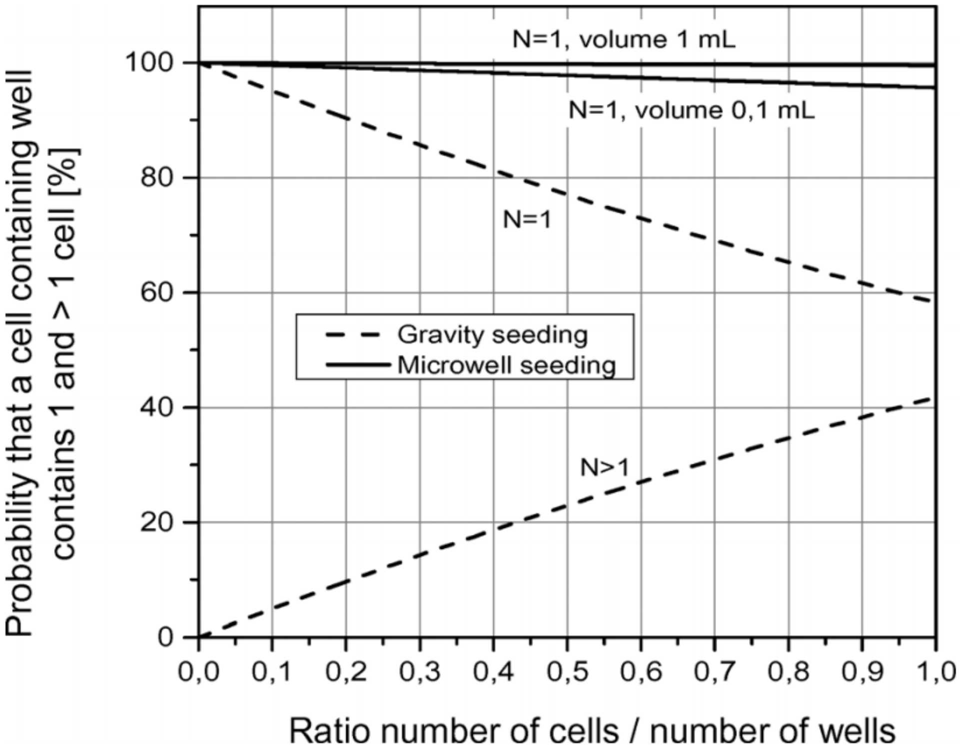

Figure 2.6: Probability for seeding single cells. The solid lines represent the probability for forced seeding for two sample volumes of 1 and 0.1mL. The dashed lines represent the probability for seeding by sedimentation. Figure reproduced from Schwennenhuis et al. [30].

2.3.1 Flow rate through pore

In this thesis the graphene membranes are used for the sieving and therefore no microwells are present in this situation. However, in both the situations the flow has to go through a small pore. Such a small pore is called an orifice and has been studied in the late 1800's by Sampson[32]. In this work Sampson published an analytical solution of the famous Navier-Stokes equations for a flow through a single pore in an infinite plane of zero thickness. Later on Weissburg showed the effects of a finite pore thickness by superposition of Sampson flow through an infinite pore and the well known Poiseuille flow inside the pore (seen as a small channel)[33]. This approximation neglects all inertial effects and approximates the flow as an incompressible Navier-Stokes flow. Sampson analysed the pressure drop across the pore by providing that the steady flow satisfies the continuity and Navier-stokes equations as follows:

$$\nabla \cdot v = 0 \qquad\qquad \mu \nabla^2 v - \nabla p = 0$$

where v and p represents the steady velocity and pressure field, respectively. The term $\nabla \cdot$ is called the divergence, which represents the volume density of the outward flux of a vector field from an infinitesimal volume around a given point. Next, Sampson applied the following boundary conditions:

- Uniform decaying of velocity at infinity.
- No-slip condition holds everywhere across the plane, except at the pore.
- The pressure approaches $-\infty$ and ∞ at opposite sides of the pore, initiating a flow.

This resulted in the relation between pressure drop Δp and flow rate q for a single pore found by Sampson, related through the dynamic viscosity μ and the radius r:

$$\frac{\Delta p}{q} = \frac{3\mu}{r^3} \tag{2.7}$$

Next, via the Poiseuille equation, which takes into account the thickness t of the plate, one can add a pressure drop associated with the Poiseuille flow along the pore for a low Reynolds number flow:

$$\Delta p = \frac{8 q \mu t}{\pi r^4}$$

And by superposition this results in the equation proposed by Weissberg:

$$\frac{\Delta p}{q} = \frac{3\mu}{r^3} + \frac{8\mu t}{\pi r^4} \tag{2.8}$$

Later on, Celebi et al. showed that the flow through a membrane can be approximated by a modified Sampson's formula [34]. This equation is given as:

$$Q = \frac{1}{6\mu} \frac{d^3}{\pi d^2} \Delta P \left(1 + 0.894 \kappa^{3/2}\right) \tag{2.9}$$

where d is the diameter of the aperture and κ the porosity of the membrane.
This equation is merely taking into account the porosity of the membrane instead of the thickness. Furthermore, this result is similar to the first part of Equation 2.8 and hence represents Sampsons model. This simple approximation has been experimentally validated by Celebi et al. for a single 50, 200 and 100nm pore in a graphene membrane, showing the relevance to this thesis. Both the models are plotted in Figure 2.7.

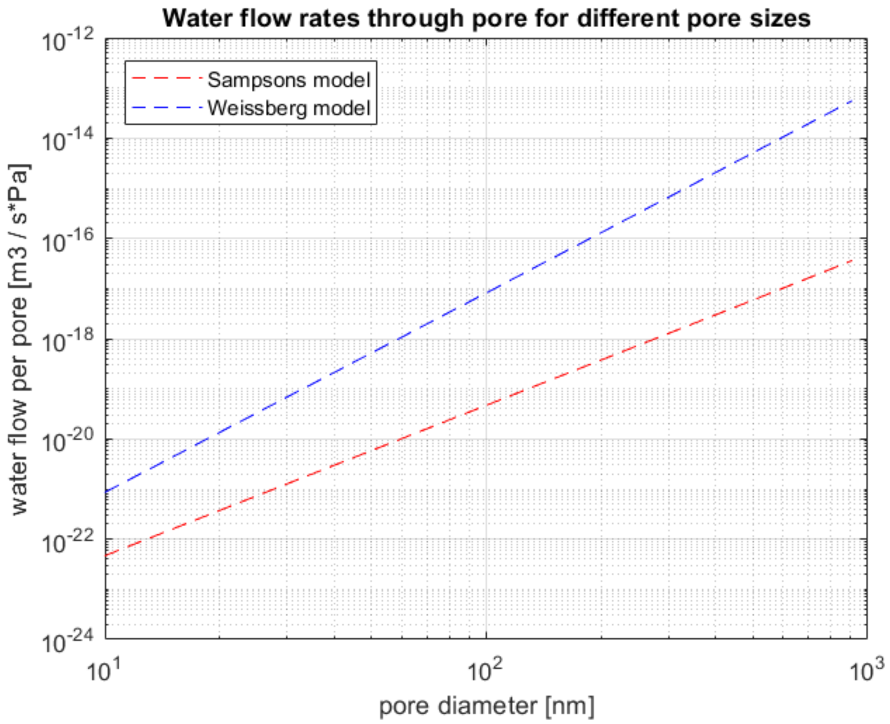

Figure 2.7: Water flow rates through a pore for different pore sizes according to Sampson's and Weissberg's model.

2.3.2 Pressure induced elongation

The pressure difference over the graphene membrane initiating the flow will also ensure an parabolic elongation to some extend, assuming the pressure is a well defined and uniform force on the membrane. This uniform force is balanced by the induced biaxial stress, σ, in the membrane. This has been shown by Vlassak et al. as the method called the bulge test[35]. This test can be used to measure in-plane mechanical properties of thin films such as the Young's Modulus, stress and Poisson's ratio. The relation between the pressure difference and stress can be described by the following equation:

$$\Delta P \cdot \pi R^2 = \sigma \cdot 2\pi R t \tag{2.10}$$

In the case that the deflection is small, meaning that $z \ll a$, the Pythagorean theorem can be used to express the radius of the curvature in terms of the radius of the membrane as:

$$R \approx \frac{a^2}{2z}$$

Substituting this equation into Equation 2.10 and expressing the surface tension as $N = \sigma t$, one would get:

$$N = \frac{\Delta P a^2}{4z} \tag{2.11}$$

When looking at the schematic of the bulge test (Figure 2.8) and taking into account the deflection is small as discussed above, the strain in the membrane is:

$$\epsilon = \frac{R\theta - a}{a} = \frac{a^2}{6R^2} = \frac{2z^2}{3a^2} \tag{2.12}$$

The biaxial strain of an isotropic plate according to the modified Hooke's law is:

$$\sigma = \frac{E}{1-\nu}\epsilon \tag{2.13}$$

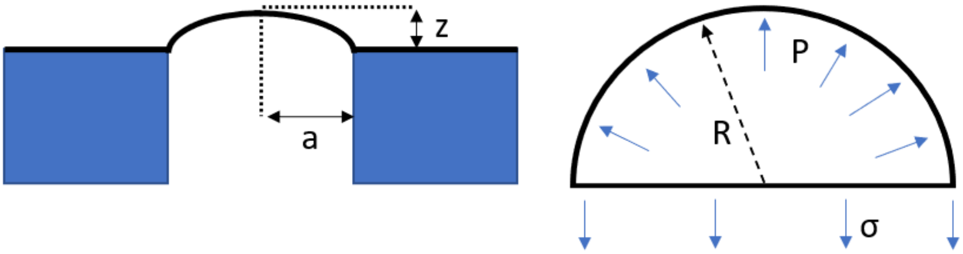

Figure 2.8: Schematic depiction of the stress due to pressure. The left side panel shows a membrane with radius a and deflection z. The right panel shows the curvature radius R due to the pressure and the resulting stress on the membrane σ.

Hence we obtain the pressure induced surface tension according to the biaxial elastic strain and Hooke's law as follows:

$$N_p = \frac{Et}{1-\nu}\epsilon = \frac{2Etz^2}{3a^2(1-\nu)} \tag{2.14}$$

The total surface tension N can be written as the total tension due to the pressure induces tension and the initial surface tension, which should be equal to the Equation 2.11.

$$N = N_0 + N_p = N_0 + \frac{2Etz^2}{3a^2(1-\nu)} = \frac{\Delta P a^2}{4z} \tag{2.15}$$

Note that the initial tension can be calculated using the resonance frequency explained in Section 2.2.2, the pressure can be varied during the experiments and as such the maximum displacement can be calculated as the only unknown variable.

2.4 READ-OUT

The motion of a graphene membrane has been commonly read-out using interferometry. This is a technique using superposition of waves to cause the phenomenon of interference. Meaning that two waves superpose to form a resultant wave of greater, lower, or the same amplitude [36]. This method is widely used in membrane motion and hence has been optimized in terms of the cavity beneath the suspended graphene. In the research of Davidovikj et al. the responsivity at the laser wavelength of $\lambda = 632.8nm$ for a range of graphene thicknesses has been maximized[37]. The reflectivity of the common devices used for graphene membrane measurements, consists of three different interfaces, which is schematically depicted in Figure 2.9. The formula for the responsivity through the different media can be represented accordingly using the described geometry as explained by Blake et al.[38]. We consider the case that normal light incidence from vacuum onto a trilayer of graphene, vacuum and silicon. The silicon layer is assumed to be semi-infinite. Also note that the materials are characterized by a complex refractive index, meaning that $\underline{n} = n + i\kappa$ due to the dependency on the wavelength. This is because if light moves through a medium, some parts will be attenuated, which can be taken into account in the refractive index by defining a complex part. The responsivity is as follows:

$$R = \left| \frac{r_1 + r_2 e^{-i\delta_1} + r_3 e^{-i\delta_2} + r_1 r_2 r_3 e^{-i(\delta_1+\delta_2)}}{1 + r_1 r_2 e^{-i\delta_2} + r_1 r_3 e^{-i(\delta_1+\delta_2)} + r_2 r_3 e^{-i\delta_2}} \right|^2 \tag{2.16}$$

Where

$$r_1 = \frac{n_0 - n_1}{n_0 + n_1},$$
$$r_2 = \frac{n_1 - n_2}{n_1 + n_2},$$
$$r_3 = \frac{n_2 - n_3}{n_2 + n_3}$$

are the refractive indices. δ_1 and δ_2 represent the acquired phase while traveling through the different media and can be calculated as following:

$$\delta_1 = \frac{2\pi n_1 N t_0}{\lambda},$$

$$\delta_2 = \frac{2\pi n_0 N z_0}{\lambda}$$

with N the number of layers of graphene, t_0 the thickness of a single layer, λ the wavelenght of the laser and z_0 the starting position of graphene. This formula for responsivity has been solved for the cavity depth z_0 by Davidovikj et al. and has shown that $z_0 = 285nm$ maximises the responsivity in the range between 1 and 30 layers of graphene[37]. Note that this is the starting point of the nanomotion detection in this thesis. From the graphene membranes, other methods for nanomotion detection are evaluated. Meaning that the media varies throughout measurements. From this model different responsivities can be checked for varying media e.g. Silicon, Polydimethylsiloxane (PDMS) and of course the bacterium. Also note that if one would use this approach on the nanomotion detection in combination with microporous sieving there will no longer be an optimal cavity filled with air but with the specific medium of the suspension, adding additional damping such as viscous damping. This will make the device less sensitive to nanomotion detection [39].

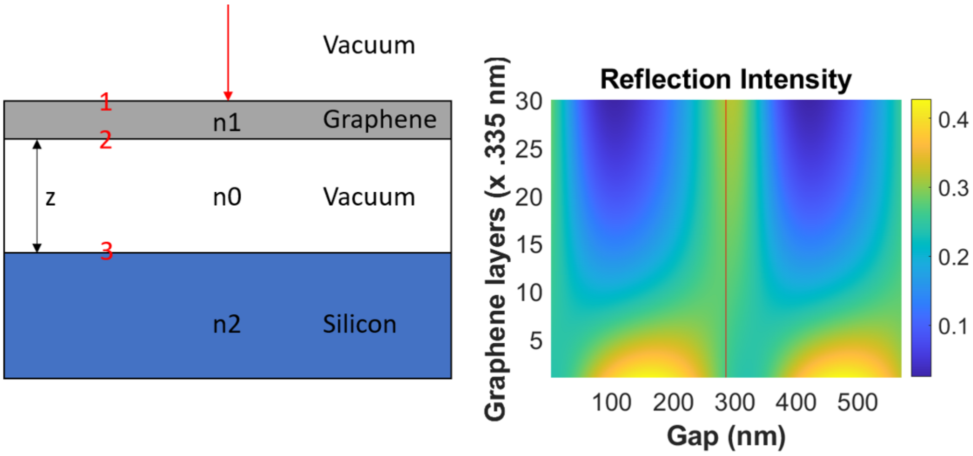

Figure 2.9: Schematic depiction of the three different interfaces (left panel) and its reflection intensity (right panel).

3 CELL TRAPPING

This chapter discusses a few methods aspired to achieve single-cell trapping. This thesis contains different kind of samples and thus requires different approaches for trapping e.g. the transfer of graphene will result in a flat surface leaving no room for topographical features. Firstly, the so-called capillary assembly method is described and discussed. Secondly, a very simple but effective method using sedimentation is evaluated. Lastly, this is followed by the sieving of particles on graphene. Note that for some situations particles are used to represent bacteria, due to safety reasons.

3.1 CAPILLARY ASSEMBLY

3.1.1 Working principle

The method of capillary assembly was firstly described by Malaquin et al., showing the influence of convective flow of the evaporation and the influence of temperature [40]. Later Flauraud et al. demonstrates that topographic features made by lithography on a solid substrate can deterministically direct the capillary assembly to attain control of position, orientation and interparticle distance at nanometer level [41]. The working principle of capillary assembly is based on three stages: insertion into the traps, resilience against the suspension front and drying of the suspension. In Figure 3.1 the working principle is shown schematically. The combined effect of geometrical confinement and capillary forces created when the meniscus is pinned on the topographic features can be used to deposit a single particle.

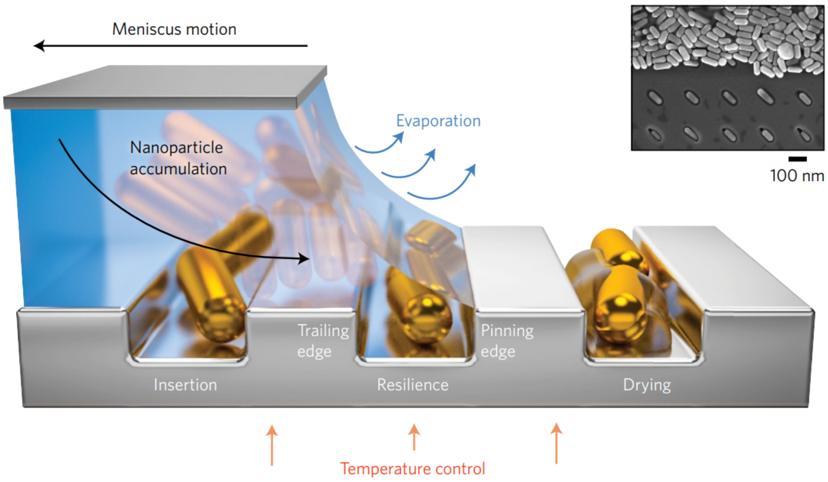

Figure 3.1: The working principle of the capillary assembly method with the three sequential stages. A suspension containing the particles is confined on a hydrophillic substrate containing traps and a top plate. The top plate is pulled across the substrate and the particles are accumulated at the edge of the suspension, as can be seen in the inset. The particles are contained in the traps due to the capillary forces and the evaporation, which is influenced by the temperature control. Figure reproduced from Flauraud et al. [41].

3.1.2 Method

The capillary assembly experiments were performed on a 5x5mm^2 Si substrate with circular cavities with a depth of 285nm and varying diameters and pitch that were etched in SiO_2. The substrate was hold in place using a vacuum pump and the top plate was controlled with a micro positioning stage, with a velocity of $\sim$2 um/s. The gap between the top plate and the substrate was 500μm and the temperature was controlled and set to 50°C during the experiments. The experiment was performed with 1.5μm polystyrene particles for three different concentrations, which were centrifuged twice for 10 minutes at 5000 rpm. A single droplet of 10μL was placed on the substrate. The three concentration of the experiments were $5 \cdot 10^6$, $5 \cdot 10^4$ and $5 \cdot 10^3$ parts/mL, respectively and were sonicated for 5 minutes prior to the experiments. The setup is shown in Figure 3.2.

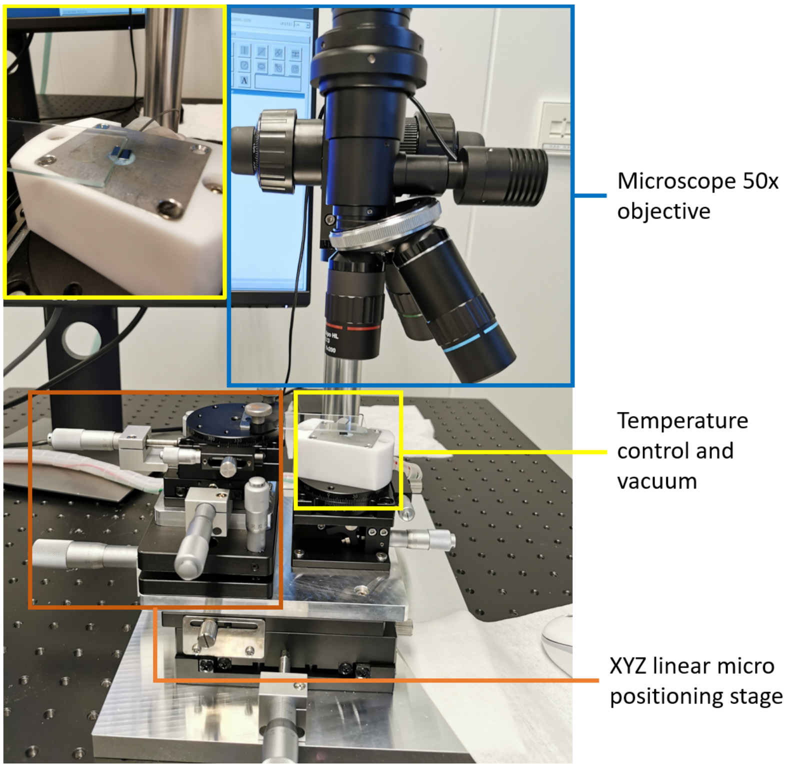

Figure 3.2: The experimental setup for capillary assembly. The three boxes represent the three main parts of the setup. The positioning stage is used for controlling the movement of the top plate. The microscope allows us to see the traps and particles during the experiments up to 50x zoom. The temperature and vacuum unit heats up the sample and holds it in place. The inset on the left top corner is showing a substrate and the top plate during an experiment.

3.1.3 Results

The experiments were evaluated for the three concentrations. Two Scanning Electron Microscope (SEM) images can be found in Figure 3.3. Note that the dimensions differ throughout the figures, as they are mainly shown to discuss the affect of different concentrations. The result of the three experiments are summarised below:

1. Concentration of $5 \cdot 10^3$ parts/mL (number of particles<number of cavities):
    - All particles were found to be trapped in a cavity (100%).
    - Every cavity (even up to 6 times the diameter of a particle) contained only one or no particle.

2. Concentration of $5 \cdot 10^4$ parts/mL (number of particles≈number of cavities):
    - Most particles were found to be trapped in a cavity ($> 95\%$).
    - Cavities of same or doubled diameter as the particles were found to be filled with one particle ($> 95\%$).
    - Cavities of a greater diameter would contain multiple particles ($\sim 50\%$)
3. Concentration of $5 \cdot 10^6$ parts/mL (number of particles>number of cavities):
    - Most cavities were found to contain a particle ($> 95\%$).
    - All cavities of the same diameter as the particles were found to be filled with one particle (100%).
    - Cavities of a greater diameter would contain multiple particles ($> 95\%$)

3.1.4 Conclusion and discussion

The capillary assembly method can be used to attain control of position, orientation and interparticle distance, deterministically. From the experiments it can be concluded that the placement of a single particle is clearly feasible using topographic features. The cavities with dimensions smaller than 2 particles would only contain a single particle. Moreover, for lower concentration of particles even the cavities with a dimension of more than 5 times the size of the particle would still contain a single particle because of the evenly distributed particles in the suspension due to the prior step of sonication. The higher concentration of particles would increase the chance of adhesion between the particles and this was optically visible in the cavities of a greater dimension than the particles.

This method demonstrates an approach that could achieve single bacterium trapping, as the capillary force is strong enough to keep the bacterium in the cavity[41]. Also, note that bacteria like to stay at the surface due to surface roughness, which is more likely to be present at the edges of the cavities (see Section 3.2). However, regressing to the implementation of this method for nanomotion measuring there are some downfalls. The drying of bacteria is far from optimal, as the drying causes a drop in survival rate of bacteria like the *E. coli*, especially in fast drying [42]. Furthermore, this experiment is performed in an open environment, which not ideal when working with bacteria. Moreover, implementing this procedure prior to nanomotion measurement would also mean moving the substrate in an open environment.

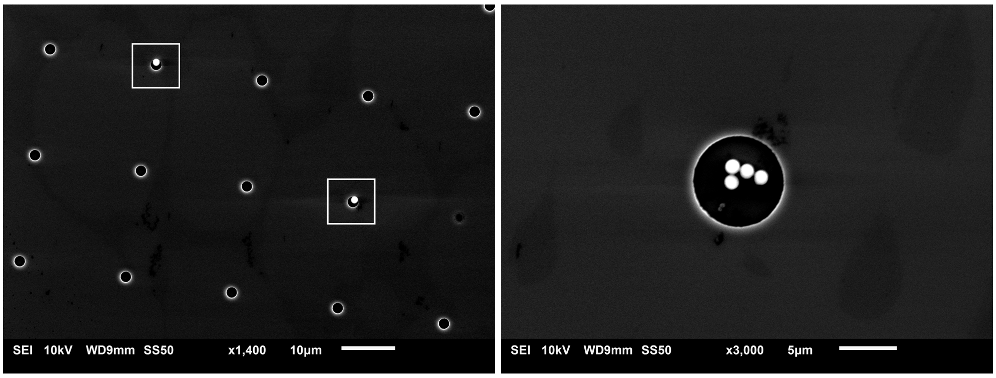

(a) An array of 2 μm cavities. The white boxes show a particle in a cavity.

(b) A 8 μm cavity showing multiple particles in the cavity.

Figure 3.3: Two SEM images of the capillary assembly method.

3.2 CELL SEDIMENTATION

3.2.1 Working principle

Cell sedimentation or gravitational sieving is a simple, yet elegant method to trap cells in a topographic feature. The free sedimentation of bacteria is in general agreement with the Stokes' law and the settling time can hence be calculated [43]. The working principle is elementary and is shown in Figure 3.4 . Bacteria slowly move down towards the substrate due to the gravitational force pulling them down and will then move across the surface of the substrate. The bacteria will swim into a cavity and stay there if the cavity is deeper than the diameter (height) of the bacterium. This is also noted for cavities with less depth, as bacteria like to adhere to rougher surfaces [44]. If you have a low pitch between cavities, one could choose to functionalize the surface. Changing the surface charge density will ensure the adhesion of bacteria to the substrate [45]. Note that it will adhere also on the surface next to the cavities. A refined solution to this problem is adding the functionalizing substance after sedimentation to keep them in the cavities, if one would have to move the substrate.

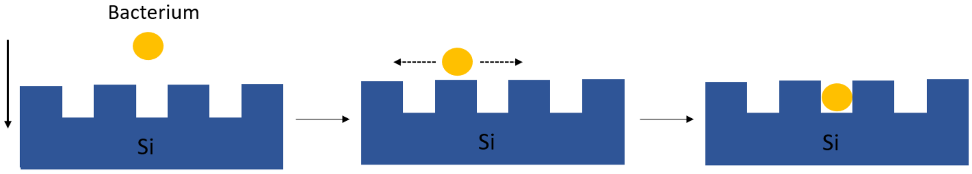

Figure 3.4: Schematic depiction of cell sedimentation. In the first panel the bacterium is moving freely in the suspension and is simultaneously pulled down to the substrate by gravity (denoted by the arrow). In the second panel the bacterium is on the surface of the substrate and will move parallel to the surface. Finally, the bacteria will swim into one of the cavities due to gravity and remain here.

3.2.2 Method

The experiments were again performed on the 5x5mm^2 Si substrate with circular cavities and a depth of 285nm that were etched in SiO_2, and on a substrate with similar circular cavities but with an depth of 1.5μm fabricated in PDMS. The fabrication of the PDMS substrate can be found in Appendix E. The substrates have been treated with acetone sonication for 5 minutes + isopropyl alcohol sonication for 5 minutes, followed by 5 min of O_2 cleaning in the plasma on 80W. After the PDMS cavities are fabricated the substrate has to be O_2 cleaned for 30 seconds on 80W again, to ensure hydrophilicity. The *E. coli* cells are grown in LB media overnight at 30°C. The next day before performing experiment, the culture was refreshed with a 1:100 volume for 2.5 hours on fresh LB medium at 30°C. To determine the amount of bacteria present in the suspension (cells/ml), the optical density can be measured. The OD_{600} measures the optical density at a wavelength of 600nm. The suspension used in experiments reach $OD_{600} = 0.2 - 0.3$. If the experiments need bacteria to adhere to the surface, the surface has to be functionalised by adding APTES to the suspension with a final concentration of 0.1% APTES before adding the suspension to the substrate.

3.2.3 Results

The cell trapping by sedimentation is difficult to validate optically. In Figure 3.5 two optical images are shown. The bacteria are still visible with the optical microscope (500x zoom). However, when enhancing to a greater magnification the images become blurry due to the refraction of the light through the growth medium. When enabling phase contrast the tracking of a bacterium becomes realizable. Nonetheless, tracking these bacteria would take an enormous amount of time when doing manually. Therefore the results were not obtained by optical images, but with an optical laser in an automated fashion. These results will be discussed separately in Chapter 4 for cavities with and without surface functionalisation on the Si/SiO_2 substrates and in Appendix F for the PDMS cavities.

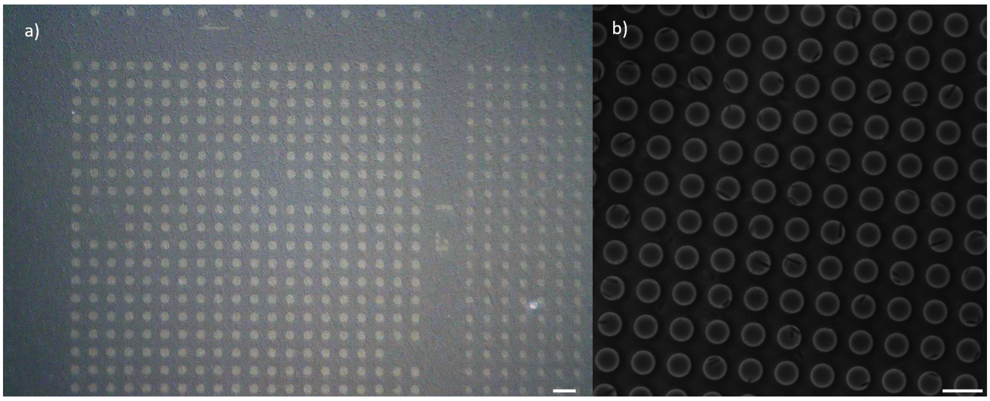

Figure 3.5: Optical images of cell trapping by sedimentation. a) Shows an optical image made with a Keyence VHS-7000. The black rod-shaped features are bacteria. b) A phase contrast image to enhance the visibility of the bacteria. In both images the white scale bar is $10\mu m$.

3.2.4 Conclusion and discussion

This method presents a simple and effective way to trap cells in topographic features, without using an additional setup or effort (such as the capillary method). Single *E. coli* bacterium were observed in the cavities with and without the surface functionalisation. Also, the images and measurements clearly show that the bacteria like to move around on the surface; even on just silicon without any topographic features, which opens the door to other exquisite and exceptional topographic features to trap the bacteria, e.g. a maze. In terms of these particular features, the substrates with the etched Si/SiO_2 cavities of $285nm$ have bacteria leaving the cavities at some extend without the functionalisation. The height of an *E. coli* is about $850nm$ and hence is larger than the depth of the cavity. Whilst the height of the PDMS cavities is significantly more than that of the bacteria ($1500nm$) this phenomena was observed to a lesser extend, implying that the increase of the cavity height will increase the trapping duration. Finally, for the larger cavities (diameter cavtity>length bacterium), the swimming on the righ-hand side has been noticed as explained by Diluzio et al. [46]. Besides this being another door to designing a topographic feature trapping the bacterium , this also causes a clockwise motion in the circular cavities (see Appendix F). Demonstratively does this phenomena also open doors to cell synchronisation.

3.3 SIEVING

3.3.1 Working principle

Sieving of particles is widely used method to obtain a single particle on a specific location. Throughout the years this method has also been applied to mammalian cells and on rigid surfaces [30, 31]. In this work the method has been tested on graphene membranes with small pores and bacteria, which are smaller than mammalian cells. The working principle of the sieving is shown in Figure 3.6. The *E. coli* bacteria is rod shaped and has a length and diameter of about 1.5 and 1μm, respectively. The pore has be smaller to make sure the bacterium is trapped. Considering we are talking about pore diameter in the order of 500nm a COMSOL simulation was run to ensure the pressure can overcome the capillary force and a flow is initiated. The simulation is shown in Figure 3.7.

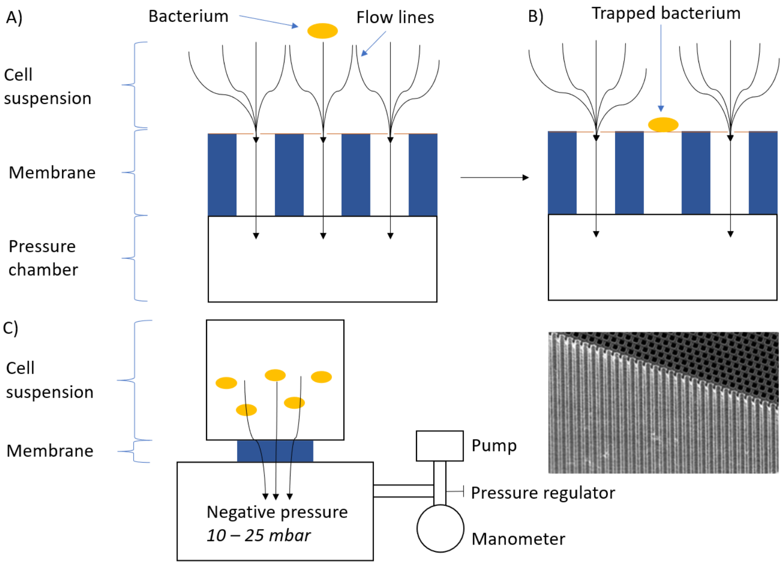

Figure 3.6: (A-B) Show a schematic depiction of the sieving working principle. A small negative pressure initiates a flow through the membrane and the suspension with the bacteria flows through the pores. The flow through a pore will be blocked as soon as a cell is trapped on the pore. C) Shows a schematic of the experimental setup and the inset is an intersection view of the membrane, figure reproduced from SmartMembranes.

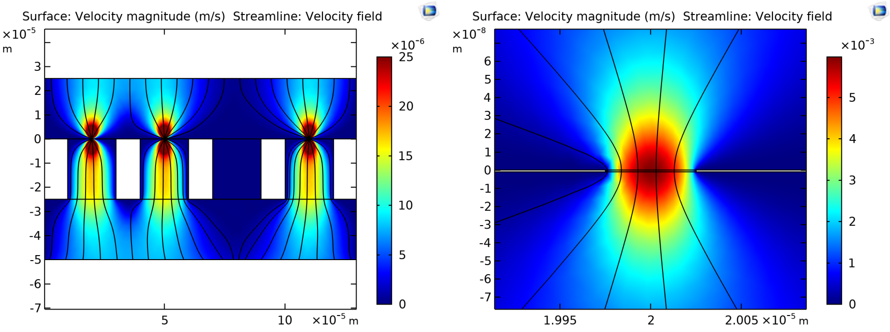

(a) Velocity magnitude across the membrane. **(b)** Zoomed in view around a pore.

Figure 3.7: A 2D COMSOL simulation of the velocity magnitude through the membrane. The black lines represent the flow lines. The third channel shows no flow, as it is simulated to be blocked by a trapped bacterium.

3.3.2 Method

The experiments were performed on a 10x10mm^2 membrane with square cavities of 4.5μm and a thickness of 311μm. The experiments were firstly performed on a empty membrane and later performed on a membrane covered with graphene. For the different graphene transfers see Appendix C. The pores were drilled with a Focused Ion Beam (FIB) by exposing to ion bombardment to produce porous membranes (Figure 3.8). We used GA-based FIB to perforate orifices of $\sim 500nm$ with low exposure doses of $5 \cdot 10^{-5} pA/nm^2$ to enable fast and precise perforation, similarly to literature[34, 47]. The effect of a pore on the graphene sensitivity can be found in Appendix D. The membrane was placed in the setup and experiments were performed with varying pressures (up to 1 bar). The experimental setup can be found in Appendix A. For the step-by-step procedure see Appendix B. The particles used for sieving on the membrane are 10μm black polystyrene microspheres and for the bacterial sieving the same cells as described in Section 3.2 are used.

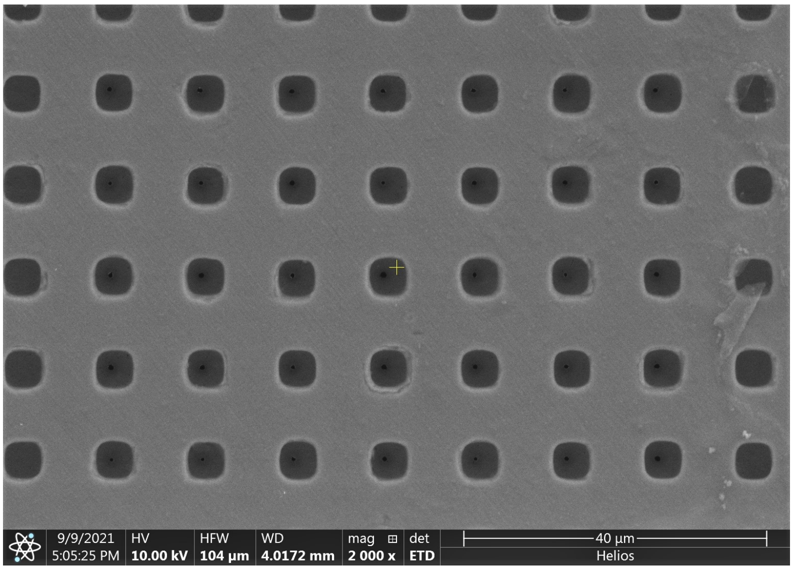

Figure 3.8: SEM image of a membrane covered with double-layer graphene. The image shows an array of 5x7 membranes with $\sim 500nm$ pores drilled using FIB.

3.3.3 Results

The first experiments were performed on 50 μm orifices with 100 μm particles. These experiments were repeated for smaller dimensions if found to be successful. Successful here connotes the trapping of a particle on the orifice. The last step before the graphene experiments was found to be successful and was in the order of 4μm orifices. Next, the experiments were performed on different graphene membranes. Most of the experiments showed a drastic increase in flow rate due to broken membranes, which can be seen in Figure 3.9a and Figure 3.9b. For this specific case the jump in flow rate was already noticeable at a pressure of 200 mbar, whilst Celebi et al. could apply up to 2 bar of pressure, without breaking the membranes[34]. Even if the membranes would stay intact, there are still parts on the membranes, which failed during the Chemical Vapour Deposition (CVD) graphene transfer as can be seen in Figure 3.9c. This creates unwanted flow directions. In addition, the edges of the graphene flakes would sometimes roll up towards the pore due to the flow across the plane, eventually blocking the pores.

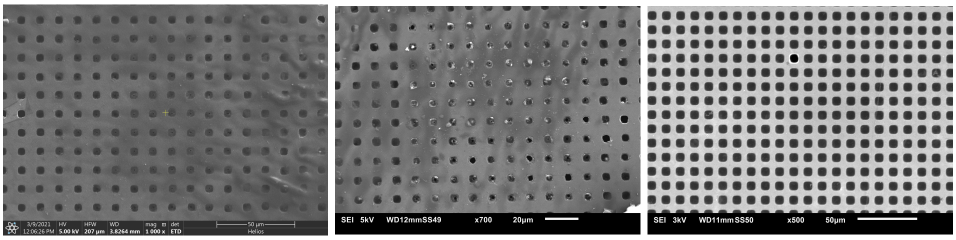

(a) Graphene membranes prior to sieving. **(b)** The same membranes post sieving. **(c)** A broken membrane after the graphene transfer.

Figure 3.9: SEM images of broken graphene drums on different membranes. (a-b) SEM images of the same membranes with pores prior and post sieving, respectively. The SEM image clearly shows broken membranes post sieving. c) Shows a broken membrane, causing the flow to be directed away from the pores.

To overcome this problem, different substrates were used to test the feasibility of this principle. A silicon substrate with a single hole of $\sim 20x20\mu m^2$ was covered with either CVD or exfoliated graphene. Different pore distributions were created using FIB and can be seen in Figure 3.10. The same experiments were performed on these substrates. The result of the flow rates can be seen in Figure 3.11. The result is obtained from 3 measurements for a duration of 24 hours for 6 pores of 500nm at 150 mbar. The flow rate was found to be $42 \pm 0.125\mu L/day$, which is $5.4 \cdot 10^{-18} \pm 1.6 \cdot 10^{-20} m^3/s \cdot Pa$. The experimental results agree with the results of the models, simulation and literature. Though a flow was initiated through the pores, unfortunately no cell trapping could be achieved using these substrates, which will be discussed next.

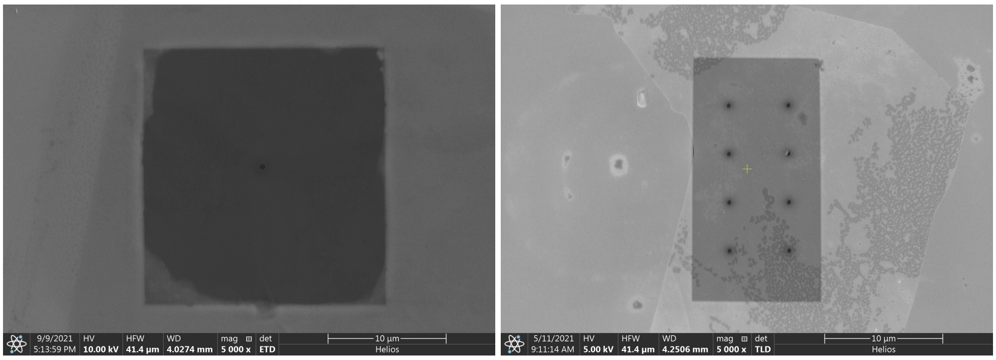

(a) A single pore in multilayer graphene. **(b)** Multiple pores in multilayer graphene.

Figure 3.10: The silicon substrates with a single through hole covered with multi-layer graphene.

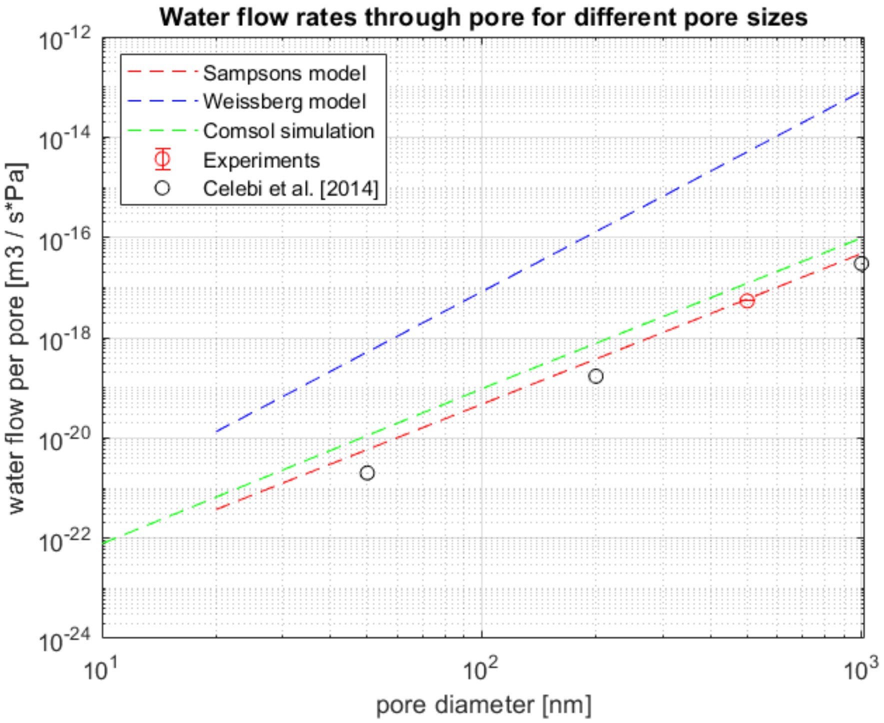

Figure 3.11: The flow rate for different pore sizes according to different models, simulation and literature. The experimental results agree with Sampson's model, simulation and literature.

3.3.4 Conclusion and discussion

The sieving of particles and even of large cells is shown to be a well researched topic in literature. The information found was helpful to create a step-by-step sieving procedure during this thesis. This resulted in successfully sieving particles, which was expected due to the already available research.

Furthermore, the results of the sieving of bacteria was unfortunately a big setback in the improvement of bacterial motion sensing with graphene. Trapping a single bacterium on a graphene membrane would increase the time duration of AST enormously, as only a single bacterium would be needed (or multiple to create a proper database) instead of the $OD_{600} = 0.2 - 0.3$ used in gravitational sieving. A flow was initiated through the graphene membrane for demiwater and so conclusively, one could say the failure mode of this method is to be found in either the bacteria or the medium. Whilst the LB medium contains nutrition's for the bacteria, such as salts (NaCl) and Glucose ($C_6H_{12}O_6$), the effect of these on clogging of the pore has yet to be analysed, but has not been done due to the lack of time. Besides the medium, the other failure mode could be found in the bacteria. Bacteria contain flagella for propulsion, which are even longer than the bacteria themselves. It has been found that in stressful situations (possibly the applied pressure) certain cells tend to shed their flagella, which could clog the pore of the membrane [48]. A straightforward way to test this hypothesis would be to stain the flagella and optically track them with a fluorescence microscope during sieving [49].

3.4 CONCLUSION AND DISCUSSION

In this chapter three different techniques were evaluated as possible methods to attain a single-cell at a topographical location (i.e. cavities and graphene membranes). Not only do the techniques require different substrates, they all have their pros and cons, which were already discussed in the individual sections. Additionally, the most important feature (single-cell placement) was found to be possible for the capillary assembly and sedimentation method but both methods have some downfalls.

The capillary assembly resulted in single particle placement if using the correct topographical feature or concentration. Correct connotes the size of the feature is smaller than the particle size or the number of particles is less than the number of features. The capillary assembly was however using three main stages: insertion in the traps, resilience against the suspension front and the drying of the suspension. The last step in this procedure, the fast drying, decreases the survival rate of bacteria, which is again not favorable for the time consumption as a higher OD is needed. Moreover, the reasoning behind these experiments was the nanomotion experiments and subsequently the AST. These experiments are performed in a liquid environment, meaning that even if the bacteria survive, the substrate has to be filled with a growth medium. Indisputably, this would raise the question on how to keep the cell in the cavity.

Though the sedimentation method was resulting in single-cell placement, to decrease the duration of sedimentation a high OD was essential. This means that again it could not be classified as a rapid AST, as this was determined to be within a working shift of 8 hours. One additional topic that was evaluated in this thesis, but not mentioned in this work, was the use of a high-end printer (Pixdro LP-50). Though the resolution of the printer was not high enough to accurately place a droplet on top of a cavity or membrane, in combination with a funnel, the sedimentation/printer method was a very encouraging combination. This means a single-cell could be placed near to the desired location and gravity would ensure the final placement. This method was not analysed beyond this step, as the printer broke down for a couple of months, but is nevertheless a supplemental approach to take into consideration to speed up to process.

The method of sieving was in my personal impression, the most promising technique prior to the start of the experiments due to the already extensive research in this field of work and even found successful for mammalian cells. The COMSOL simulations and the experimental results of a flow of demineralised water through pores, were certainly optimistic steps in the beginning of the procedure. However, sieving of bacteria was not found to be successful. This was most likely due to medium or the flagella. The group of Prof. Dr. D. Tam at the department of Process and Energy at Delft University of Technology is working on cell synchronisation of algae using the same sieving technique on silicon pores. These pores are a factor of 10 bigger than the pores in graphene and only 25% could successfully be trapped. Even here the pores are getting clogged by the shedding of the flagella. This might emphasises the failure mode for even smaller pores.

4 PROBING NANOMOTION

This chapter displays the results of the nanomotion detection of bacteria on different substrates and topographical feature, and discusses the relation between the different experiments. Additionally, the different substrates are exposed to a known to be effective antibiotic (Chloramphenicol) to evaluate the antibiotic susceptibility of the *E. coli* bacteria on these substrates. The method of sedimentation from Chapter 3 is used to obtain rapid measurements (from adding the suspension to the substrate, to the start of the interferometric measurements $<$30min) and to ensure bacteria are at the desired location. Note that this chapter is written in the IEEE format and therefore might have a small repetitive part in the abstract and introduction.

ABSTRACT

Nanomotion detection of bacteria has received considerable attention in the field of antibiotic susceptibility testing. However, single-cell sensitivity, rapid tests or reusability have been the limiting factor to produce a promising antibiotic susceptibility test. Here a novel method based on cavities in silicon substrates is introduced to detect the motion of a single motile bacterium and is compared to a highly sensitive sensor based on graphene membranes. By using an interferometric setup and monitoring the fluctuation in the voltage signal, due to bacterial biophysical processes, the Signal-to-Noise-Ratio is determined. The Signal-to-Noise-Ratio is demonstrated to show an increasing trend when presented with a deterministically known topographical location of the bacteria. Subsequently, the ability to detect motile cells enables the capabilities of Antibiotic Susceptibility Testing on these substrates, by monitoring the change in motion of the bacteria prior and post exposure to an effective antibiotic. The motion change, due to antibiotic exposure, is observed to show a significant difference even for a single bacterium, which opens up opportunities for an elementary non-invasive monitoring tool based on silicon.

4.1 INTRODUCTION

In the last decade, cantilevers have become increasingly popular in the field of AST. Evolving from AFM, into the dynamical and statical response of living cells on the cantilever, and even into nanomotion detection of living cells[3, 14, 19]. The nanomotion detection of bacteria on classical cantilevers opened doors to extraordinary materials for flexible nanomechanical sensors, such as suspended graphene membranes[8]. Flexible MEMS like cantilevers and graphene membranes have some limitations: they may have low reusability (one use only or higher failure rate), need multiple cells for nanomotion detection, or are difficult to implement in in an array for parallelization (space limitations on the substrate or setup). Therefore an elementary, reusable and rigid device, with single-cell sensitivity, would reduce these effects.

Here, we present a more elementary technique based on the reflectivity of silicon and the use of cavities to show single-cell sensitivity. This technique allows us to sense bacterial motion of motile cells by probing motion on different topographical features (cavities) and the use of surface funtionalisation. Probing motion on silicon, arrays of silicon/silicon dioxide cavities, and the change in surface functionalisation, we could compare the vibration amplitudes of the *Escherichia coli (E. coli)* 7740 strain [50]. In particular, we investigate the contribution of cell trapping and surface functionalisation on a reflective mirror and demonstrate that bacterial motion is increasingly present if resided in a specific location. Moreover, by tracking the motion of these bacteria, we can conclude that even a simple design enables antibiotic susceptibility testing with a single-bacterium sensitivity. Additionally, this technique is compared to a highly sensitive single-cell technique based on graphene membranes. Though the sensitivity of the new technique is lower, a motile cell is still detected and the technique is less affected by the limitations present in current techniques. Therefore, this opens new routes towards label-free, non-invasive monitoring of nanomotion at single-cell level on rigid structures, with an elementary design of a reflective backmirror.

4.2 CAVITIES FOR PROBING MOTION OF A SINGLE BACTERIUM

The experiments were performed using circular cavities with a diameter of 8 μm and a depth of 285nm that were etched in SiO_2. A silicon chip with an array of thousands of these cavities was placed inside a cuvtte containing *E. coli* in LB medium (fig 4.1a). APTES was used to bind the bacteria to the surface. APTES is an aminosilane that acts as a binder by covalant attaching [51]. The nanomotion of the bacteria was measured using an inferferomteric setup[52], see figure 4.1b. The bacterium induced a refraction in the laser path, which can be determined from the modulation of the intensity of the reflected light. To quantitatively compare the nanomotion of different measurements, we acquire voltage traces of the photodiode over 30 seconds and normalize the data to obtain voltage amplitudes (signal fluctuations), to measure the change in Signal-to-Noise-Ratio (SNR).

To compare the difference in signal between different substrates and experiments, the background noise was determined first. The voltage amplitudes of a cavity without a bacterium were taken as the noise of the system, which is resulting in 0 dB. The cavities containing a single live bacterium displayed a larger fluctuation in the amplitudes and resulted in a time average SNR of 19 dB. The increase in amplitudes can be associated with the motility of the bacterium. The trapped bacterium in a cavity is inducing a refraction in the laser path [53]. Fabry-Pérot interferometry requires two mirrors and in measuring bacterial nanomotion on silicon, the cell walls of the bacterium might function as one of the mirrors. Fig 4.1c shows normalized data for the noise measurement, a single bacterium in a cavity and the graphene membrane with a single bacterium, respectively. Note the increase in σ from left to right and the already vivid increase in amplitudes for a rigid substrate.

4.3 IMPACT OF TRAPPING

To investigate the role of cell trapping, we compare the voltage amplitudes of four techniques using a silicon backmirror. Firstly, we evaluate the SNR of bacteria on only a silicon substrate. Secondly, we extend this by adding surface functionalization (APTES), to ensure adhesion between the substrate and the bacteria (indicated with a + sign after the specific substrate). Additionally, we confine the bacteria to a topographical location by designing Si/SiO_2 cavities on the substrate. Lastly, the same surface functionalization has been applied to these cavities, to obtain bacterium that resides in a specific cavity.

The voltage fluctuation due to the motion of a single bacterium for the four different measurements are displayed in figure 2 prior and post exposure to antibiotics. In figure 2a the voltage amplitude on Si is observed not to be substantially lowered after exposure to the antibiotics. However, the SNR observed was higher than the background (8.4 dB). The surface was then exposed to APTES and a vivid voltage amplitude increase is present, shown in 2b. We observed for the substrate with the Si/SiO_2 cavities a bacterium stays here for a longer time duration due to the surface roughness of the cavity[44]. The signal conveys this message in figure 3c as the voltage amplitude is relatively low but drastically increases as soon as a bacterium is located in the cavity. This hypothesis is also observed by using both the functionalising agent and the cavities, resulting in the highest motion amplitude (19.4 dB).

4.4 ANTIBIOTIC EFFICACY ON A SINGLE BACTERIUM

Subsequently, we explored the four cases for antibiotic susceptibility test by monitoring the voltage amplitude due to the motility of the bacteria. On the right side of fig 2 a few example voltages of the situations were already presented. To test efficacy of antibiotics and the impact of graphene membranes, silicon mirror and cell trapping on single-cell motion detection for the situation presented, we calculated the Root Mean Square (RMS) of the measured voltage over 30 seconds on the given substrates, both prior and 1 hour post exposure to antibiotic (chloramphenicol) above its Minimum Inhibitory Concentration (MIC). In all the measurements the results were neglected if there was no bacterium present during the motion detection (optically confirmed and/or visible in the voltage amplitudes). Fig 3a-e shows the measured SNR for the different experiments, including the graphene membranes measurements. The drop in median value shows the decrease in sensitivity along the different measurements. Conclusively, these result show that for all the situation, motile cells can be detected.

The histogram of the motion amplitude on the Si/SiO_2 cavities are shown in figure 3b′-c′, with and without surface functionalisation, respectively. In both the situations we can distinguish the difference prior and post antibiotic exposure as the median SNR decreases from 19.4 dB to 9.9 dB for 3b′ and 17.3 dB to 11.8 dB for 3c′. The silicon substrate show similar behavior in the data (fig 3d′). We observe a decrease in SNR from 16.2 dB to 9.9 dB for 3d′ and no change in motion for 3e′ (8.4 dB). These results show that one can use a Si background for probing nanomotion of cells and testing antibiotic susceptibility based on the SNR. Additionally, trapping a cell at a desired location shows an increasing trend in the SNR.

4.5 DISCUSSION

We present an alternative, yet elementary, method to measure nanomotion of a single bacterial cell. Single *E. coli* bacterium were observed to produce peak fluctuation resulting in up to and 30, 30, 22, and 18 dB for Si/SiO_2+, Si/SiO_2, Si+, and Si substrates, respectively. By comparing the voltage amplitudes of these different situations, we conclude that cell trapping (topographical features and/or surface functionalization) is of paramount importance for increasing the motion detection of nanoscale vibrations. It is worth noting that a motile cell is observed with a simple, rigid, and reflective backmirror, instead of using a more complex and flexible structure, such as a suspended graphene membrane, though at a significantly lower amplitude.

Other than probing nanomotion and antibiotic susceptibility experiments, the experimental setup offers the possibility to trace this motion in real-time. This enables us to see the effect of antibiotics on the nanomotion for a long time-frame. The real-time tracking is only achievable for the trapped bacteria. These motion measurements on just Si are only capable if the topographical placement of a bacteria is known and it is almost immovable (or at least unable to escape the topographical feature), which is evidently difficult in these type of measurements. The high OD of the bacteria enabled this motion detection on Si or one would need to (optically) track the location of the bacterium. Moreover, the SiO_2 cavities elucidate this is possible for lower OD and opens new routes to topographical features on Si, to enable rapid and elementary antibiotic susceptibility testing.

FIGURES

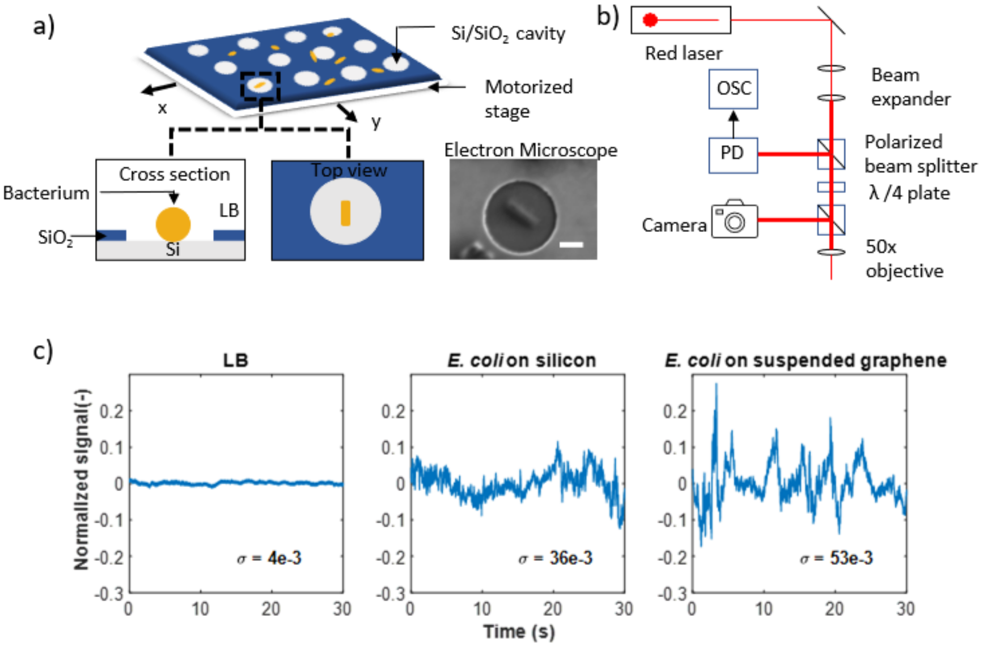

Figure 4.1: Detection of nanomotion of a single bacterium. a) Schematic illustration of the substrate used to trap a single bacterium in a cavity. The SEM image shows a bacterium in a cavity. The white scale bar is 1 μm. b) Schematic depiction of the interferometric measurement setup used to record the nanomotion. c) Recorded signal of a cavity filled with LB (left), compared to the signal from a cavity with LB and a bacterium (middle), and to a signal from a cavity covered with suspended graphene membrane, LB and a bacterium (right). The square root of the variances (σ^2), or the Root Mean Square, is showing an increase in fluctuation from left to right.

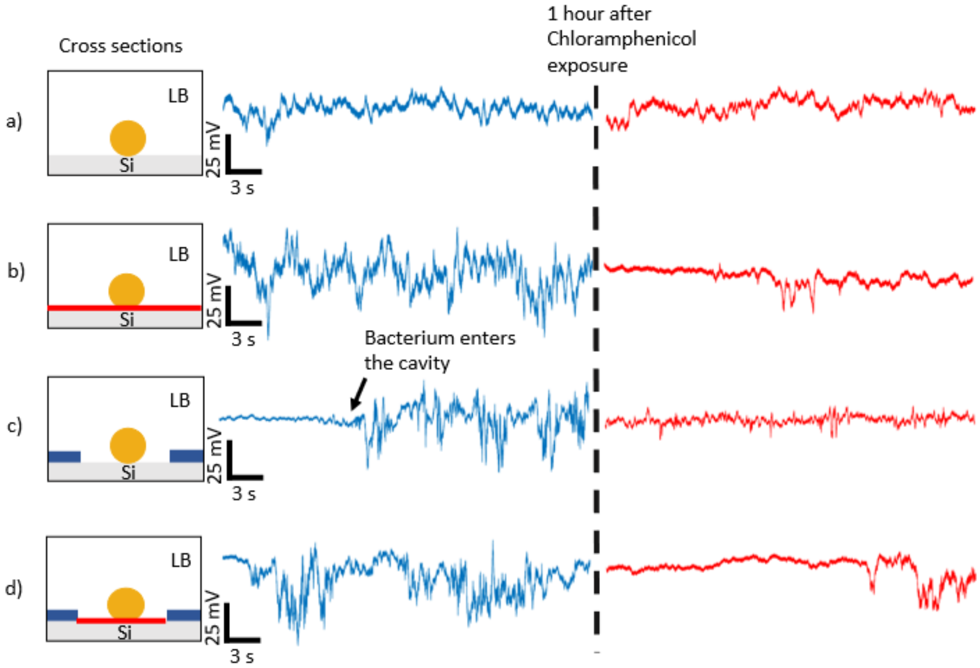

Figure 4.2: Voltage fluctuation of a single bacterium and single-cell antibiotic sensitivity screening on silicon. The left side of the figure shows the cross section of the experiments conducted. The red line present in the cross sections represents surface functionalization, ensuring the adhesion of the bacteria to the surface. The black dotted line represents 1 hour after adding Chloramphenicol. a) A single bacterium on silicon surface without surface functionalisation. b) A single bacterium on silicon surface with surface functionalisation. c) A single bacterium trapped in Si/SiO$_2$ cavity without surface functionalisation. d) A single bacterium trapped in Si/SiO$_2$ cavity with surface functionalisation.

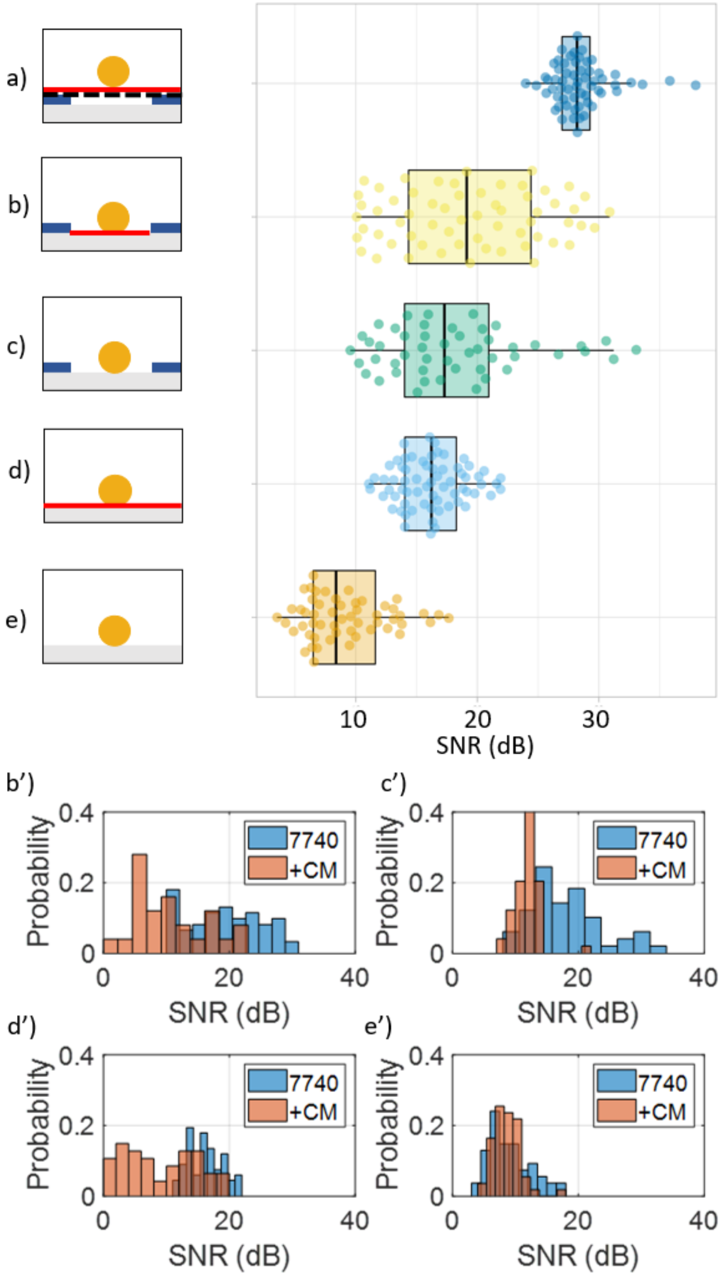

Figure 4.3: Impact of graphene membrane, silicon, cell trapping and functionalisation for single-cell detection and antibiotic efficacy. a-e) Boxplot for all the measurements conducted in this work with the double-layer graphene membranes (n=60), Si/SiO$_2$+ cavity (n=61), Si/SiO$_2$- cavity (n=49), Si+ cavity (n=67), Si+ (n=67) and Si- (n=55), respectively. The + sign indicates surface functionalisation. The graphene measurements is from previous work [8]. The box plot indicates the 25th, 50th (median) and 75th percentiles, whereas whiskers extend to maximum 1.5 times the interquartile distance. b'-e') Histograms of the SNR of the 7740 strain measurements (blue) and 1 hour post Chloramphenicol exposure (red) for the 4 different experiments.

Substrate	Number of measurements (n)	Median SNR before exposure (dB)	Median SNR after exposure (dB)	p-value
Si/SiO$_2$+	61	19.4	9.9	7.6e-7
Si/SiO$_2$-	49	17.3	11.8	8.3e-10
Si+	67	16.2	9.9	5.9e-10
Si-	55	8.4	8.4	9.1e-1

Table 4.1: Efficacy of Chloramphenicol measured 1 hour after exposure for the different substrates. The median value of the SNR before and after exposure are compared, and the probability (p-value) that the drug has no effect on the SNR is evaluated using a two-tailed rank test.

METHODS

Sample preparation

The *E. coli* cells are grown in LB medium overnight at 30°C. The next day before performing experiment, the culture was refreshed with a 1:100 volume for 2.5 hours on fresh LB medium at 30°C. To determine the amount of bacteria present in the suspension (cells/ml), the optical density can be measured. The OD_{600} measures the optical density at a wavelength of $600nm$. The suspension used in experiments reach $OD_{600} = 0.2 - 0.3$. If the experiments need bacteria stuck to the surface, the surface has to be functionalised. This is done by adding APTES to the suspension with a final concentration of 0.1% APTES before adding the suspension to the substrate. The chamber was filled with the solution and left for 15 minutes in horizontal position to deposit the bacteria on the surface. An optical microscope (keyence VHX-7000) was used to inspect the sample. The chamber was placed in the interferomtric setup (fig 4.1a) for nanomotion detection.

The setup was equipped with Attocube ECSx5050 nano positioners that allowed us to have automated scanning of the desired locations, such as the cavities. The motion of the bacterium is causing a refraction in the laser path and the reflected light was measured with a photodiode. The photodiode signal was fed to a digital oscilloscope (Rohde & Schwarz RTB2004). For each measurement point a trace was recorded for at least 30 seconds with a sampling rate of at least 1000 Hz. The measurements were performed in an air-conditioned room with a temperature of 21 degree Celsius. For the efficacy of Chloramphenicol, the measurements were repeated 1 hour after the antibiotic was added to the solution. The substrates were 5x5 mm^2 silicon chips or 5x5 mm^2 silicon chips with a 285 nm layer of silicon oxide that were patterned with circular holes by a reactive ion etch, where silicon acts as a stop layer.

Amplitude calibration

The deflection of the membrane was obtained from the photodiode voltage due to the variations in reflected intensity of the red laser as explained in previous work[8]. Similarly, the reflected intensity variations can be used to analyse the silicon substrates. However, since there is no movable membrane, one cannot convert the variation to nanomotion for these substrates. Therefor we calculated the SNR, to compare the measurements. First the time trace of the photodiode voltage $V_{pd}(t)$ was normalized by division over its average, $V_{norm}(t) = V_{pd}(t) / < V_{pd}(t) >$, and a linear fit was subtracted from the data to eliminate the effects of drift during the measurements. Next, the RMS of the signals can be calculated as $A = \sqrt{\frac{1}{n}\sum_{i=1}^{n} x_i^2}$, where x_i represents the amplitude at that data point and n the total number of data points. The SNR is calculated using the following relation between Power P and the voltage V: $SNR = \frac{P_{\text{signal}}}{P_{\text{noise}}} = \left(\frac{V_{\text{signal}}}{V_{\text{noise}}}\right)^2 = \left(\frac{A_{\text{signal}}}{A_{\text{noise}}}\right)^2$. Because of the very wide dynamic range of signals, they are often expressed using a logarithmic decibel scale: $SNR_{dB} = 10\log_{10}\left(\frac{A_{\text{signal}}}{A_{\text{noise}}}\right)^2 = 20\log_{10}\left(\frac{A_{\text{signal}}}{A_{\text{noise}}}\right)$. The fluctuation in amplitude of the signal of the empty silicon cavities (in LB medium) is taken as the noise of the system. This means that the SNR of these measurements is 0 dB. We can now compare the different signals quantitatively.

Statistics

The data of the conducted experiments are not normally distributed. Thus we rely on non-parametric tests for statistics. We present the median and quartiles of data in boxplots, which is in accordance of non-parametric tests. We used a signed rank test whenever repeated measurements on the same cavity and bacterium is available (i.e. Si/SiO_2+) and a rank sum test for comparison between uncertain measurements (i.e. unknown location of bacterium). We used Matlab built-in functions for statistical analysis. All tests were two-sided.

5 CONCLUSION AND DISCUSSION

A single-cell sensing method of motile cells is presented that is based on measuring the refraction in the laser path, induced by a single motile bacterium. By introducing cavities for the bacteria and/or surface functionalisation and evaluating the resulting difference in voltage fluctuation observed by the photodiode, conclusions can be drawn on the sensitivity of the different substrates and the efficacy of antibiotic susceptibility.

In this thesis four substrates are highlighted. All these substrates consist of a reflective silicon mirror for an optimal reflectivity. Besides, the simplicity of only using the Si substrate, also three additional features have been evaluated. By increasing the additional features to Si with surface functionalisation and Si/SiO_2 cavities with and without the surface functionalisation. This research explains, through the evaluation of these four substrates, the importance of the surface functionalisation and topographical features on nanomotion detection and subsequently the efficacy of Chloramphenicol. Additionally, the highly sensitive suspended graphene membrane is also highlighted, to compare the sensitivity of the novel substrates.

5.1 CELL TRAPPING

The importance of residing a bacterium on a specific location has already been stressed throughout this thesis. Three different cell trapping techniques have been discussed in this work. The first method was the capillary assembly and is aimed at the cell trapping of bacteria in topographic features as it can be used to attain control of position, orientation and interparticle distance. The second technique is based on gravitational sedimentation and is an elementary, yet effective way of trapping. Finally, sieving was evaluated and by applying a pressure to different substrates a flow could be initiated to trap bacteria. The sieving was very promising to attain cell trapping on the graphene membranes but was found to be unsuccessful. This was most likely caused by either the growth medium or the flagella of the bacteria. Though only 2 methods were prosperous, they could effectively been used to test the motion of bacteria on different substrates.

5.2 NANOMOTION DETECTION AND ANTIBIOTIC EFFICACY

The measured voltages during the experiments are showing a vivid increase in voltage fluctuation due to the presence of a bacterium. It is argued that this amplitude increase was due to the motility of a bacterium. The SNR and thus comparing the noise of the system to the different experiments concluded that the motility of the bacterium was indeed causing this increase in amplitudes. Later on this was once more confirmed by the decrease of amplitudes during the exposure to antibiotics. Moreover, an increasing trend in the SNR was evidently present when ensuring the topographical placement of a bacteria using surface functionalisation and/or cavities. This opens the door to elementary nanomotion detection designs, using topographic features and rigid structures.

However, in terms of sensitivity of the different substrates, the graphene membrane still remains unchallenged. Meaning that the elementary silicon nanomotion detection designs are feasible for fast and simple monitoring of motile cells but are nowhere close to the sensitivity of graphene membranes, which could even be used for less motile cells. Nonetheless, one could argue that there is a trade-off between the limitations of the flexible designs and the robust rigid substrates.

Subsequently, the different situations were exposed to Chloramphenicol to observe if AST is applicable, which is of paramount importance to combat the incline of multiresistant bacteria. The time traces and consequently the calculation of the SNR shows that these experiments are capable of performing AST. The long time traces show that the decrease of SNR is observable 1 hour after the exposure to antibiotics. The decrease is distinctively noticeable if the same bacterium is measured, meaning that the trapping again is of great importance. It is also worth noting that even a simple silicon surface, without additional features, can notice motile cells. However, it has no significance difference in the SNR post antibiotic exposure. Additionally, the graphene membranes show a high SNR for all the measurement points, while the different silicon experiments show a wide range of SNR, even during the same experiment. Conclusively, graphene membranes have a large drop in SNR for each individual measurement and therefore have less necessity for a large data set.

5.3 RECOMMENDATIONS

Hundreds of measurements were performed to test the sensitivity of the different samples and its efficacy to antibiotics. Though all methods show sensitivity to motile cells, we concluded the highest sensitivity was observed in cavities and even higher on graphene. It was hard to deterministically comment on the location of the bacteria during the experiments. The use of well-defined traps, such as a maze taking into account the clockwise motion of the *E. coli*, could ensure the trapping with a negligible change of the cell leaving. Additionally, since the graphene membranes are the most sensitive (even detecting minimally-motile cells), finding a way to trap the bacteria on these membranes would result in the biggest impact in the field of AST.

The most interesting application of these diverging samples is to implement a method to test different concentrations or different kinds of antibiotics on a single substrate. To assure reasonable AST the use of a single substrate is highly recommended. With the fast screening of thousand of membranes or cavities on one substrate, this method could evolve into a rapid and non-invasive monitoring tool. One could for example define multiple parallel channels on top of the substrate, to test different antibiotics on the substrates. Though this method is already considered as a rapid measurement (30seconds per measurement point), the time could be improved even more by measuring all the cavities/membranes at once by collimating the laser on the entire substrate.

BIBLIOGRAPHY

1. A. J. Alanis, "Resistance to antibiotics: are we in the post-antibiotic era?," *Archives of medical research*, 2005.
2. R. T. Horvat, "Review of antibiogram preparation and susceptibility testing systems," *Hospital Pharmacy*, vol. 45, no. 11_suppl, 2010.
3. L. Venturelli, A.-C. Kohler, P. Stupar, M. I. Villalba, A. Kalauzi, K. Radotic, M. Bertacchi, S. Dinarelli, M. Girasole, M. Pešić, J. Banković, M. E. Vela, O. Yantorno, R. Willaert, G. Dietler, G. Longo, and S. Kasas, "A perspective view on the nanomotion detection of living organisms and its features," *Journal of Molecular Recognition*, 2020.
4. A. Kohler, L. Venturelli, G. Longo, G. Dietler, and S. Kasas, "Nanomotion detection based on atomic force microscopy cantilevers," *The Cell Surface*, vol. 5, 2019.
5. Y. Hancock, "The 2010 nobel prize in physics—ground-breaking experiments on graphene," *Journal of Physics D: Applied Physics*, vol. 44, no. 47, p. 473001, 2011.
6. I. Yin, Y. Zhao, C. Lin, H.-H. Tsai, Y. Juang, and G. Urban, "Development of a microfluidic device with microcantilever sensor array for probing single cancer cells mechanics," *2011 16th International Solid-State Sensors, Actuators and Microsystems Conference, TRANSDUCERS'11*, pp. 1216–1219, 06 2011.
7. S. Kasas, F. S. Ruggeri, C. Benadiba, C. Maillard, P. Stupar, H. Tournu, G. Dietler, and G. Longo, "Detecting nanoscale vibrations as signature of life," *Proceedings of the National Academy of Sciences*, vol. 112, no. 2, pp. 378–381, 2015.
8. I. Roslon, A. Japaridze, P. Steeneken, C. Dekker, and F. Alijani, "Probing nanomotion of single bacteria with graphene drums," *bioRxiv*, 2021.
9. S. B. Zaman, M. A. Hussain, R. Nye, V. Mehta, K. T. Mamun, and N. Hossain, "A review on antibiotic resistance: alarm bells are ringing," *Cureus*, vol. 9, no. 6, 2017.
10. J. R. e. a. A. van Belkum, C.D. Burnham, "Innovative and rapid antimicrobial susceptibility testing systems.," *Nature Reviews Microbiology*, vol. 18, p. 299–311, 2020.
11. G. L. e. a. A.van Belkum, T.T. Bachmann, "Developmental roadmap for antimicrobial susceptibility testing systems.," *Nature Reviews Microbiology*, vol. 17, p. 51–62, 2019.
12. A. Boisen, S. Dohn, S. S. Keller, S. Schmid, and M. Tenje, "Cantilever-like micromechanical sensors," *Reports on Progress in Physics*, vol. 74, no. 3, p. 036101, 2011.
13. P. S. Waggoner and H. G. Craighead, "Micro-and nanomechanical sensors for environmental, chemical, and biological detection," *Lab on a Chip*, vol. 7, no. 10, pp. 1238–1255, 2007.
14. F. Pujol-Vila, R. Villa, and M. Alvarez, "Nanomechanical sensors as a tool for bacteria detection and antibiotic susceptibility testing," *Frontiers in Mechanical Engineering*, vol. 6, 2020.
15. B. N. Johnson and R. Mutharasan, "Biosensing using dynamic-mode cantilever sensors: A review," *Biosensors and Bioelectronics*, vol. 32, 2012.
16. R. S. A. Mathew, R., "A review on surface stress-based miniaturized piezoresistive su-8 polymeric cantilever sensors.," *Nano-Micro Lett.*, 2018.

17. G. G. Stoney, "The tension of metallic films deposited by electrolysis.," *Proc. R. Soc. Lond.*, 1909.

18. G. Longo, L. Alonso-Sarduy, L. Rio, A. Bizzini, A. Trampuz, J. Notz, G. Dietler, and S. Kasas, "Rapid detection of bacterial resistance to antibiotics using afm cantilevers as nanomechanical sensors," *Nature nanotechnology*, vol. 8, 2013.

19. A. Kohler, L. Venturelli, G. Longo, G. Dietler, and S. Kasas, "Nanomotion detection based on atomic force microscopy cantilevers," *The Cell Surface*, vol. 5, p. 100021, 2019.

20. K. M. K. K. e. a. Etayash, H., "Microfluidic cantilever detects bacteria and measures their susceptibility to antibiotics in small confined volumes.," *Nature communications*, vol. 7, 2016.

21. D. G. Papageorgiou, I. A. Kinloch, and R. J. Young, "Mechanical properties of graphene and graphene-based nanocomposites," *Progress in Materials Science*, vol. 90, pp. 75–127, 2017.

22. G.-H. Lee, R. C. Cooper, S. J. An, S. Lee, A. Van Der Zande, N. Petrone, A. G. Hammerberg, C. Lee, B. Crawford, W. Oliver, *et al.*, "High-strength chemical-vapor–deposited graphene and grain boundaries," *science*, vol. 340, no. 6136, pp. 1073–1076, 2013.

23. Y. Hwangbo, C.-K. Lee, S.-M. Kim, J.-H. Kim, K.-S. Kim, B. Jang, H.-J. Lee, S.-K. Lee, S.-S. Kim, J.-H. Ahn, *et al.*, "Fracture characteristics of monolayer cvd-graphene," *Scientific reports*, vol. 4, no. 1, pp. 1–9, 2014.

24. H. Tian, Y. Shu, X.-F. Wang, M. A. Mohammad, Z. Bie, Q.-Y. Xie, C. Li, W.-T. Mi, Y. Yang, and T.-L. Ren, "A graphene-based resistive pressure sensor with record-high sensitivity in a wide pressure range," *Scientific reports*, vol. 5, no. 1, pp. 1–6, 2015.

25. Y. Wang, Z. Li, D. Hu, C.-T. Lin, J. Li, and Y. Lin, "Aptamer/graphene oxide nanocomplex for in situ molecular probing in living cells," *Journal of the American Chemical Society*, vol. 132, no. 27, pp. 9274–9276, 2010.

26. Z. Fang, Z. Liu, Y. Wang, P. M. Ajayan, P. Nordlander, and N. J. Halas, "Graphene-antenna sandwich photodetector," *Nano letters*, vol. 12, no. 7, pp. 3808–3813, 2012.

27. R. Hooke, *Lectiones Cutlerianae, Or a Collection of Lectures: Physical, mechanical, Geographical & Astronomical, Made Before the Royal Society on Several Occasions... to which are Added Divers Miscellaneous Discourses*. John Martyn printer, 1963.

28. I. Newton, *The mathematical principles of natural philosophy. By Sir Isaac Newton. Translated into English by Andrew Motte. To which are added, The laws of the moon's motion, according to gravity. By John Machin Astron. Prof. Gresh. and Secr. R. Soc. In two volumes*. Benjamin Motte, at the Middle-Temple-Gate, in Fleetstreet, 1729.

29. A. Castellanos-Gomez, V. Singh, H. S. van der Zant, and G. A. Steele, "Mechanics of freely-suspended ultrathin layered materials," *Annalen der Physik*, vol. 527, no. 1-2, pp. 27–44, 2015.

30. J. F. Swennenhuis, A. G. Tibbe, M. Stevens, M. R. Katika, J. Van Dalum, H. D. Tong, C. J. van Rijn, and L. W. Terstappen, "Self-seeding microwell chip for the isolation and characterization of single cells," *Lab on a Chip*, vol. 15, no. 14, pp. 3039–3046, 2015.

31. F. Abali, J. Broekmaat, A. Tibbe, R. B. Schasfoort, L. Zeune, and L. W. Terstappen, "A microwell array platform to print and measure biomolecules produced by single cells," *Lab on a Chip*, vol. 19, no. 10, pp. 1850–1859, 2019.

32. R. A. Sampson, "Xii. on stokes's current function," *Philosophical Transactions of the Royal Society of London.(A.)*, no. 182, pp. 449–518, 1891.

33. H. L. Weissberg, "End correction for slow viscous flow through long tubes," *The Physics of Fluids*, vol. 5, no. 9, pp. 1033–1036, 1962.

34. K. Celebi, J. Buchheim, R. M. Wyss, A. Droudian, P. Gasser, I. Shorubalko, J.-I. Kye, C. Lee, and H. G. Park, "Ultimate permeation across atomically thin porous graphene," *Science*, vol. 344, no. 6181, pp. 289–292, 2014.

35. J. Vlassak and W. Nix, "A new bulge test technique for the determination of young's modulus and poisson's ratio of thin films," *Journal of materials research*, vol. 7, no. 12, pp. 3242–3249, 1992.

36. P. Hariharan, *Basics of interferometry*. Elsevier, 2010.

37. D. Davidovikj, J. J. Slim, S. J. Cartamil-Bueno, H. S. van der Zant, P. G. Steeneken, and W. J. Venstra, "Visualizing the motion of graphene nanodrums," *Nano letters*, vol. 16, no. 4, pp. 2768–2773, 2016.

38. P. Blake, E. Hill, A. Castro Neto, K. Novoselov, D. Jiang, R. Yang, T. Booth, and A. Geim, "Making graphene visible," *Applied physics letters*, vol. 91, no. 6, p. 063124, 2007.

39. B. N. Johnson and R. Mutharasan, "Biosensing using dynamic-mode cantilever sensors: A review," *Biosensors and bioelectronics*, vol. 32, no. 1, pp. 1–18, 2012.

40. L. Malaquin, T. Kraus, H. Schmid, E. Delamarche, and H. Wolf, "Controlled particle placement through convective and capillary assembly," *Langmuir*, vol. 23, no. 23, pp. 11513–11521, 2007.

41. V. Flauraud, M. Mastrangeli, G. D. Bernasconi, J. Butet, D. T. Alexander, E. Shahrabi, O. J. Martin, and J. Brugger, "Nanoscale topographical control of capillary assembly of nanoparticles," *Nature nanotechnology*, vol. 12, no. 1, pp. 73–80, 2017.

42. P. Louis, H. Trüper, and E. Galinski, "Survival of escherichia coli during drying and storage in the presence of compatible solutes," *Applied microbiology and biotechnology*, vol. 41, no. 6, pp. 684–688, 1994.

43. J. Wan, T. K. Tokunaga, and C.-F. Tsang, "Bacterial sedimentation through a porous medium," *Water Resources Research*, vol. 31, no. 7, pp. 1627–1636, 1995.

44. S. Wu, B. Zhang, Y. Liu, X. Suo, and H. Li, "Influence of surface topography on bacterial adhesion: A review," *Biointerphases*, vol. 13, no. 6, p. 060801, 2018.

45. S. Zheng, M. Bawazir, A. Dhall, H.-E. Kim, L. He, J. Heo, and G. Hwang, "Implication of surface properties, bacterial motility, and hydrodynamic conditions on bacterial surface sensing and their initial adhesion," *Frontiers in Bioengineering and Biotechnology*, vol. 9, p. 82, 2021.

46. W. R. DiLuzio, L. Turner, M. Mayer, P. Garstecki, D. B. Weibel, H. C. Berg, and G. M. Whitesides, "Escherichia coli swim on the right-hand side," *Nature*, vol. 435, no. 7046, pp. 1271–1274, 2005.

47. M. Ghosh, M. A. Junker, R. T. Van Lent, L. Madauß, M. Schleberger, H. Lebius, A. Benyagoub, J. A. Wood, and R. G. Lammertink, "Charge regulation at a nanoporous two-dimensional interface," *ACS omega*, vol. 6, no. 4, pp. 2487–2493, 2021.

48. P. A. Lefebvre, "Flagellar amputation and regeneration in chlamydomonas," *Methods in cell biology*, vol. 47, pp. 3–7, 1995.

49. E. Leifson, “Staining, shape, and arrangement of bacterial flagella,” *Journal of bacteriology*, vol. 62, no. 4, pp. 377–389, 1951.

50. E. J. Gauger, M. P. Leatham, R. Mercado-Lubo, D. C. Laux, T. Conway, and P. S. Cohen, “Role of motility and the flhdc operon in escherichia coli mg1655 colonization of the mouse intestine,” *Infection and immunity*, vol. 75, no. 7, pp. 3315–3324, 2007.

51. R. L. Meyer, X. Zhou, L. Tang, A. Arpanaei, P. Kingshott, and F. Besenbacher, “Immobilisation of living bacteria for afm imaging under physiological conditions,” *Ultramicroscopy*, vol. 110, no. 11, pp. 1349–1357, 2010.

52. J. M. Vaughan, *The Fabry–Perot Interferometer: History, Theory, Practice and Applications*. Routledge, 2017.

53. I. Bennett, A. L. Pyne, and R. A. McKendry, “Cantilever sensors for rapid optical antimicrobial sensitivity testing,” *ACS sensors*, vol. 5, no. 10, pp. 3133–3139, 2020.

54. R. Frisenda, E. Navarro-Moratalla, P. Gant, D. P. De Lara, P. Jarillo-Herrero, R. V. Gorbachev, and A. Castellanos-Gomez, “Recent progress in the assembly of nanodevices and van der waals heterostructures by deterministic placement of 2d materials,” *Chemical Society Reviews*, vol. 47, no. 1, pp. 53–68, 2018.

55. K. Kinoshita, R. Moriya, M. Onodera, Y. Wakafuji, S. Masubuchi, K. Watanabe, T. Taniguchi, and T. Machida, “Dry release transfer of graphene and few-layer h-bn by utilizing thermoplasticity of polypropylene carbonate,” *npj 2D Materials and Applications*, vol. 3, no. 1, pp. 1–8, 2019.

56. W. Liu, H. Li, C. Xu, Y. Khatami, and K. Banerjee, “Synthesis of high-quality monolayer and bilayer graphene on copper using chemical vapor deposition,” *Carbon*, vol. 49, no. 13, pp. 4122–4130, 2011.

57. A. V. Zaretski and D. J. Lipomi, “Processes for non-destructive transfer of graphene: widening the bottleneck for industrial scale production,” *Nanoscale*, vol. 7, no. 22, pp. 9963–9969, 2015.

58. F. Ricciardella, S. Vollebregt, B. Boshuizen, F. Danzl, I. Cesar, P. Spinelli, and P. M. Sarro, “Wafer-scale transfer-free process of multi-layered graphene grown by chemical vapor deposition,” *Materials Research Express*, vol. 7, no. 3, p. 035001, 2020.

59. G. B. Barin, Y. Song, I. de Fátima Gimenez, A. G. Souza Filho, L. S. Barreto, and J. Kong, “Optimized graphene transfer: Influence of polymethylmethacrylate (pmma) layer concentration and baking time on graphene final performance,” *Carbon*, vol. 84, pp. 82–90, 2015.

60. F. Bonaccorso, Z. Sun, T. Hasan, and A. Ferrari, “Graphene photonics and optoelectronics,” *Nature photonics*, vol. 4, no. 9, pp. 611–622, 2010.

61. D. Davidovikj, “Two-dimensional membranes in motion,” 2018.

62. F. Xia, H. Wang, D. Xiao, M. Dubey, and A. Ramasubramaniam, “Two-dimensional material nanophotonics,” *Nature Photonics*, vol. 8, no. 12, pp. 899–907, 2014.

63. J. W. Suk, R. D. Piner, J. An, and R. S. Ruoff, “Mechanical properties of monolayer graphene oxide,” *ACS nano*, vol. 4, no. 11, pp. 6557–6564, 2010.

64. D. Davidovikj, F. Alijani, S. J. Cartamil-Bueno, H. S. van der Zant, M. Amabili, and P. G. Steeneken, “Nonlinear dynamic characterization of two-dimensional materials,” *Nature communications*, vol. 8, no. 1, pp. 1–7, 2017.

65. M. S. Kumar and P. Philominathan, “The physics of flagellar motion of e. coli during chemotaxis,” *Biophysical reviews*, vol. 2, no. 1, pp. 13–20, 2010.

66. G. Bean, S. Flickinger, W. Westler, M. McCully, D. Sept, D. Weibel, and K. Amann, "A22 disrupts the bacterial actin cytoskeleton by directly binding and inducing a low-affinity state in mreb," *Biochemistry*, vol. 48, no. 22, pp. 4852–4857, 2009.

67. N. Iwai, K. Nagai, and M. Wachi, "Novel s-benzylisothiourea compound that induces spherical cells in escherichia coli probably by acting on a rod-shape-determining protein (s) other than penicillin-binding protein 2," *Bioscience, biotechnology, and biochemistry*, vol. 66, no. 12, pp. 2658–2662, 2002.

68. P. Stoica, R. L. Moses, *et al.*, "Spectral analysis of signals," 2005.

69. C. Lissandrello, F. Inci, M. Francom, M. Paul, U. Demirci, and K. Ekinci, "Nanomechanical motion of escherichia coli adhered to a surface," *Applied physics letters*, vol. 105, no. 11, p. 113701, 2014.

A SIEVING DESIGN

The sieving design was developed by a step-by-step procedure and many iterations of the design. The design did not only need the functionality of sieving particles but also had to be integrated in the current setup. Meaning that a few more requirements had to be added to the design. The requirements are summed up below:

- The design has to be mounted on the Attocube positioners. To have automated scanning of the nanomotion experiments, after the sieving experiment.
- It has to be free of leakage because we want no loss of pressure during the sieving, there are electronics in the setup and of course the biohazard of the bacteria.
- An inlet/outlet is necessary to flush in antibiotics.
- A microscopic window for the laser and the microscope to perform the nanomotion experiments.
- The location (depth) of the substrate should be in the order of the focal depth.

The design for the sieving experiments can be found in Figure A.1. The design was 3D-printed using a Prusa mk3 (SLA) printer for the rapid production and low production cost. Also, because the design was an iterative process, many different design were fabricated and tested, which favored the 3D printing technique in terms of time consumption. The final design exist out of multiple parts which are colour coded in the SolidWorks model. The exploded view shows the different parts of the design and the caption of the figure explains the parts. Note that the parts are connected with screws by creating threads in the 3D-print. Similarly, the pump connection was also connected to the design using thread. However, an additional layer of Teflon tape was added to ensure no leakage here. The inlet/outlet tubes for the antibiotics were connected using epoxy resin. A list of additional parts is shown below.

Part	**Amount**
M2 x 8 mm (Philips)	4
M2 x 12 mm (Philips)	4
M2 x 15 mm (Philips)	4
Steel hexagon hose nipple (5mm)	1
Silicon tube (1mm)	2
Silicon tube (3mm)	1
Teflon tape	1
Epoxy resin	1
Glass slide (10x10mm)	1

Table A.1: List of parts of the sieving design.

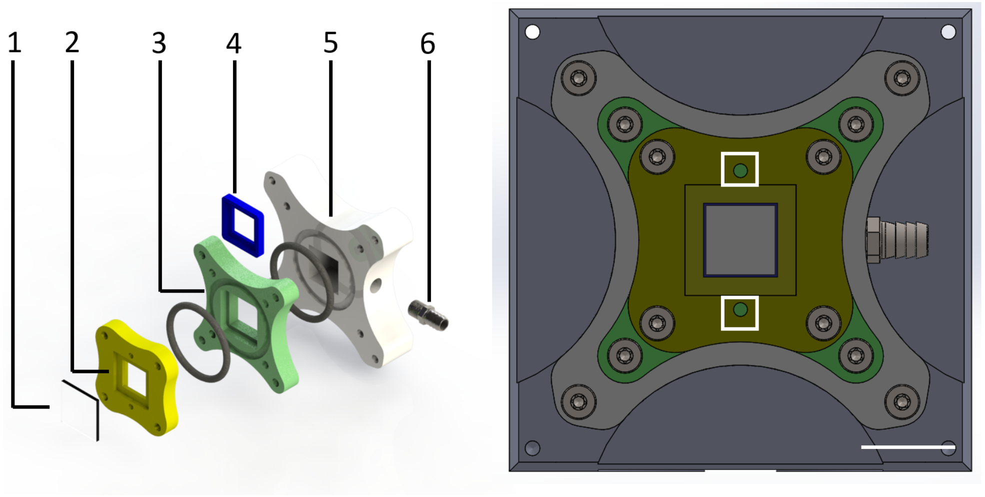

Figure A.1: Solidwork model of the design. The left panel shows an exploded view of the designed chamber.The parts are glass window (1), top chamber with the microscopic window and the inlet/outlet for antibiotics (2), middle part to seperate the vacuum chamber from the top chamber (3), chip holder is located above the middle part in the exploded view because it is placed in this part (4), vacuum chamber to create a negative pressure (5) and the pump connection (6). The O-rings ensure no leakage. The right panel shows a front view of the design mounted on the Attocube positioner. The white boxed show the inlet/outlets for the antibiotics and the white scale bar is 10 mm.

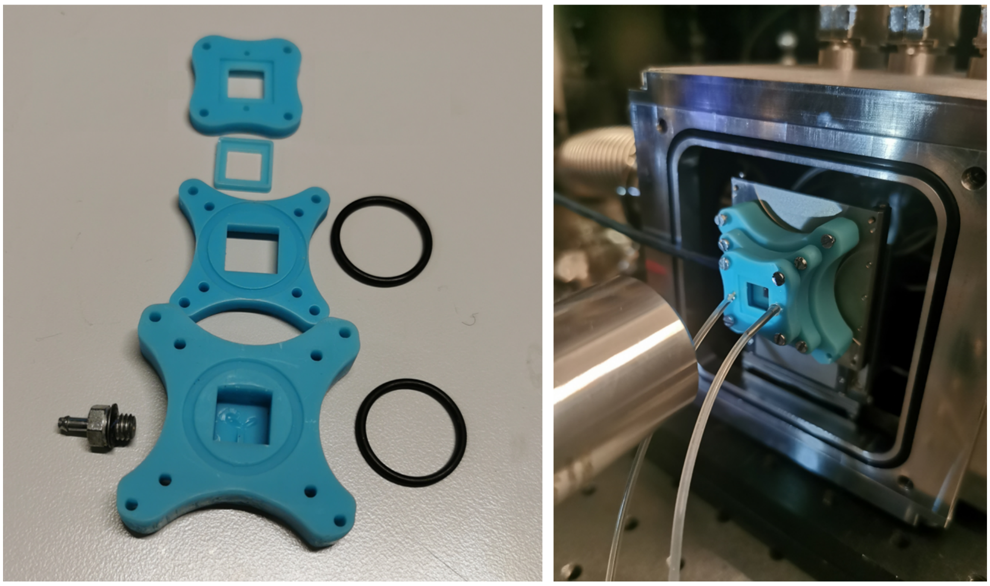

Figure A.2: The left panel shows the 3D-printed parts. The right panel shows the design mounted on the Attocube positioners. The inlet/outlet of the antibiotics is created with syringes (attached to the white tubes) and the negative pressure is applied with a pump (attached to the blue tube on the left side).

B SIEVING PROCEDURE

The sieving procedure is developed by taking into account the failure modes of Celebi et al. and Swennenhuis et al., such as the importance of pre-wetting [30, 34]. The working principle has been explained in Section 3.3.

1. Let the substrate sit in demineralized water for 45 minutes to ensure pre-wetting.
2. Depending on the amount of pores, add the growth medium (or any other medium depending on the particle or bacteria used) accordingly. Note that if one uses a mesh with thousands of holes, the flow rate can be up to 1-2 mL/min or even higher depending on the pressure.
3. Switch on the pump and wait until **most** of the liquid is through the pores. Ensuring there is a flow initiated and the pores are not blocked.
4. Switch off the pump before the liquid is completely gone. It is important to not remove all fluid, this will cause air entering the wells and this will limit the sieving. If the pump is switched off too late, return to the pre-wetting step.
5. Add the suspension with the particles or bacteria.
6. Switch off the pump after the whole sample has passed or after the flow rate is approaching zero. Note that the flow rate will decrease as more pores will become blocked by the cells.
7. The pores should now be blocked by the particles or bacteria.

C GRAPHENE TRANSFER

This chapter discusses the different methods used to transfer graphene and shows a step-by-step procedure on how to do the transfer. All methods have their pros and cons, as they vary layers, size, stress and some methods favour substrates with through-holes for the remaining liquid to be removed.

C.1 EXFOLIATED GRAPHENE

The method of exfoliated graphene or dry transfer method is a commonly used method for a quick multi-layer graphene transfer from graphite. The graphite flake is pressed upon scotch tape and removed. The tape is then pressed and released multiple times on the remaining flake to ensure the resulting flakes decrease in number of layers. Now you have multiple flakes on the scotch tape and the transfer process can begin. In Figure C.1 the step-by-step procedure is shown [54].

Note that this only works if one can hold the substrate in place (e.g. vacuum or using an adhesive material such as tape). If this is not the case, due to for example holes in the substrate, the substrate will move up when moving the PDMS stamp. An additional step to ensure transfer on the substrate is the use of Polypropylene Carbonate (PPC) and is called the van der Waals pick-up transfer method [55]. An additional layer of PPC is added on top of the PDMS before pressing the graphene flake on. The PPC ensures the graphene is released on the substrate by heating during contact. The PDMS stamp can now be moved up and the graphene flake is left on the substrate.

C.2 CHEMICAL VAPOUR DEPOSITION

CVD of graphene is a method which can produce relatively high qualilty graphene on a large scale. This method can also produce very thin layers, even up to monolayer graphene [56]. In most cases copper foil is used to synthesise mono- and double-layer graphene. This is because it is relatively inexpensive and so it is by far the best studied material for this application[57]. Due to the lack of specialist equipment and time, the graphene has been bought from Graphenea or made in-house at the faculty of EEMCS at Delft university of technology. In this thesis mono-, double- and multi-layer graphene has been used. The mono- and double-layer is synthesised on copper foil and has a sacrificial layer of Polymethyl Methacrylate (PMMA) to make the graphene visible during the transfer. The multi-layer graphene has been synthesised on silicon and molybdenum is uses as a catalyst for the growth via CVD [58].

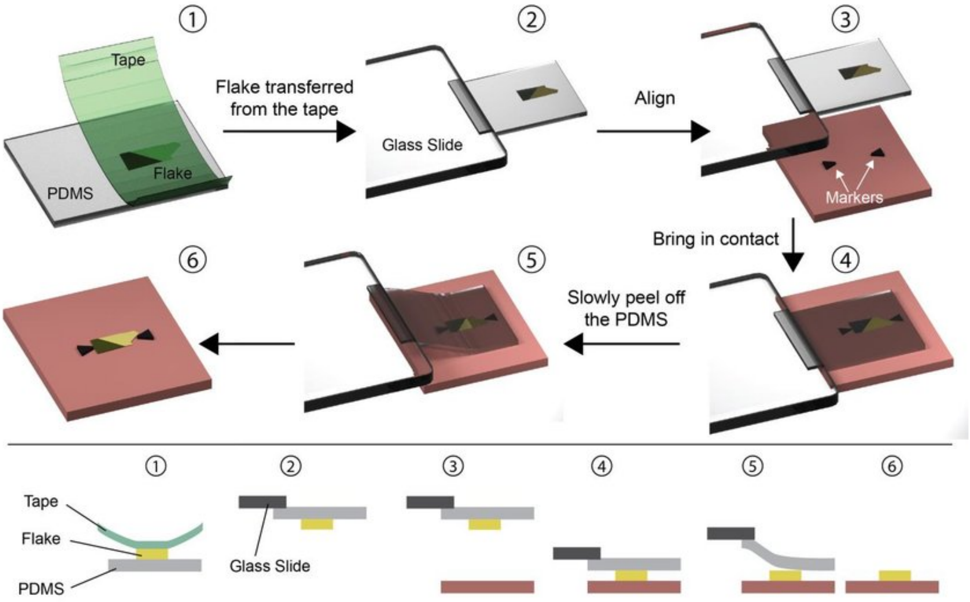

Figure C.1: The dry transfer method of graphene. The flake to be transferred is exfoliated onto a PDMS stamp (1) and the stamp is attached to a glass slide connected to a micromanipulater (2). Using a microscope the flake can be aligned with the substrate (3) and brought in contact (4). By slowly peeling (or heating and cooling) of the PDMS stamp (5) the flake is deposited on the substrate (6). Figure reproduced from [54].

C.2.1 Mono- and double-layer graphene

This section discusses the step-by-step procedure of transferring graphene to the substrate using copper foil and PMMA. Considering the thickness of the graphene, this process is very fragile and takes some practise and patience.

1. The copper foil is cut with a sharp razor knife to the desired dimensions from the big copper sheet. See Figure C.2a
2. Prepare amonium persulfate of 0.5M to etch away the copper and add the copper foil with graphene to the solution as in Figure C.2b.
3. Wait for about 50-60 minutes, the copper will slowly etch away. In Figure C.2c the etching of copper is almost done, and a thin almost invisible layer is left floating on the surface. Note that the final result is not in the figure, since it could hardly be photographed.
4. Prepare two petridishes with demineralised water. Scope with a spoon the floating graphene to the first petridish and repeat to the second, to flush away the remaining amonium persulfate. This process takes some practise and a lot of care, since the graphene is very fragile.
5. Have a clean substrate (chip) to transfer the graphene on (e.g. plasma cleaning). Move the substrate beneath the floating graphene and slowly move the substrate up until the graphene is on top of the substrate. Note that plasma cleaning is highly recommended, to ensure that the surface of the substrate is hydrophilic. Figure C.2d shows two substrates with the transfered graphene. Note that the graphene is still visible due to the PMMA.
6. Anneal the substrate overnight (≥8 hours) at 120°C for better adhesion. This will evaporate the remaining liquid on the substrate and increase the tension of graphene to substrate.

7. The final step is to remove the PMMA from the graphene. This was done by immersion in acetone for 20 minutes followed by 2 hours of annealing at 500°C. A more explicit explanation can be found in [59].

The thickness of the remaining graphene depends the number of layers. Each layer is about 0.345nm thick and so it visually looks like the substrate has no graphene. To check if the graphene is still intact one has to check the substrate under the SEM or if one wants to know the quality of the graphene a Raman spectroscopy can be performed. SEM images of a successful transfer is shown in Figure C.2e and of a failed transfer in Figure C.2f.

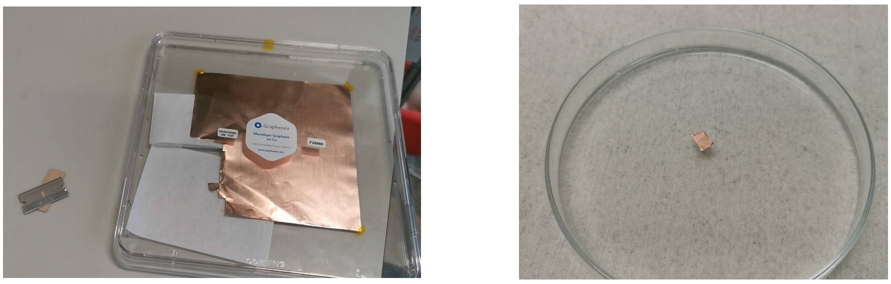

(a) The copper foil with monolayer graphene from Graphenea.

(b) The copper foil has been added to the amonium persulfate and will float.

(c) After 30 minutes the copper foil is slowly etched away.

(d) Two transfers with PMMA residue left on top. The substrates shown here are 1x1 cm.

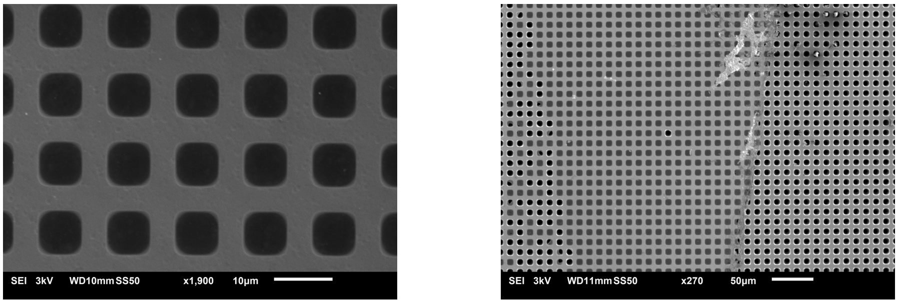

(e) SEM image of intact mono-layer graphene.

(f) SEM image of a failed transfer.

Figure C.2: a-d) Show intermediate steps of the procedure used to transfer CVD graphene on a susbrate. e-f) Show two results of the transfer method.

C.2.2 Multi-layer graphene

The procedure of multi-layer graphene is quite similar and is less fragile due to the thickness of the graphene. Ricciardella et al. discusses the process and the procedure [58]. This section summarises the steps but excludes the figures as they are similar to the mono- and double-layer process.

1. The silicon wafer with graphene is cut using a diamond pen to the desired dimensions of the graphene.
2. The wafer is placed in a petridish and a single droplet of hydrogen peroxide (h_2O_2) concentrated at 31%, is very carefully placed on top of the wafer. Note that the droplet needs to cover the entire surface, as it will release the graphene from the corners of the wafer. Thus if one has a large wafer multiple droplets are needed.
3. The petridisch is closed with parafilm to ensure that the droplet will not evaporate. The wafer is left overnight ($\geq$8 hours).
4. Deminerilazed water is slowly added to the petridish and the graphene will start to float.
5. The graphene can now be transferred on the substrate by again moving the substrate beneath the floating graphene and slowly move the substrate up until the graphene is on top of the substrate. Note that again a clean and hydrophilic surface is highly recommended.

D GRAPHENE CHARACTERISATION

This chapter shows the interferometric setup used for the characterisation of graphene and discusses the effect of a pore in the membrane. In the setup the measurement is obtained using the Fabry-Pérot cavity as explained in Section 2.4. The moving membrane acts as a mirror and so does the bottom of the cavity. The characterisation of the graphene drums can be done optically, using lasers to actuate the graphene membranes and at the same time reading out the change in deflection. Even though, different transfer techniques are used and thus the thickness of the graphene membrane differs, the principle is the same. One layer of graphene absorbs about 2.7% of the incoming light [60]. This absorption of the light results in heating of the membrane and hence causes periodic variation of the tension in the membrane by thermal expansion [61]. This change in tension, or so-called stretching and shrinking of the membrane, sets the membrane in motion. Both the lasers are focused on the membranes with a $1.5\mu m$ spotsize. The power of the red and blue laser is 2 mW and 0.5 mW, respectively. For the graphene characterisation, the actuation comes from the blue laser ($\lambda = 405nm$) instead of the red laser($\lambda = 632.8nm$), as the blue lasers absorption is two times higher than the red laser. This can be substantiated by the fact that the blue laser is closer to the absorption peak [62]. The set-up used for characterisation of graphene can be seen in Figure D.1.

In these experiments 7 drums of 5 μm covered with CVD graphene (mono-layer) are exited and the frequency response measured. Next, the pores were drilled in the membranes with a FIB by exposing to ion bombardment. We used GA-based FIB to perforate orifices of $\sim 500nm$ with low exposure doses of $5 \cdot 10^{-5} pA/nm^2$ to enable fast and precise perforation. This has been explained in Section 3.3 and a result of this can be seen in Figure 3.8. Two examples of the frequency response are shown in Figure D.2. Note that a lot of noise is present in the measurements but the resonance frequencies are visible. The resonance is used to calculate the Q-factor and the pre-tension. These values are obtained by fitting a Lorentzian shape to the frequency response. Using the formulae from Section 2.2 one could calculate the characterisation parameters. The results are shown in the first two columns of Table D.1.

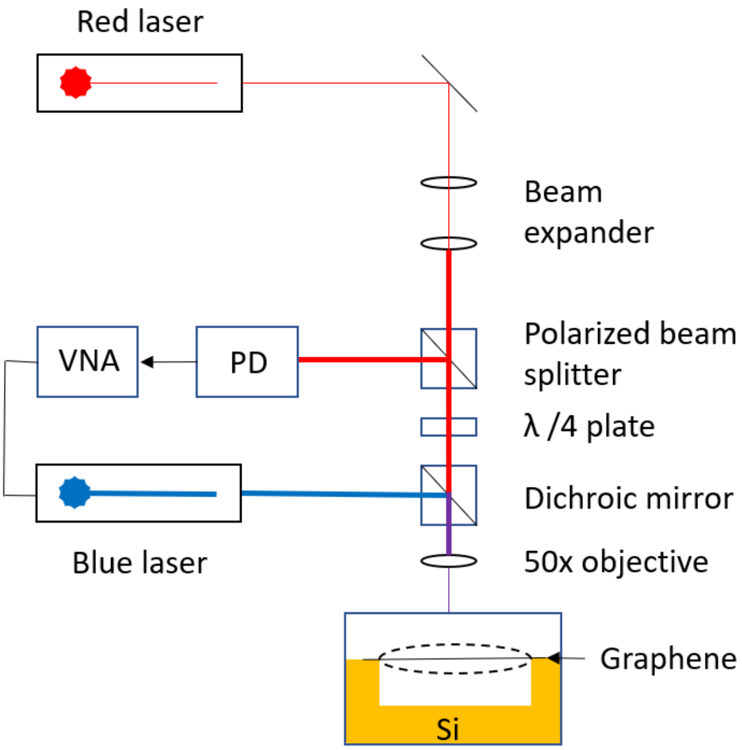

Figure D.1: The interferometry setup used to conduct experiments for graphene characterisation. The blue laser is combined with the red laser through the dichroic mirror and focused on the membrane. The red laser passes through the polarized beam splitter and the quarter-wave plate. The red laser is reflected at the bottom of the cavity and shines into the photodiode(PD). This signal is fed to the Vector Network Analyzer(VNA), which modulates the blue laser. The chip is located in a vacuum chamber. The black dotted line represents the change in deflection of the graphene membrane due to thermal excitation.

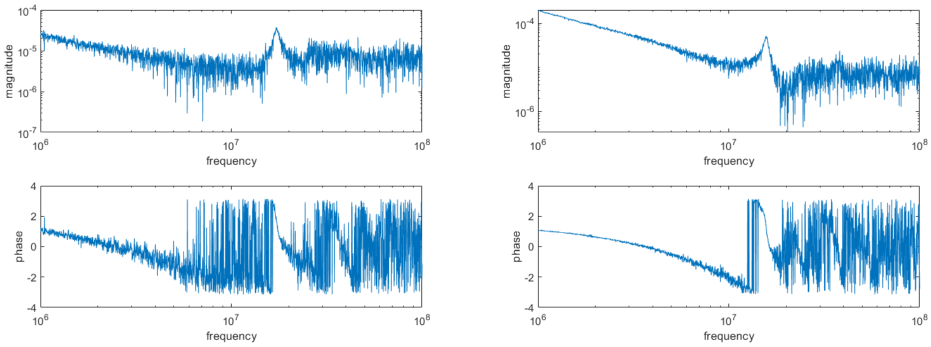

(a) 4 μm monolayer graphene membrane. **(b)** 4 μm FIB monolayer graphene membrane.

Figure D.2: The frequency and phase response of a graphene membrane for two situations. a) Shows the response for an intact membrane. b) Shows the response of a membrane with a 500 nm pore. A lorentzian shape was fitted to the frequency response to obtain the parameters.

	Monolayer graphene	**Monolayer with pore**	**Multilayer graphene**
Resonance frequency (MHz)	16.3 ± 1.9	25.6 ± 2.9	16.7 ± 2.1
Pre-tension (mN/m)	26.0 ± 5.6	179.2 ± 39.6	253.8 ± 62.9
Q-factor (-)	9.4 ± 6.0	14.4 ± 10.5	69.9 ± 33.9

Table D.1: The characteristics of 4 μm graphene membranes used in this thesis. The first and second column represent the same mono-layer graphene membrane prior and post FIB, respectively. The third column represents a multi-layer graphene membrane.

The table shows that the presence of a pore increases the resonance frequency of the membranes and so does the pre-tension as they are non-linearly related through Equation 2.4. This is in agreement with values found in literature [29, 63, 64]. However, the Q-factor in these experiments is rather low and comparing it to literature, it was expected to be at least > 50. For the membranes in this work the mono-layer graphene was transferred with CVD method and this resulted in some residue of the sacrificial layer of PMMA on top of the membranes. This can be seen in Figure D.3. To confirm this hypothesis a set of experiments consisting of 15 drums with multi-layer graphene (10 layers), has been conducted and the results are presented in the third column. The Q-factor is now in the expected order and the membranes were microscopic verified to be clean and intact (electron and optical microscope), indicating the transfer was successful.

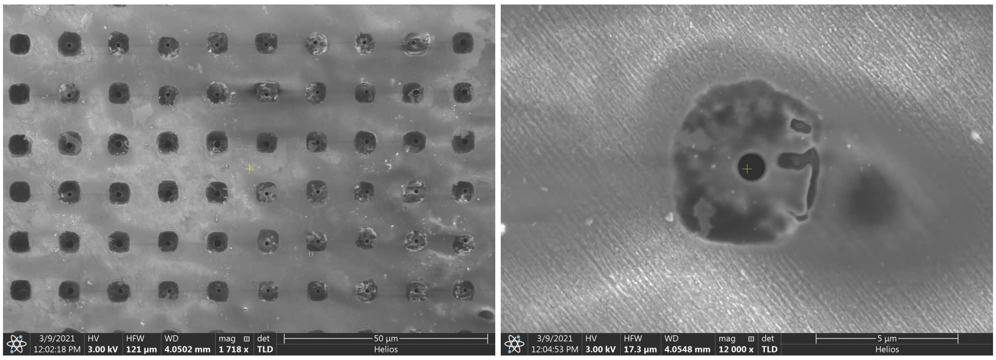

(a) Mono-layer graphene membranes.

(b) A single mono-layer graphene membrane.

Figure D.3: SEM image of mono-layer graphene membranes. The pores in the membrane are created with FIB. The white rash all over the substrate is the residue of the sacrificial layer, still present after the final step of Appendix C. A zoomed in image of one of the membranes is also shown in (b).

E POLYDIMETHYLSILOXANE CAVITIES

This chapter shows the fabrication steps for creating circular cavities in PDMS for cell trapping. An inverted design of the Si/SiO_2 substrates used throughout the thesis, is used as a mold to create the cavities in PDMS. A schematic depiction of the main steps of the procedure is shown in Figure E.1.

1. The PDMS is created by mixing the elastomer and curing agent with a ratio of 10:1 and is put in the desiccator for 15 minutes to remove air bubbles.
2. The PDMS is now ready to be placed on the silicon mold.
3. The PDMS is gently pressed into the cavities by a top plate. In this case we use a silicon wafer, as we need the relfectivity for the nanomotion experiments. A borosilicate glass or microscope slide also worked.
4. The silicon mold with PDMS is put in a oven at 85°C for 3 hours to cure.
5. The PDMS cavities on your chosen substrate can be removed from the mold by gently bending the edges of the substrate until it releases from the silicon mold.

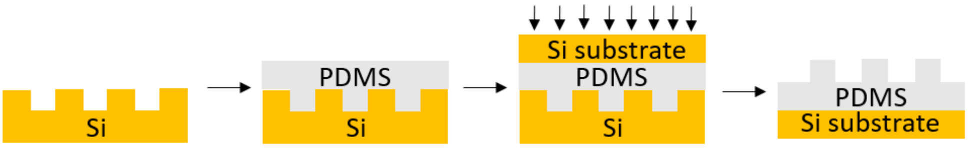

Figure E.1: Schematic depiction of the steps used to create the PDMS cavities.

Note that because of the intersection, in the schematic depiction the cavities are square but in practise they are circular. A microscopic image is shown below.

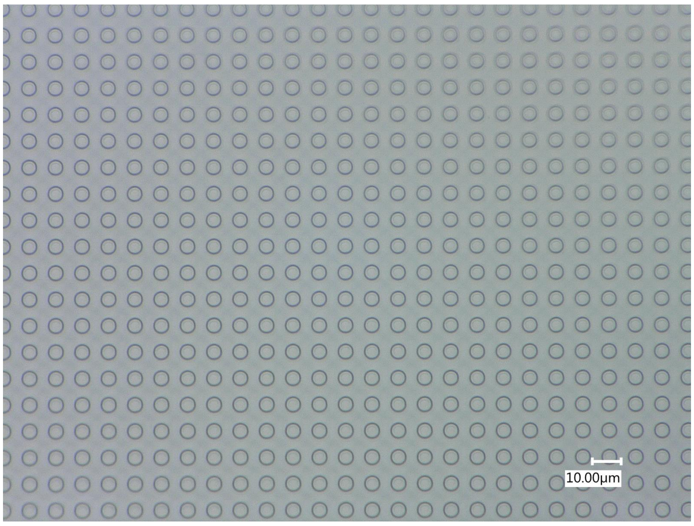

Figure E.2: Microscopic image of the PDMS cavities.

F NANOMOTION DETECTION IN PDMS CAVITIES

The PDMS cavities have also been used to measure the nanomotion of bacteria by trapping them in the cavities, similarly to the SiO_2 substrates. The height of these traps are about $1.5um$, which makes it harder for the bacteria to escape the cavities. Figure F.1 shows four screenshots of a time-laps video from a microscope with phase contrast filter and demonstrates the trapping of a single bacterium. Note the bacteria swimming in clockwise direction in the cavity due to the propulsion of the flagella [46, 65]. This oscillatory behavior is opening doors to synchronisation of bacteria.

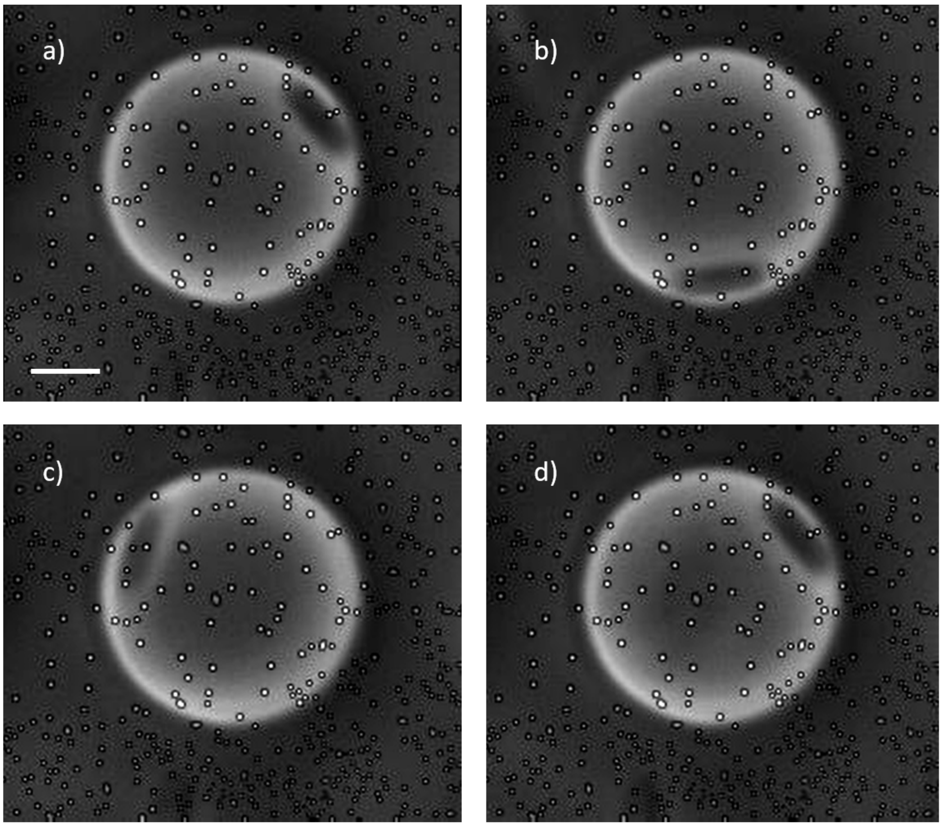

Figure F.1: Screenshots of a time-laps video of an *E. coli* bacterium trapped in a cavity. a) Is taken at 0 seconds and shows the bacterium in the north-east of the cavity. The scale bar is $1\mu m$. b) Shows the bacterium at the in the south at around 1.5 seconds. c) At 3 seconds the bacterium is in the north-west of the cavity. d) Finally the bacterium returns to its starting position after 4 seconds.

The voltage amplitude fluctuations of these trapped bacteria were measured with the same approach using the interferometric setup discussed in Chapter 4. The result of these are shown in Figure F.2 and summarised in Table F.1. Note that again the 7740 strain of *E. coli* is used and no surface functionalization has been applied to these experiments. The p-value is again determined using a two-tailed Wilcoxon rank sum test.

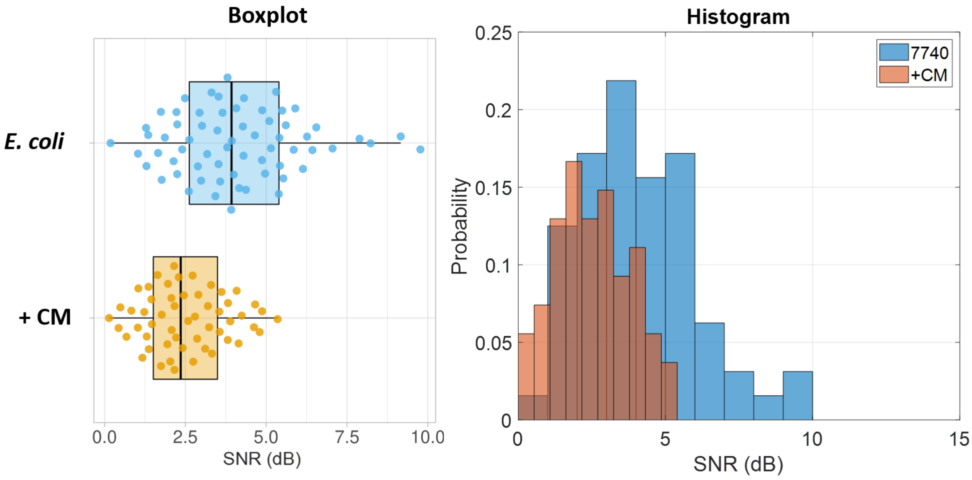

Figure F.2: The nanomotion measurements of the PDMS cavities summarised in two figures. The left figure is the boxplot showing the data prior to antibiotics with a median variance of 3.9 and 2.4 post chloramphenicol exposure (1 hour later). The median, whiskers and percentiles are the same as explained in Chapter 4. The right figure shows the histogram of the SNR (dB), with blue being prior to antibiotics exposure and red 1 hour post exposure of the same experiment.

Number of measurements	Median SNR before exposure (dB)	Median SNR 1 hour after exposure (dB)	p-value
64	3.9	2.4	5.2e-6

Table F.1: Data of nanomotion detection of *E.coli* 7740 in PDMS cavities.

The result are quite deterministic as the statistic show the low p-value. Meaning that the nanomotion experiments clearly can determine the difference prior and post antibiotics. However, comparing these results to the other nanomotion experiments from Chapter 4 we can distinctively see that the median is lower up to a factor of 5. The PDMS is transparent and has a reflextive index of 1.43 for pure PDMS, thus we would expect to see the same order of nanomotion. Note that the reflective intensity of this layer has been calculated and can be found in Appendix G. The difference can be described by the focus point of the laser spot. The laser spot is focused on the silicon surface, which is in all the other cases the direct location of the bacteria, as well. However, in the case of PDMS there is an additional layer between the bacteria and the silicon surface. Thus having the laser still focused on the silicon results in having the laser not focused on the bacteria.

G

REFLECTION INTENSITY OF DIFFERENT MEDIA

To ensure nanomotion readout, the photodiode has to receive a proper signal to exclude the noise of the system. Moreover, this will ensure a higher SNR. This means that the incident laser has to be reflected on the silicon, whilst not losing too much signal through the different media. In this thesis multiple media have been tested for nanomotion detection and this chapter shows the results of the reflection intensities of these situations. We start from the situation of a bacterium on a silicon surface and use the approach of Section 2.4. This situation represents a bacterium trapped at the bottom of a Si/SiO_2 cavity. Figure G.1 shows the result of the intensity. The intensity is showing an sinusoidal motion and is about 0.2 of the incident laser of 2mW, which is high enough for the photodiode to detect. This was expected as the reflective index of the bacterium and LB is almost equal (1.33 and 1.34 respectively). Also, with the thickness of the bacteria the intensity decreases due to attenuation in the medium, which can also be seen in the plot.

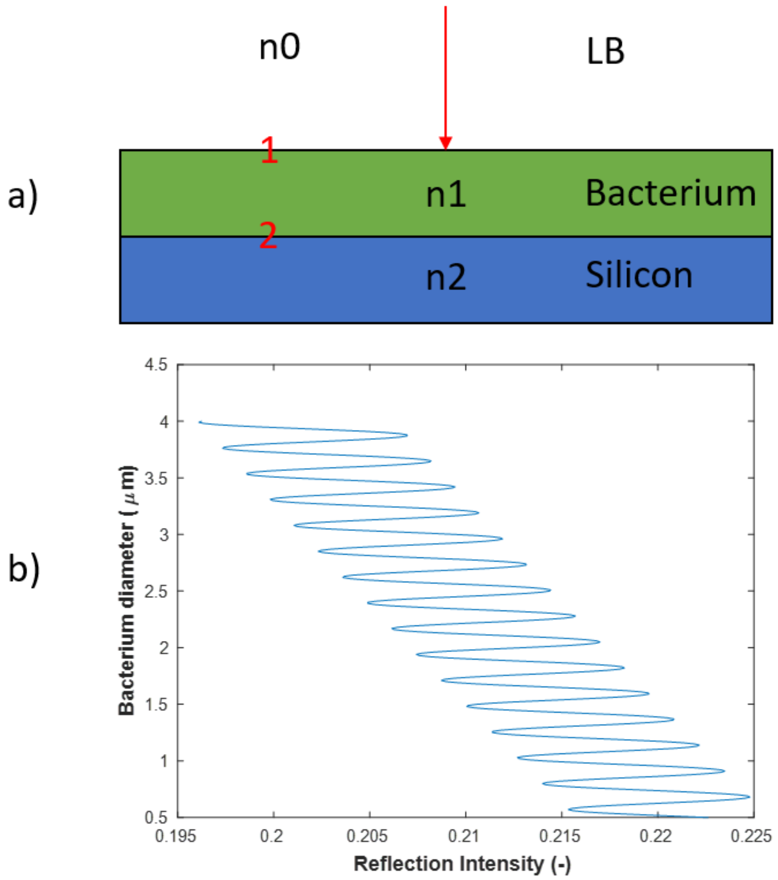

Figure G.1: Reflection intensity of a bacterium on silicon. The red arrow indicates the incident laser starting in the LB medium. a) Shows a schematic of the media and the refractive indices. b) Shows the resulting reflection intensity.

The next step is adding the additional layers and using the same method. We have two additional situations: Firstly, the PDMS cavities create an additional layer of PDMS between the silicon and the bacterium. Secondly, the situation where we measure on the Si/SiO$_2$ substrate, next to a cavity. Both situations are schematically depicted in Figure G.2. Note that the incident laser is not shown and neither the starting medium LB since the method is the same as described by Figure G.1. In the situation with the presence of PDMS, we would expect the intensity to be in the same order of the situation with the absence of PDMS, due to the transparency of pure PDMS. This is confirmed in the plot. The situation of an additional layer of SiO$_2$ shows a similar results. With an refractive index of 1.47 this was expected and is in agreement with Blake et al[38].

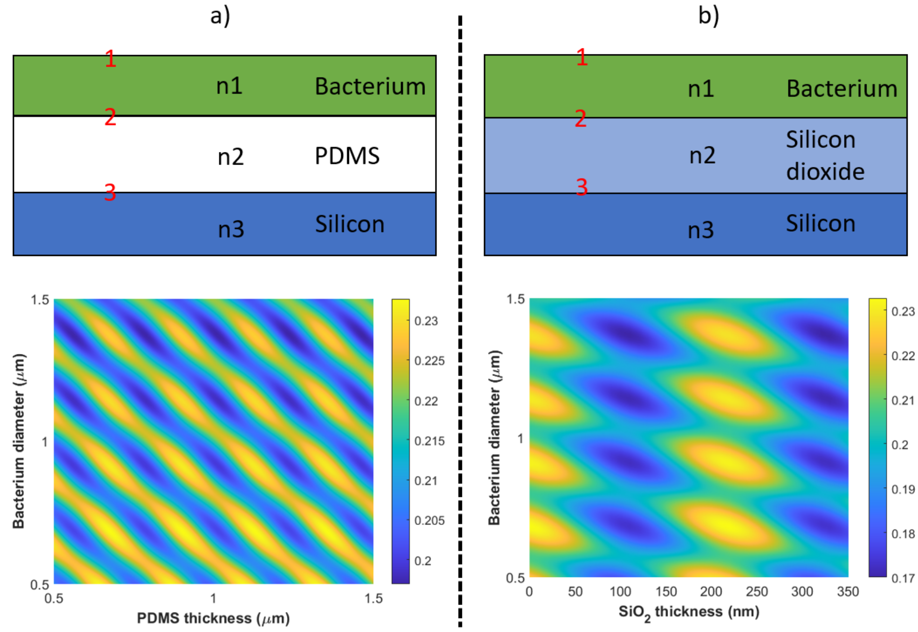

Figure G.2: Reflection intensity of a bacterium on different media. The top panels show the schematic depiction of the situation and the bottom panels the resulting intensity of said depiction. a) Shows the situation where PDMS is present between the bacterium and silicon. b) Shows the situation when measuring on the Si/SiO$_2$ substrate.

H CELL SYNTHESIS AND NANOMOTION DETECTION

The *E. coli* 7740 strain used in this thesis is rod-shaped with a length of $\sim 1.5\mu m$ and a diameter of $\sim 1\mu m$. To test nanomotion on different morphology, one could show the affect of these changes. By adding the A22 antibiotics to the 7740 strain would exhibit these changes. The A22 antibiotic targets the cell wall synthesis by inhibiting MreB filament polymerization [66]. This means that it blocks the formation of long and robust polymers of the MreB, creating no longer rod-shaped cells. The result of this are spherical *E. coli* cells[67]. A microscopic image can be seen in Figure H.1.

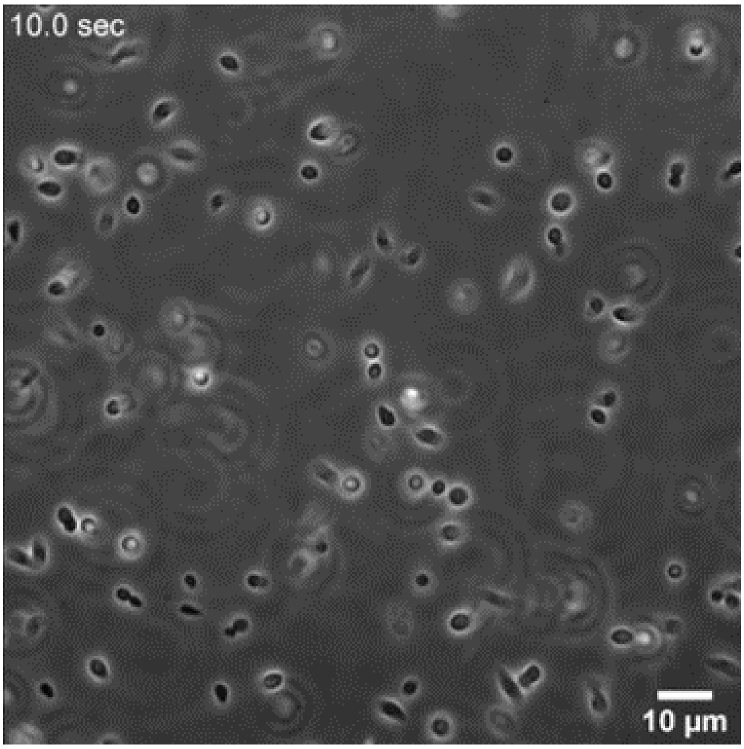

Figure H.1: A microscopic image of a the 7740 strain with the cell wall synthesis creating the morphology change. The cells are swimming freely and the black spherical spots on the image are the *E. coli* bacteria. Note the change in shape and the increase in size to about 4 μm

The nanomotion detection of the bacteria was again measured with the interferometric setup discussed in Chapter 4. The 7740 strain with A22 are measured on silicon with and without surface functionalization. In Figure H.2 and Figure H.3 the results of the nanomotion detection with and without surface functionalization are shown, respectively.

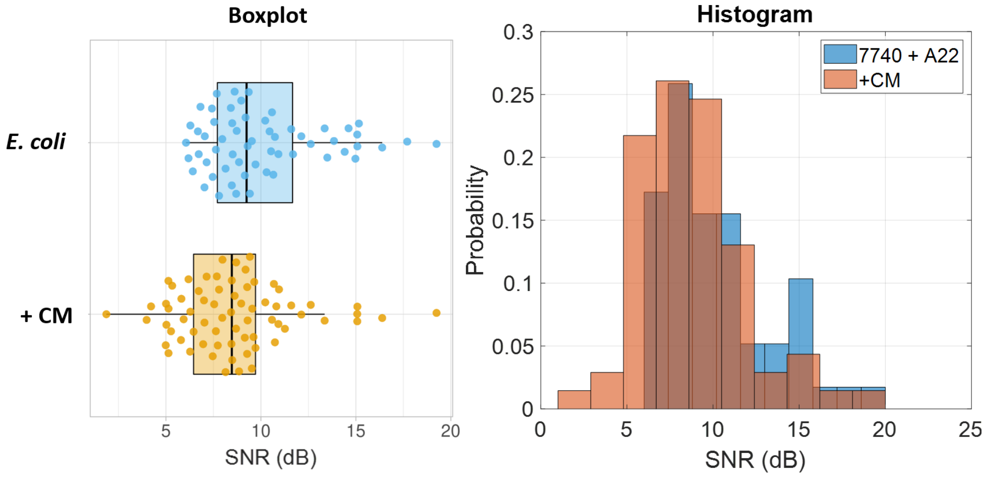

Figure H.2: The nanomotion measurements of the 7740 strain + A22 with surface functionalization summarised. The left figure is the boxplot showing the all the measurements of SNR prior and 1 hour post antibiotics exposure (Chloramphenicol). The median, whiskers and percentiles are again the same as explained in Chapter 4. The right figure shows the histogram of the SNR, with blue being prior to antibiotics exposure and red 1 hour post exposure of the same experiment.

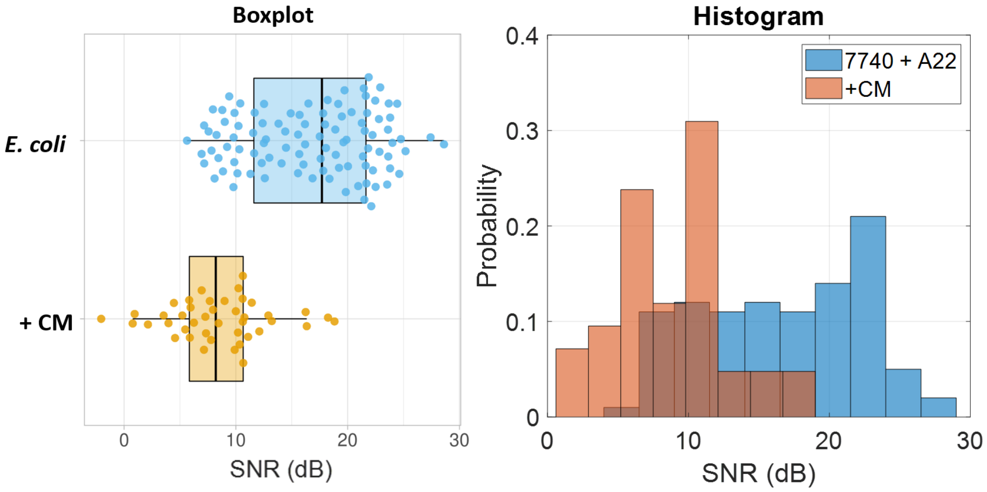

Figure H.3: The nanomotion measurements of the 7740 strain + A22 without surface functionalization summarised. The left figure is again the boxplot showing the data prior and 1 hour post antibiotics exposure and the right figure the histogram of the SNR.

The result for both the situations are summarised in Table H.1. For both the experiments there is a distinctive difference before and after antibiotics exposure and thus the statistics show an apparent low p-value for both surface funtionalizations. However, the difference between the two is enormous in the measurements prior to the antibiotics exposure. By changing the morphology of the bacteria, we change the surface area of the bacteria which is in contact with the surface of the substrate. When exposing the 7740 strain to the A22 antibiotics and measuring on the graphene drums, there was no distinctive difference, as you are measuring the deflection of the membrane. This means we can not know for sure if the surface functionalization binds silicon with a higher affinity compared to graphene. For the situations presented here, a larger area is not adhered to a flexible membrane but to a rigid surface. We are no longer measuring the deflection of the membrane but the motion of the bacteria causing a change in the interference pattern. The increase of surface area is most likely creating a stronger adhesion between the bacteria and the silicon, resulting in a less motile bacteria. This hypothesis is also based on the behavior of the bacteria observed under the microscopic videos for both the situations. Also, when comparing these results to the normal 7740 strain the motion is higher, as there is more area of the bacteria interfering with laser path for the same amount of bacteria present in the suspension. Moreover, this would mean that applying this cell synthesis on the Si/Sio_2 cavities would probably have no distinctive difference compared to the normal 7740 strain, but this hypothesis is yet to be confirmed.

Surface functionalization	**Number of measurements**	**Median SNR before exposure (dB)**	**Median SNR 1 hour after exposure (dB)**	**p-value**
Yes	69	9.2	8.5	1.3e-2
No	100	17.7	8.2	3.2e-11

Table H.1: Data of nanomotion detection of *E. coli* 7740 + A22 on silicon

I POWER SPECTRAL DENSITY PLOTS

The power spectrum of a time series describes the distribution of power into frequency components composing that signal[68]. Using Fourier analysis the physical signal can be decomposed into a number of discrete frequencies or a spectrum of frequencies. The statistical average of a signal as analysed in terms of its frequency content is called its spectrum. The amplitude of the Power Spectrum Density (PSD) is important in statistical signal processing and gives us information on the noise dominating the system and the motility of the bacterium[69]. Noise in the spectral density plots of a system given as $S(f) = constant/f^{\alpha}$, can similarly be described by the simple relation $1/f^{\alpha}$. The value of α is 1 if the system is dominated by the pink noise and 2 for random walk noise or Brownian motion. The Brownian motion dominating the system can be explained by the random motion of the bacteria as discussed in Chapter 2. The white noise is usually given as $S(f) = constant$, showing a linear line in the PSD.

In Figure I.1 three different plots of the PSD are shown. The first panel shows the difference between a graphene membrane with bacterium, a perfectly motile cell in the cavity and an empty cavity. The red line represents the fit for the graphene membrane. In both the cavity with bacterium and the graphene, the systems are still dependent for a higher frequency and are probably dominated by the motion of the bacterium, resulting in a similar trend with $\alpha = 1.9$ (close to Brownian motion). Figure I.2 shows the high trend for all the graphene measurements. However, this similar trend in α was only noted a few times (4 out of 65 measurements) for the cavity experiments, because in those specific cases the bacteria was showing a lot of motion (almost similar to that of graphene). In most of the situations the PSD varied between the optimal situation and the empty drum, an example is shown in Figure I.1b. Here cavity 1 denotes an empty drum, cavity 2 a drum with a bacterium but drastically less motion is noted and 3 again the highly motile situation. Here the situation is already changing, even though we are measuring the same sample with a bacterium in the cavity. The white noise coming from the system is becoming increasingly dominating, especially shown at higher frequency, which is shown in the decreasing trend in α (Figure I.2). This could be discussed by the same reasoning behind the change of motion in the A22 measurements: does surface functionalisation bind silicon with a higher affinity, resulting in most of the cases less motile cells? In the third panel three measurements of a cavity without surface functionalisation is shown. The trend can again be observed to show a more dominating behaviour of the noise and shows less power amplitude compared to the graphene and cavity with perfect mobility. This can be explained by the bacterium leaving the cavities resulting in again measuring the noise of the system.

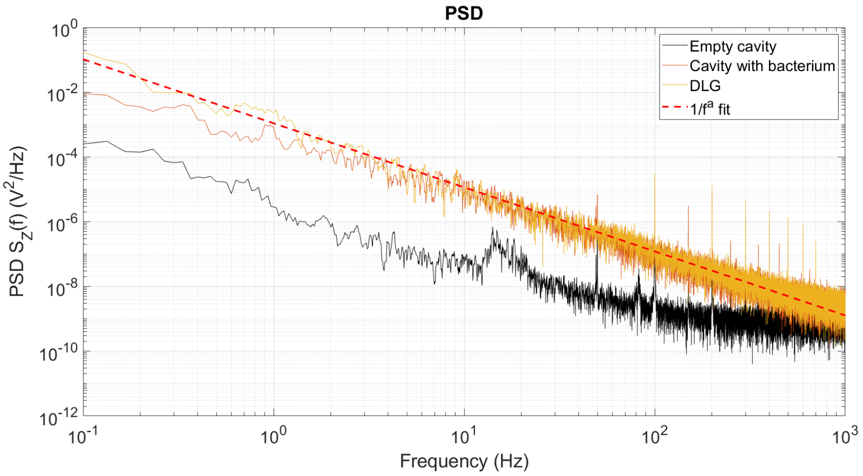

(a) The PSD of a graphene membrane, a perfect situation in a cavity and an empty cavity. The red line represents a $1/f^a$ fit on the graphene measurement.

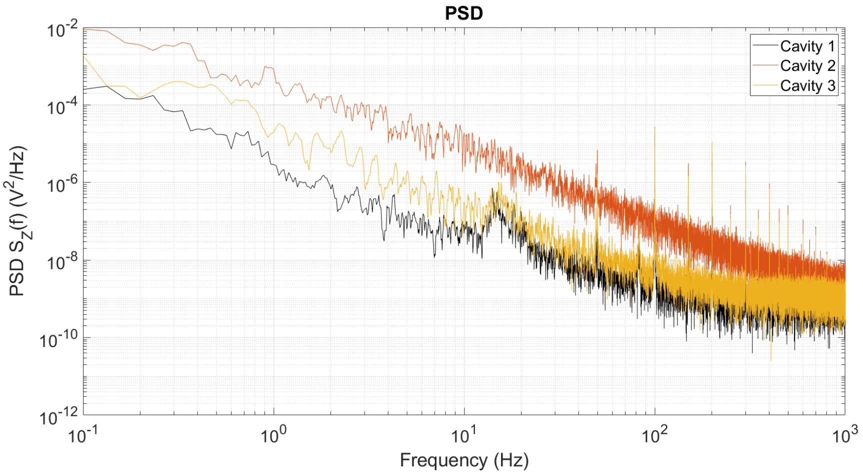

(b) The PSD between measurements of three different cavities on the same sample

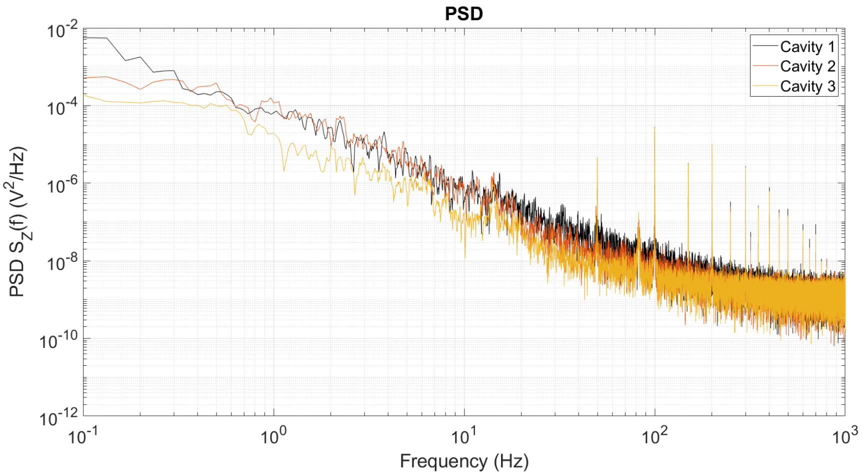

(c) The PSD between measurements of three different cavities without surface functionalisation on the same sample.

Figure I.1: PSD plots of different measurements. The peaks in all the measurements at harmonics of 50 Hz are coming from mains interference.

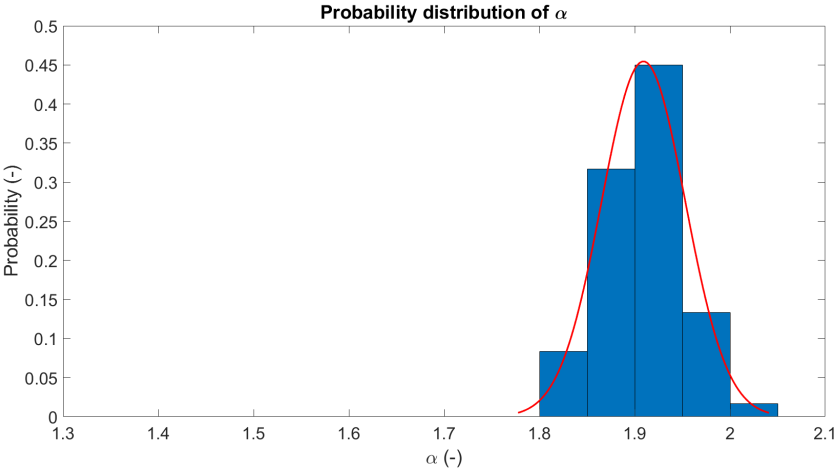

(a) The probability distribution for the graphene measurements of $\alpha = 1.91 \pm 0.05$ (mean + SD) for n=60.

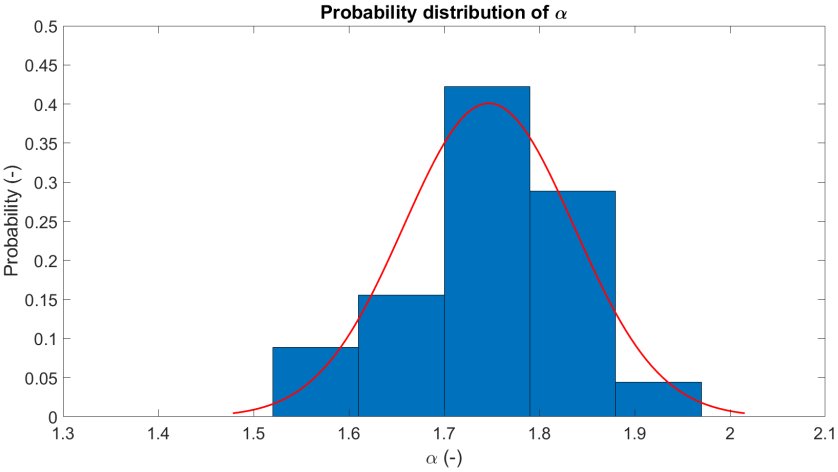

(b) The probability distribution for the cavities with surface functionalisation measurements of $\alpha = 1.75 \pm 0.09$ for n=61.

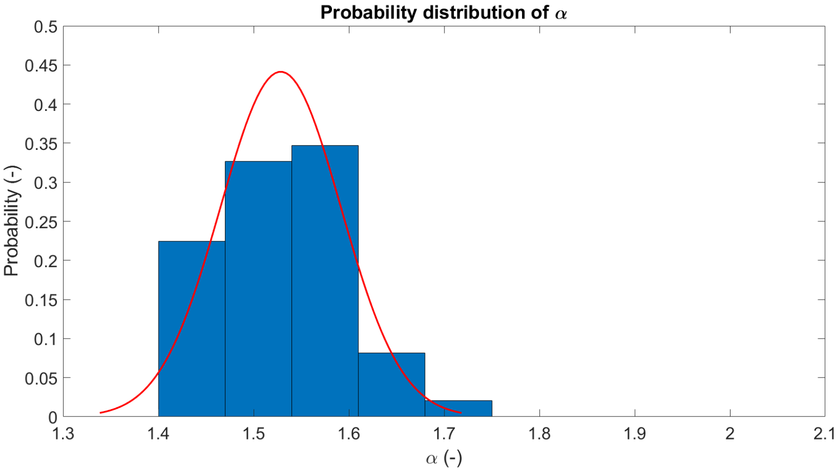

(c) The probability distribution for the LB measurements of $\alpha = 1.52 \pm 0.06$ for n=49.

Figure I.2: The probability distribution of α for three different measurements. The red lines represent a Gaussian fit. The decreasing trend in α is observed, due to the sub-missive Brownian motion.

J

LITERATURE REVIEW

Delft University of Technology

Department of High-Tech Engineering

Current and emerging techniques of nanomotion detection in bacteria

Literature survey

Author:
Stef Rodenhuis [4368746]

December 14, 2020

Contents

List of Figures

List of Tables

1 Introduction

With the incline of multiresistant bacteria due to widespread use of antibiotics, there has been an ongoing search for a faster and more effective method to test antibiotics on bacteria [1]. Current techniques on detection of bacterial resistance requiring a minimum of 24 hours to complete, a new technique is clearly essential to reduce the widespread misuse of antibiotics worldwide to combat the incline of multiresistant bacteria [2]. In the last decade a new method of this so called Antibiotic Susceptibility Testing (AST) has been on the rise, where it emphasises on the use of nanomechanical oscillators as highly sensitive sensors [3, 4]. Interestingly, due to the high sensitivity of these nanomechanical oscillators, they do not only restrict to multiresistant bacteria but could also have an enormous impact on cancer treatment therapies and outer space microbiology exploration [5, 6].

This shows the need for a simple yet precise method for AST. Though there are many different AST techniques available, graphene nanodrums are highly promising in terms of sensitivity. A recent study by Irek Roslon at Delft University of Technology shows that the nanodrums are sensitive enough to function for rapid AST. Though feasibility has been proven in terms of AST there are many uncharted territories in the optimization of this process.

The scope of this literature study is therefore not only to do extensive research into state-of-the-art AST techniques but also in single-cell isolation, dispensing single cells by printing and live imaging, in order to identify challenging knowledge gaps to be studied in the subsequent MSc-project. This MSc report will be concluded with a design and experimental results to validate the feasibility of the promising AST technique in combination with single-cell isolation and/or printing and live imaging.

The report is organized in the following sections: in section 2 an introduction on the different AST techniques is given. This is followed by the problem definition in section 3. After the problem definition the state-of-the-art is evaluated on several important topics for optimization of the process in section 4: dispensing of bacteria, single-cell isolation and live imaging, respectively. Furthermore in section 5 the results of state-of-the-art are discussed and proposes a challenging research topic. Section 6 concludes the literature review and comments on the societal relevance of this research.

2 Antibiotics Susceptibility Testing techniques

This section emphasises on the most commonly used state-of-the-art techniques for AST. Also, the pros and cons of each method are discussed and the road is paved to the current problems in this field of research.

2.1 Introduction

The variation of bacteria over the years and the vast misuse of antibiotics has created two fields of research as can be seen in Figure 1 [7]. The field of antimicrobial resistance (AMR) focuses on the prediction of antimicrobial resistance and is of paramount importance for the future antibiotics and its use. The field of AST focuses on the misuse of antibiotics and the importance of a new, rapid and affordable AST technique has already been emphasised in section 1. Moreover, the AST research is called phenotypic, which is a procedure whereby an antibiotic is added to the medium containing a certain bacteria. Figure 1 shows the classic methods for phenotypic research. However, to obtain a rapid method for AST, which is defined as being feasible within a normal 8 hours working shift, a new method is of great necessity [8].

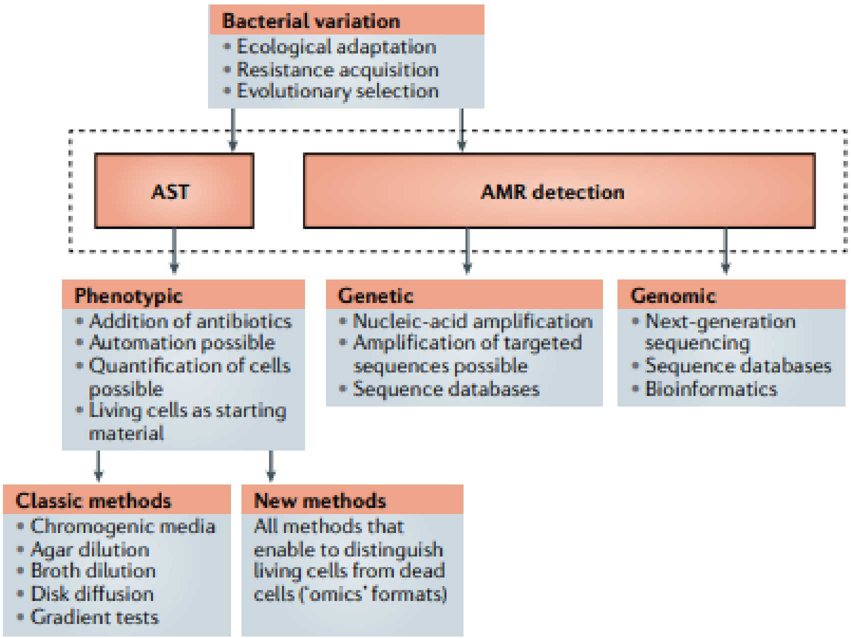

Figure 1: Schematic overview of antimicrobial susceptibility testing and antimicrobial resistance detection methods reprinted from A. Belkum et al. (2020).

Although nanomechanical oscillators have been a very promising technique, there are many other fields on the rise as new phenotypic methods. This can be seen in Figure 2. This chart includes the toolbox, read-out and more importantly: single cell suitability. A few of these techniques and their state-of-the-art designs are discussed next.

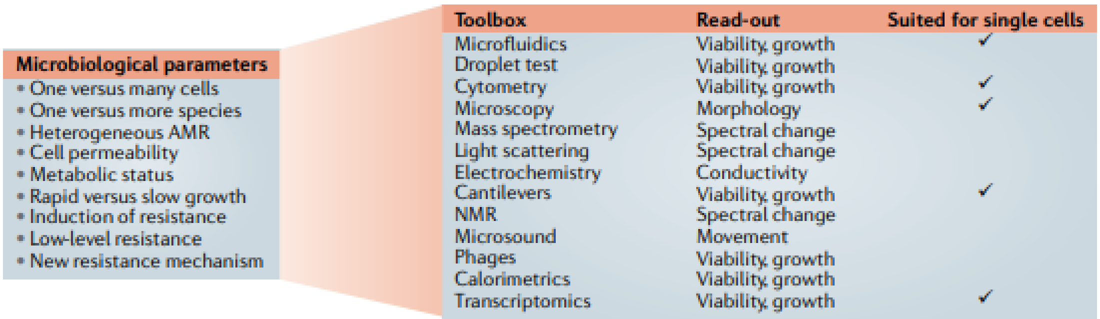

Microbiological parameters

- One versus many cells
- One versus more species
- Heterogeneous AMR
- Cell permeability
- Metabolic status
- Rapid versus slow growth
- Induction of resistance
- Low-level resistance
- New resistance mechanism

Toolbox	Read-out	Suited for single cells
Microfluidics	Viability, growth	✓
Droplet test	Viability, growth	
Cytometry	Viability, growth	✓
Microscopy	Morphology	✓
Mass spectrometry	Spectral change	
Light scattering	Spectral change	
Electrochemistry	Conductivity	
Cantilevers	Viability, growth	✓
NMR	Spectral change	
Microsound	Movement	
Phages	Viability, growth	
Calorimetrics	Viability, growth	
Transcriptomics	Viability, growth	✓

Figure 2: New phenotypic methods from A. Belkum et al. (2020).

2.2 State-of-the-art

2.2.1 Microfluidics

The first auspicious technique is called the method of microfluidics. Microfluidic processes small amounts of fluids in an integrated microchannel to obtain bacterial culture analysis and hence is a prominent AST technique. Usually it constraints bacteria in a channel and the process is monitored in real-time. Such a chip is shown in Figure 3 [9].

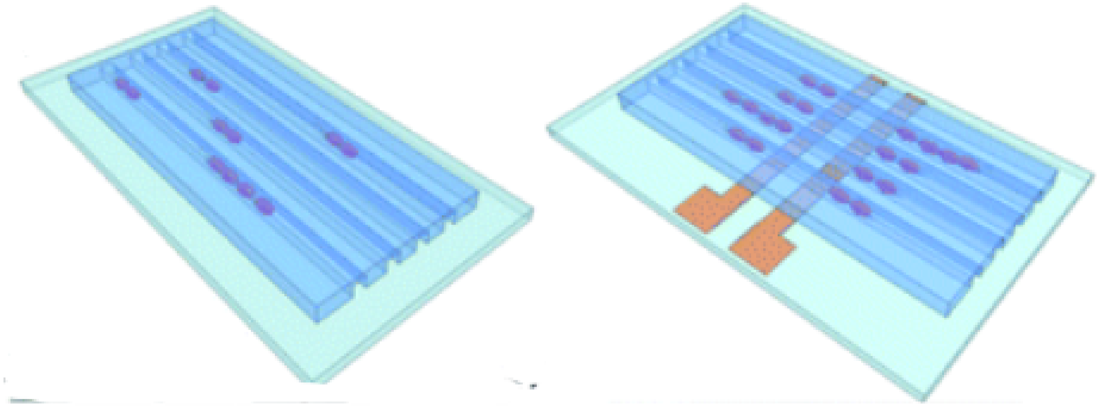

Figure 3: A basic microfluidic chip with microchannels for AST from Zhang et al. (2020).

The principle of this method is based on tracking a single-cell under the microscope and hence determining the susceptibility of an antibiotic in a few hours. Moreover, besides being slightly time consuming the current used systems are not automatic and need handling steps from a professional and/or image processing techniques. According to Zhang et al. (2020) and Blair et al. (2015) to speed up this process, not the cell viability should be measured but merely the biological reaction on molecular scale [10,11]. This would need a highly sensitive nanotechnology to measure biological reactions, which will be discussed separately in subsection 2.3.

2.2.2 Microfluidic cantilever

Not only has the need for sensitive nanotechnology been explained in the previous section, it has already been applied to the field of microfluidics. A very interesting paper has been published by H. Etayash et al. (2016) on this topic achieving single-cell per μL sensitivity [12]. Figure 4 shows the schematic overview of this novel approach. The microfluidic channel is embedded in the cantilever and the sample containing the bacteria is flowing through this channel. The resonance frequency (mass change), and the deflection of the beam (surface stress) are measured simultaneously, resulting in a very high sensitivity. Both these approaches of measurement are explained more thoroughly in subsection 2.3. Also, the ratio between infrared radiation and infrared absorption of the bacteria is measured for identification of living cells. The combination of approaches are needed to ensure that the cell is alive, as the resonance frequency will also show dead cells. Unquestionably, the combination of multiple approaches and the limitation of high throughput was leaving room for improvement.

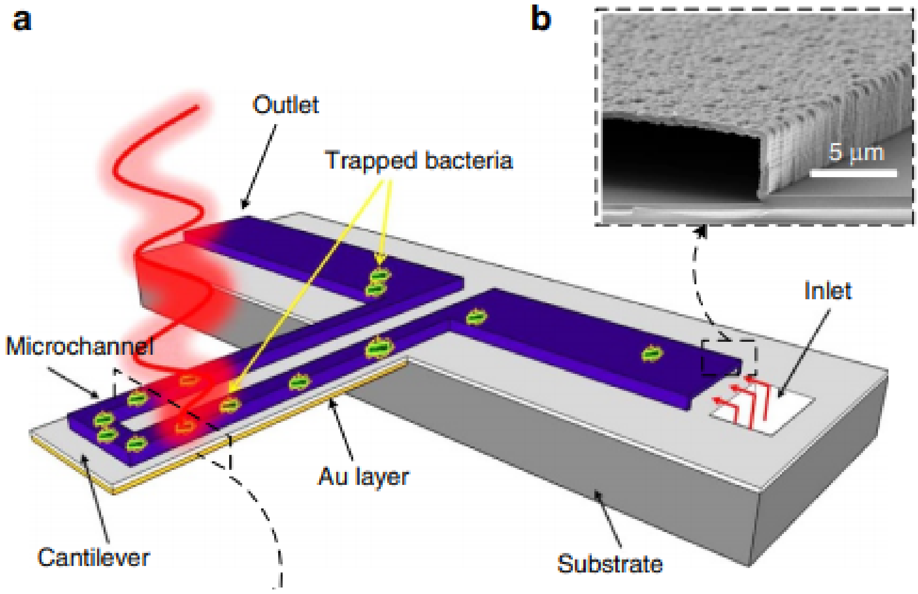

Figure 4: Schematic overview microfluidic cantilever from H. Etayash et al.(2016)

This problem could be resolved using an array of microfluidic cantilevers as has been explained by N. Cermak et al. (2016) [13]. In Figure 5 one can see the working principle of the array of cantilevers. The resonance frequency is measured for all the cantilevers to obtain same cell recognition. Though this method resulted in a 150 bacterial cells per hour resolution, this method is rather difficult to implement. Also, this method is prone to clogging of bacteria at the tip of the cantilevers if not flushed correctly and/or needs delay channels as explained in the paper. However, this hybrid between the two tools of cantilevers and microfluidic, intrigues the field of research not to merely focus on one tool only.

2.2.3 Flow cytometry

Another promising technique is based on flow cytometry. In flow cytometry the cells are flowing through a channel and aligned using for example acoustic focusing [14]. The cells are now in the centre of the channel and can easily be read using various techniques. The most common method used is optical characterization, which needs staining of the cells. During this process there is a spectral shift and the fluorescence intensity increases if one compares dead cells with living cells. Commercially there is a wide variety of flow cytometers, like the 2020 Attune NxT Flow Cytometer, which are showing a very high throughput up to 35.000 events per second [15]. Though this method is favorable in terms of throughput and time consumption, it has the downside of requiring labeling or staining the bacteria. Moreover, it limits the user to detecting things that the user knows how to label. Also, flow cytometry is commonly used for single-cell isolation and will be discussed more in depth in subsection 4.2.

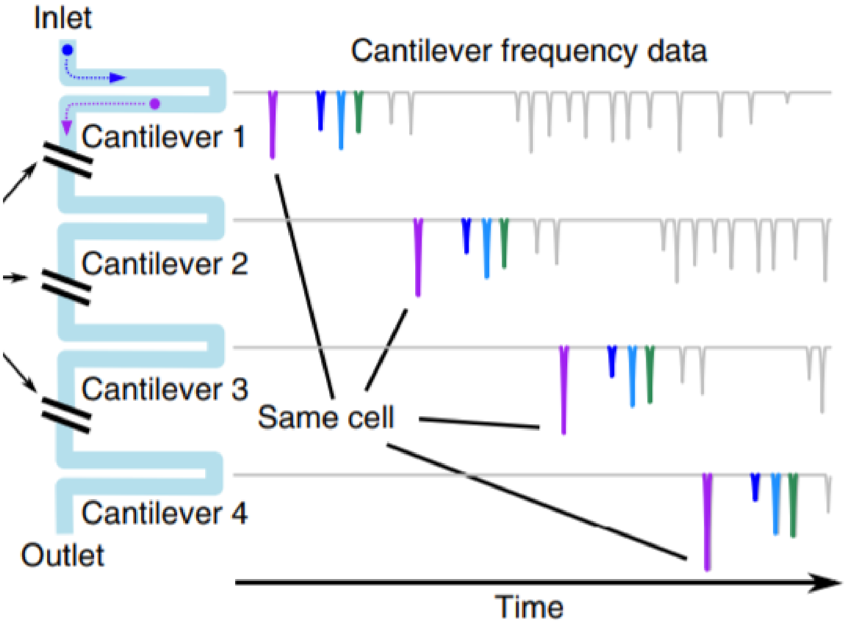

Figure 5: Working principle of an array of microfluidic cantilevers by N. Cermak et al.(2016)

2.3 Cantilever AST

Cantilevers, or nanomechanical sensors, are discussed separately due to its already extensive field of research and favorable time consumption for AST. The nanomechanical sensors used in AST evolved from Atomic Force Microscopy (AFM) as they currently reach a distinguished performance in terms of sensitivity. This means that even thermal and brownian motion will be detected by the cantilevers, therefore they will spontaneously oscillate [16]. These oscillations have a very low amplitude and hence the influence of a living sample can drastically been seen. The nanomotion of bacteria on the nanomechanical oscillators can be measured either in the dynamic or in the static mode [16]. In the dynamic mode, the cantilever is driven at its resonance frequency. As soon as a bacterium is attached to this cantilever, there will be a shift in resonance frequency due to the added mass. In this mode the sensitivity of the performance depends on the resonance frequency and the quality factor, which depends on the sensing medium. Meaning that the sensing medium can strongly influence the dynamics of the cantilever for example due to viscous damping [17]. Due its simplicity the cantilever can be modelled as a harmonic oscillator and the frequency can be calculated as follows:

$$f = \frac{1}{2\pi}\sqrt{\frac{k}{m}} \tag{1}$$

where k is the cantilever spring constant and m the effective mass.

In the static mode a bacterium attaches to the surface of the nanomechanical sensor and the deflection can be derived from the change in the surface stress, of course being either compressive or tensile stress. The surface stress in caused by interaction between the cell and the cantilever i.e. electrostatic, entropy and more [18]. In the static mode the sensing medium has a negligible influence on the measurement and hence is preferable when working in a liquid environment. The surface stress can be described by Stoney's equation [19]:

$$\Delta\sigma = \frac{Et^2}{3(1-\nu)L^2}\Delta z \tag{2}$$

where E is the Young's modulus, t the thickness of the cantilever, ν the Poisson coefficient and L the length of the cantilever.

Extensively, one can say a third mode is present based on nanomotion of bacteria. This approach does not focus on the deflection due to surface stress or on the frequency shift due to change of mass but merely on the amplitude increase of the oscillations due to biological nanomotion. After functionalizing the cantilever, resulting in bacteria or other living cells adhering to the nanomechanical oscillators, the amplitude of the oscillations increase vividly. Moreover, nanomechanical sensors convert the biological motion, which mainly comes from metabolism, into mechanical motion [20]. This motion can be measured, including the addition of antibiotics, within 30 minutes after adding the sample with the bacteria. A good example is shown in Figure 6, where the difference between amplitudes can clearly be noted [21].

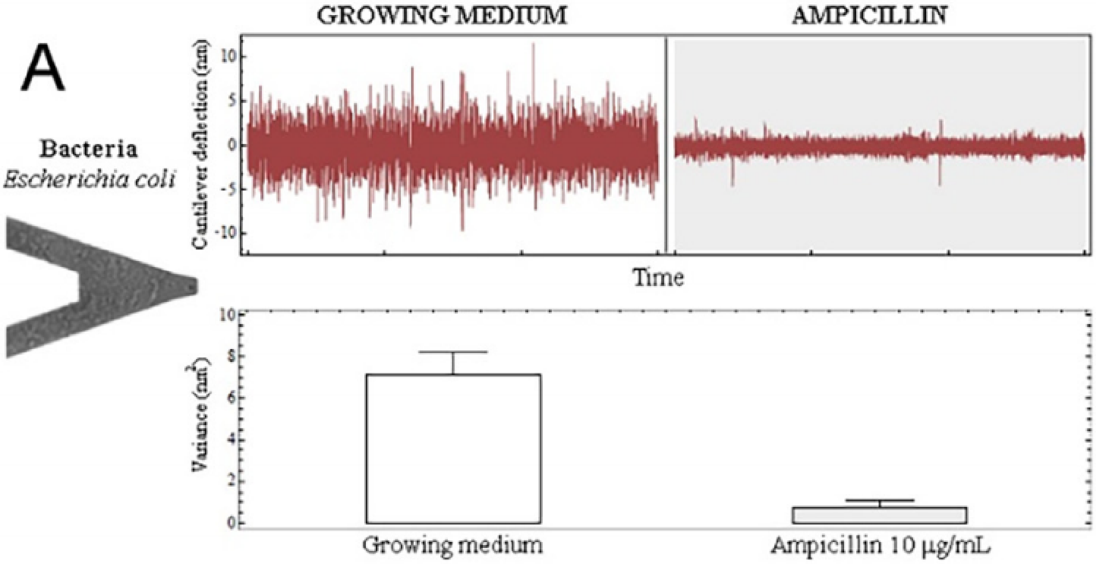

Figure 6: Deflection and variance of E. coli bacteria in a growing medium and with ampicillin, respectively from G. Longo et al. (2019).

2.3.1 Readout techniques

The AFM cantilevers for the AST are highly sensitive, reaching mechanical responses up to the order of angstroms, the readout techniques have to be extremely sensitive as well. The last few decades the optical beam deflection, piezoelectric and the piezoresistive are the most popular readout techniques [16].

The optical beam deflection(OBS) is a method widely used in deflection measurements due to its simplicity to implement. The OBS dates all the way back to 1988 and was a novel approach to AFM [22]. A laser is focused on the cantilever and reflected to a position sensitive detector (PSD), which detects electric current differences. A graphical explanation can be seen in Figure 7 [23]. Though this method is highly accurate, the disadvantage is the alignment, the re-calibration of the system and only works with reflective cantilevers or coatings.

The second common method is integrating piezoelectric or piezoresistive material in the cantilever. One of the biggest advantage compared to the OBS method is the possibility to work with an array of cantilevers. The piezoresitive usually uses the well-known Wheatstone bridge(WSB), a device for detecting small difference in resistance [24]. Additionally, the WSB runs a small current and converts the change in resistance into a voltage, which is equivalent to the surface stress in static mode. In dynamic mode piezoelectric cantilevers are more common, as they are able to self-excite by electric actuation. Moreover, this principle works both ways, so instead of being excited it can generate internal electrical charge, hence also being used in the field of research in Energy Harvesting [25]. However, there are two drawbacks in the electrical detection method in

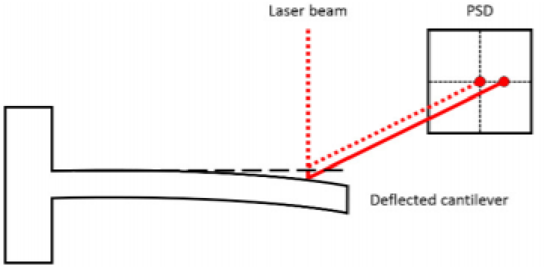

Figure 7: Optical beam deflection readout from H.Gonzales-Rivera et al. (2017).

comparison with the OBS. The first drawback is the approach has larger electrical noise than the optical method [26]. Secondly the electrical detection method has the need for additional material to the cantilever, which can highly influence your dynamic mode of the system, or one has to fabricate the transducer using piezoelectric material.

2.3.2 Materials

Though there are many different kind of nanomechanical sensors they do not immensely vary on dimensions, shapes or fabrication methods. The main feature that extinguishes all these types of senors is the transducer type used, ergo the material used for the cantilever. Not only does the material highly affect the characteristics of the mode but also the coating is of paramount importance. M. Alvazer et al. (2020) summarises the nanomechanical sensors used for AST of the last 2 decades [16]. A few very promising results are summarised in Table 1, including the transducer type and sensitivity. Table 1 clearly shows some variations between the transducers by means of materials. This paves the road to new and exciting material choices. Note that the sensitivity is not only dependent on the material but also on the mode (static or dynamic) and medium.

Table 1: A few promising nanomechanical sensors from M. Alvazer et al. (2020).

Transducer type	**Medium**	**Sensitivity**	**Mode**
Silicon nitride MC [27]	Air	1 cell	Dynamic
PZT MC [28]	Liquid	1 cell/mL	Dynamic
Suspended silicon microchannel [29]	Liquid	1 cell	Dynamic
Silicon nitride microfluidic gold-coated MC [30]	Liquid	1 cell/μL	Static

2.4 Discussion and conclusion

The field of AST has been under a tremendous development over the last few decades. The demand for a rapid AST due to the misuse of antibiotics and the variation of bacteria is forcing this rapid development. Though there are many fields or tools applicable and many methods have been proposed, all lack either affordability, high throughput or rapid AST. This section discussed the different tools and their pros and cons, resulting in the same conclusion.

The cantilever or nanomotion toolbox has a interesting stance in terms of the most important aspect: rapid measurements and therefore is favorable. However, the current state-of-the-art often needs a cultured sample to have a high dose of bacteria, which will be explained in the next section. Also, to obtain multiple measurements an array of cantilevers is needed, which is rather difficult to implement and quite space-consuming. The current state-of-the-art AST techniques show there is optimistic perspective for a rapid AST, when not merely focusing on one toolbox. There has been shown that there is big room for improvement not only in a hybrid of the toolboxes but also in the material and design of the nanomechnical oscillator.

3 Problem definition

In section 2 there has been shown that in the field of AST already broad research has been conducted on the tools for AST, its readout techniques and materials for a few decades now. Recently, a new door was opened in the nanomotion toolbox, choosing a different path than the classical cantilevers. The study by Roslon et al. (2020) shows that graphene nanodrums are highly sensitive and do properly function for AST. In this study, like the other cantilever AST studies, the nanodrum is submerged in liquid containing a high dose of the bacteria. During this emerging, bacteria will adhese to the surface of the nanodrums after gravitational sedimentation. This means a high Colony Forming Units(CFU) is needed to make sure there is going to be bacteria on the nanodrums before doing experiments, hence the bacteria have to be cultured, again being time consuming.

To obtain a faster(<8 hours) and more precise measurement, e.g. single bacteria sensitivity, by other means than emerging the nanodrum in a high CFU liquid, is desired. Not only does this change affect the dispensing method of the bacteria, but also making sure one bacterium is at a nanodrum would need some filtration i.e. microfiltering, creating new challenges to unravel.

Another viable and exciting challenge is the live imaging during the experiments. The nanodrums can be observed with a microscope before advancing to the AST measurements, but during the experiments live imaging would open the door to exhilarating topics. Moreover, not only can one visualise the bacteria on the nanodrums but also enhancing to a phase of image acquisition can enable live tracking of the bacteria.

Note that not only the above mentioned challenges are to be unraveled but also other challenges arise during this new method for AST. For example, to obtain a precise measurement of the oscillation, the readout techniques described in section 2 are no longer feasible. Hence a new approach has to be established, using fabry-pérot interferometry instead of optical or electric detection. Moreover, a calibration is needed to ensure this method is accurate, as one does not surely know the medium between the silicon and the graphene layer. Lastly, there might even be more challenges which we will encounter along the way but for now the main issues have been discussed in this section.

In Figure 8 one can see the current experimental set-up, including the chip with the graphene nanodrums, fabry-pérot interferometry and also a microscopic image of the chip containing a high dose of bacteria.

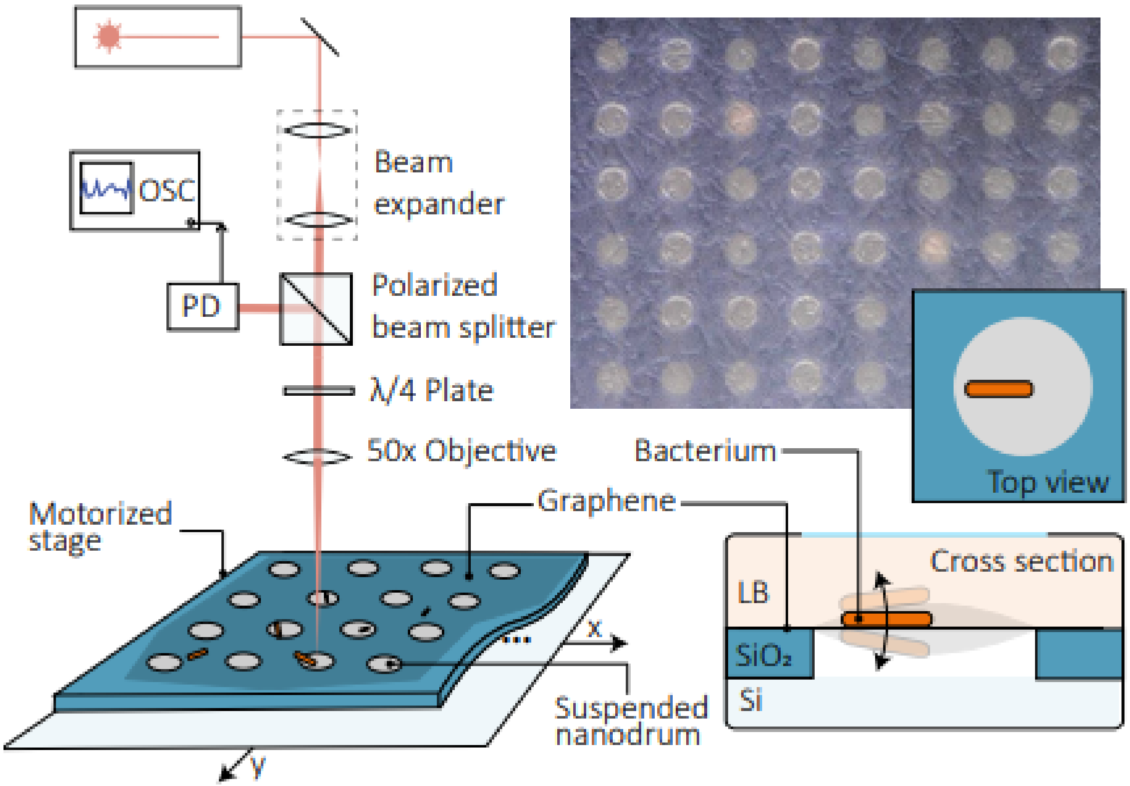

Figure 8: Working principle current set-up. Courtesy of Irek Roslon, Tu Delft (2020).

4 State-of-the-art

This chapter presents the state-of-the-art techniques to identify knowledge gaps in the dispensing of bacteria and single-cell isolation techniques. Both the pros and cons are discussed for both the methods to sort out the technique to be designed in the subsequent MSc-project. Also, the state-of-the-art live tracking of bacteria is discussed in this section, which merely focuses on the recognition of E.coli bacteria.

4.1 Dispensing of bacteria

In the last few decades inkjet printing has become a more popular field of research for printing e.g. lithography or transistor circuits [31]. This method is intriguing due to its high-resolution and affordability. More recently, inkjet printers are becoming more and more popular for bio-printing as it is seen as one of the most promising methods of transferring bioactive materials, such as bacteria, using a noncontact method [32]. This method of dispensing of bacteria is not only affordable but also has a high throughput, which makes it desirable for handling bacteria in AST. The commercially available and mainly used printers are currently the piezoelectric and the thermal inkjet. This section discusses both methods and concludes on the use of inkjet printing for dispensing bacteria. Note that this section centralises the available options at the university, factoring in the affordability.

4.1.1 Thermal inkjet printing

Thermal drop-on-demand (DOD) printing, as well as piezoelectric DOD printing, has been around since the 1970's. This method was inspired by the process of boiling water where it forms bubbles and hence has a convenient working principle. The working principle will be explained using Figure 9 [33]. The ink in the chamber is rapidly heated up (to a high temperature of about 350°C) to vaporize the ink in the chamber. Similarly as in the concept of boiling water the vaporizing creates a bubble. This bubble will create a pulse due to the pressure and will push ink through the nozzle. As the ink gets ejected, the bubble will collapse and the chamber refills again with ink. The process can now be repeated.

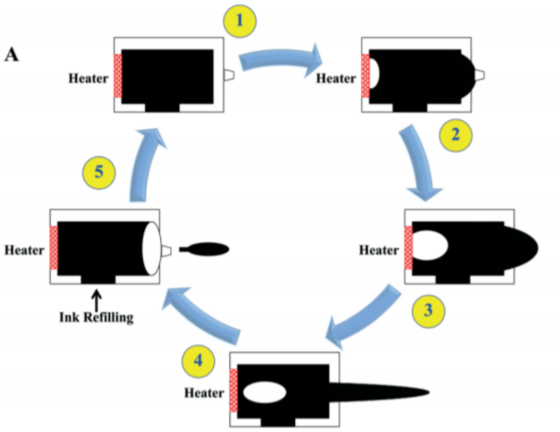

Figure 9: Working principles of the thermal DOD printer from J. Li et al. (2015).

In Xu et al. the thermal inkjet printing has been used to obtain colony arrays of E. coli [34]. Droplets with a high-density bacteria were ejected on a substrate and later incubated at 37°C to obtain the colony arrays. The high viability is therefore achieved due to this high-density. A rather low-density with high viability has not yet been achieved. Moreover, the E. coli bacteria is vulnerable to heat and the working range of 350-400°C of the thermal printing has a negative impact on the viability. However, the short duration of the pulses, around 10 ms, ensures most bacteria survive. Nevertheless, not much research has been conducted on lower-density.

4.1.2 Piezoelectric inkjet printing

Though piezoelectric DOD inkjet printing has been around as long as thermal DOD inkjet printing the research conducted is more extensively in the field of bioprinting, as there is no substantial heat treatment. The working principle of the piezoelectric is graphically explained in Figure 10. The chamber with ink is surrounded by Piezo-ceramic material, which deforms due to an applied current. This again, similarly to the thermal DOD printer, creates a pressure wave, ejecting the ink out of the chamber.

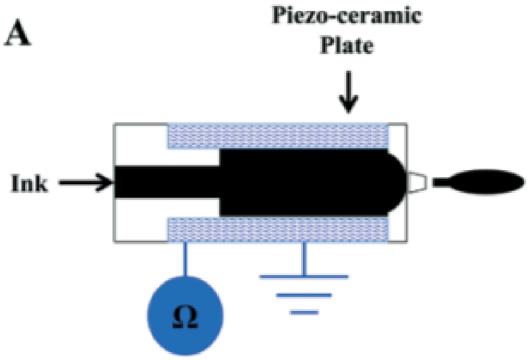

Figure 10: Working principles of the piezoelectric DOD printer from J. Li et al. (2015).

The piezoelectric DOD inkjet printer is a more commonly used method for printing of bioactive material, as has been explained in the previous section. Literature shows that piezoelectric printers can be used to print small droplets, in the order of picolitres, onto a flat surface at high resolution with a viability exceeding 98.5% [35]. Also, since we are striving to achieve single cell sensitivity, besides achieving the high viability, Merrin et al. has very promising results on the distribution of cells per droplet, as can be seen in Figure 11.

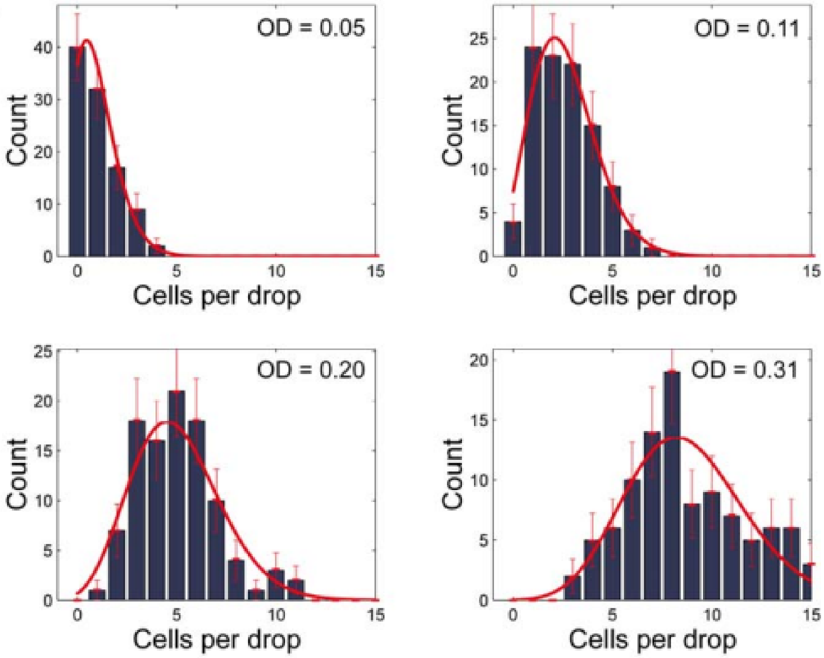

Figure 11: Distribution of cells in a single droplet for varying densities from Merrin et al. (2007)

4.1.3 Discussion and conclusion

Over the years Inkjet DOD printing has shown to be a viable method for dispensing of bacteria. Not only has there already been research on the printing of E. coli bacteria but also a high viability has been achieved. There can be concluded that no knowledge gap is present and piezoelectric DOD printing has the preference over thermal DOD printing, due to the obvious reason of higher viability. Though the printing of bacteria is feasible, one has to keep in mind that the printers vary on some features for every model e.g. printer head and nozzle size. This means that certain factors have to be taken into account to achieve high-resolution and high viability, namely: viscosity, clogging, nozzle size, CFU, surface tension and printing solution [35,36]. Consequently, the Reynolds number, Weber number and the Ohnesorge number are of paramount importance. Numerically is said that a drop formation is stable if $1 > Oh > 0.1$. The formulae are shown below, respectively.

$$Re = \frac{\rho d \nu}{\eta} \tag{3}$$

$$We = \frac{\rho d \nu^2}{\sigma} \tag{4}$$

$$Oh = \frac{\sqrt{We}}{Re} = \frac{\eta}{\rho d \sigma} \tag{5}$$

where ρ is the liquid density, d the nozzle diameter, ν the speed of the droplet, η the viscosity and σ the surface tension.

Note that these printers have a rather low repeatabilitiy and accuracy looking at micro-scale [36]. The Epson Stylus SX235W printer available at the university has a standard deviation of $5.4\mu m$ and $8.4\ \mu m$ in the vertical and horizontal direction, respectively, when printing picolitre size droplets. Since the chip, with the nanodrums, is $5x5mm$ the accuracy and repeatability is not of paramount importance. However, to ensure the objectives are met, there is also a high-end printer available at the university, namely the pixdro LP80. Though this printer is preferred in terms of accuracy and precision, the downside of this printer is the high cost.

4.2 Single-cell isolation

Though there many high-end machines on the commercial market for single-cell isolation, one would need a high precision machine to place a living bacteria on a nanodrum after the isolation. Moreover, a cheap and simple yet elegant single-cell isolation is desired for this designed purpose. This section discusses the 5 frequently used methods for single-cell isolation and concludes on feasibility for this specific problem [37, 38].

4.2.1 Fluorescence activated cell sorting

Fluorescence Activated Cell Sorting or FACS is basically a flow cytometry. In this process, cells are firstly stained by fluorescent dye so that they can be optically detected. Next, a sample containing the cells, is driven through a flow cell. In this flow cell the cells pass a laser beam and the optical detector. The Fluoresecent cells are then sorted by using electrically charged plates (electrostatic deflection). This working principle is graphically shown in Figure 12. One of the biggest advantages of this method is the high throughput as FACS has been widely used for isolation of cell populations. Nevertheless, Schulz et al. has shown that single-cell isolation is also possible using flow cytometry [39]. However, this method needs to make sure there is a low CFU pressent for single-cell isolation and a small delay between cells going through the flow cell (or non sticky). Also, though this method is promising in terms of cell population isolation, big disadvantages are the need for a precision placing machine and building the set-up for FACS after single cell isolation. Note that there are already commercial single-cell isolation machines available, that even include deposition on a desired location, but are not within the range of cost.

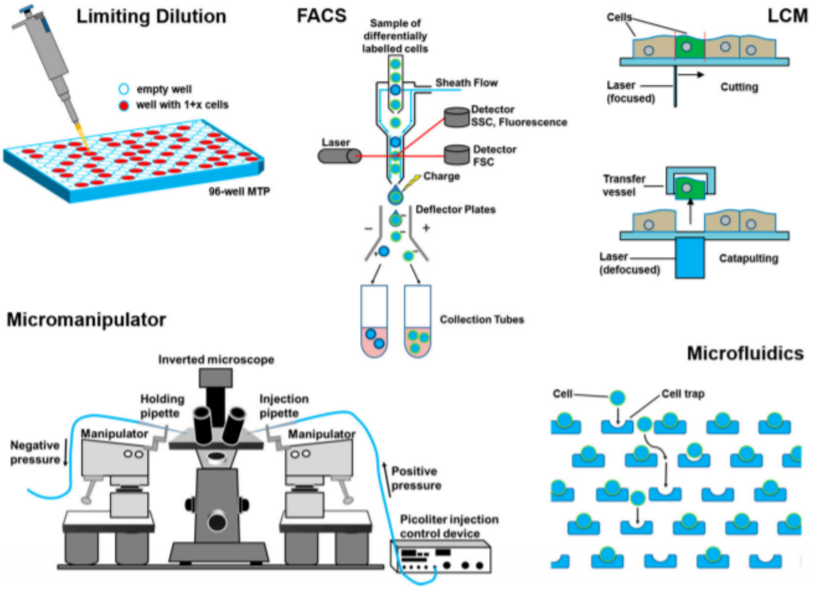

Figure 12: Overview of the single-cell isolation techniques from A. Gross (2015).

4.2.2 Laser capture microdissection

Laser capture microdissection(LCM) is promising technique for single-cell isolation [40]. There are a few variations of the working principles but they all boil down to roughly the same method. A section of one cell is cut off using a laser and the desired cell is extracted using either a transfer vessel or adhesive cap as shown in Figure 12. This technique has not been analysed as it is used to isolate cells from tissue and will not be considered in the design.

4.2.3 Limiting dilution

Limiting dilution is the method of single-cell isolation by diluting the suspension, containing the cells, and combining statistical distribution. From previous literature has been concluded that the cells are based on Poisson distribution and so the sample can be highly diluted to statistically achieve 1 cell [41]. This method either needs an educated guess of the amount of cells present in the sample or needs to approximate the number of cells by growing from a single-cell [37]. Moreover, the probability to achieve 1,2,3 or 4 cells is 61%, 30%, 1% and 0%, respectively. Also, since this method is using hand-pipettes, again a placing machine is needed. These disadvantages substantiate the irrelevance of this method and will not be considered in the design.

4.2.4 Manual cell picking

A simple and convenient method for single-cell isolation is manual cell picking or micromanipulation. A small amount of the suspension, usually in the orders of picolitres, is observed under an inverted microscope. Each cell passing through the microscope is observed and manually analysed. Micro-pipettes driven by motorized mechanical stages are then used to isolate the single-cell. The schematic working principle can again be seen in Figure 12. A few big disadvantages is that this method requires a highly skilled professional and has limited throughput. Also, again a precise placing machine is needed. Though this method is highly favorable for handling bacteria, the previous mentioned disadvantages opposes the consideration of this method [42].

4.2.5 Microfluidics

The final method commonly used in single-cell isolation is called microfluidics. This principle is based on processing small(nano- to atto-litre) amounts of fluid using channels or channels-like structures, usually at the micro-scale [43]. Though this method needs fabrication up to micro- or even nano-scale, microfluidics is a powerful tool to achieve high sensitivity, high throughput and low costs. Hence this field has a broad field of research and the principles differ from droplet-in-oil-based isolation to pneumatic membrane valving to plain hydrodynamic trapping [44–46]. The droplet-in-oil-based isolation is mainly used for random distribution of cells and is therefore not considered. The method of pneumatic membrane valving needs some kind of cell detection unit, using time-lapse microscopy with automated image acquisition or manual microscopy and therefore does not meet the requirements. The method of hydrodynamic trapping is shown in Figure 12 and is the most commonly used for single-cell isolation due to its simplicity and effectiveness. This method has high potential for single-cell isolation after printing the droplets onto the chip, hence a few distinguished state-of-the-art designs will be discussed on this topic.

Recently, microwell array chips are becoming an interesting topic in the field of microfluidics [47,48]. A chip usually consists of thousands of wells, with the diameter and depth in the order of micrometers, depending on your requirements. A small pore, again the diameter depending on your requirements, is created at the centre of the wells. A small negative pressure of usually around 10mbar is applied across the microwells and the suspension containing the cells will flow through the pores. The flow through a pore will be blocked as soon as a cell is trapped in the well. A schematic depiction can be seen in Figure 13.

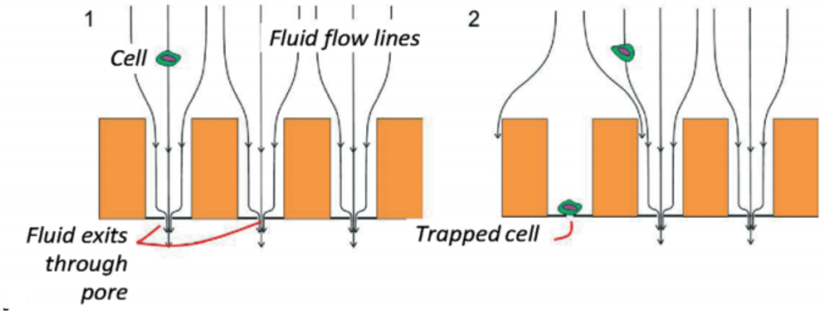

Figure 13: Working principle self-seeding microwell from F. Abali et al (2019).

The importance of the single-cell isolation in wells by flow is shown in Figure 14. However, one can note that the wells without a pore and use gravity sedimentation have a rather successful rate for a low ratio of number of cells / number of wells. This might be a interesting topic if the result printed using inkjet is similar to the results in Figure 11. Moreover, this would mean that no pores have to made and no flow has to be initiated (no airpump, pressure regulation and manometer), simplifying the design tremendously.

4.2.6 Discussion and conclusion

The FACS method is a sensible option if one would look at the commercial market and the technical achievements. However, these cytometry apertures are relative expensive and particularly when combined with high precision placement on the chip, which makes this method not appealing. Though there is a wide variety of single-cell isolation methods, there is only one meeting all the requirements of this research: microfluidics. Not only does this method accommodate room for design changes but the fabrication costs are prodigious compared to the other methods and is prone to iterations in the design phase. Furthermore, a high throughput and high sensitivity is realizable. However, one has to keep in mind that the material used is of paramount importance in the design of the microfluidic system [49]. Consequently, the bacteria might adhere to the chip if the wrong material or a rough surface has been chosen.

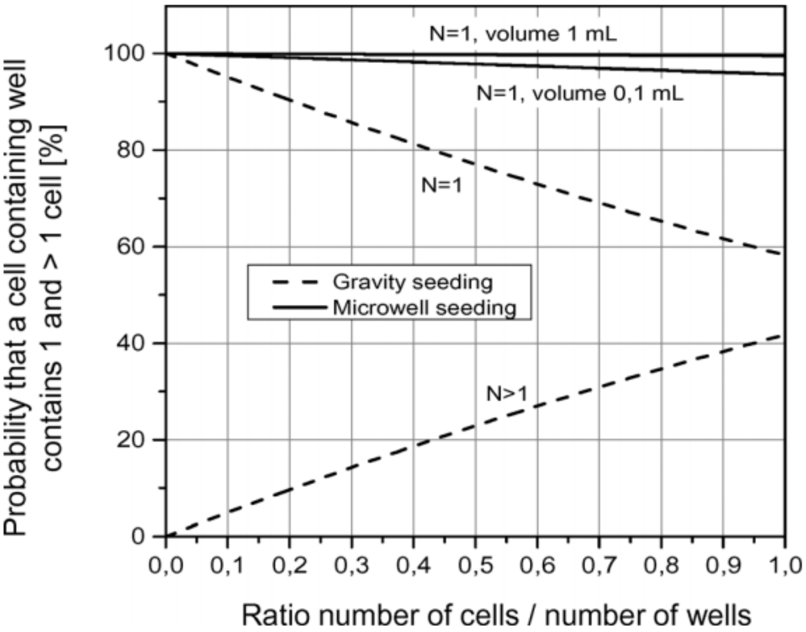

Figure 14: Probability of single cell isolation by sedimentation and self-seeding from F. Abali et al (2019).

4.3 Live imaging

The live tracking of bacteria is a vital step in the process. The recognition of bacteria by an automated system saves time on finding the bacteria under a microscope. If we are talking about single-cell isolation on a few nanodrums on a chip containing hundreds of nanodrums, bacteria recognition through machine learning or edge detection methods could highly increase the momentum of your research.

4.3.1 Machine learning and toolboxes

Microscopes enhanced with artificial intelligence (AI) or more specifically called deep learning, is becoming more relevant as it recognises bacteria quickly and rather accurately. There are several approaches published on this and are based on deep convolutional neural network(CNN). This deep learning strategy uses thousands of training images to create a neural network. These training images consists of (blood) samples with the already identified bacteria by microbiologist. With help of human interaction it is training the algorithm to recognise bacteria reaching over 95% recognition after the training phase without human interaction. A few techniques will be discussed in this section.

A highly effective way of tracking bacteria is using a phase contrast microscope. Currently, the technique has even been extended to 3D tracking. During this approach 3D images are extracted from several 2D images, by varying the angle of the microscope up to 180°. This method compares the out-of-focus diffraction patterns to a reference library and can distinguish different bacteria over 95% accuracy. The working principle is shown in Figure 15, with a vertical slice, horizontal slice from reference, swimming E.coli bacterium and the reconstructed 3D path, respectively [50]. Though for the problem of recognising the bacterium on a nanodrum we are looking at 2D, contract microscopy is a common method used with a high-throughput.

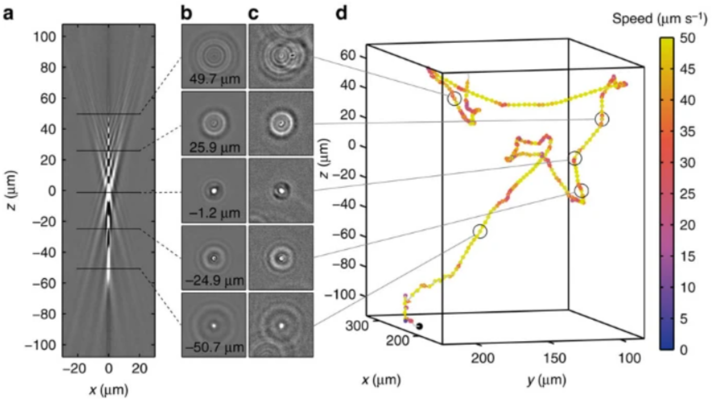

Figure 15: Tracking E.coli bacterium using diffraction patterns from S. Gude et al (2015).

Another commonly used method is based on fluorescent microscopy or staining. This means a fluorescent dye is used to stain a living cell and this specific cell will fluoresce upon irradiation. A good example is shown in Figure 16 ,where 4 different cells are tracked in a well using fluorescent time-lapse imaging microscopy [51]. A. Merouane et al. (2015) also comment on the use of re-segmentation to detect different shapes as fluorescent microscopy is effective for merely the number of cells but not the exact location.

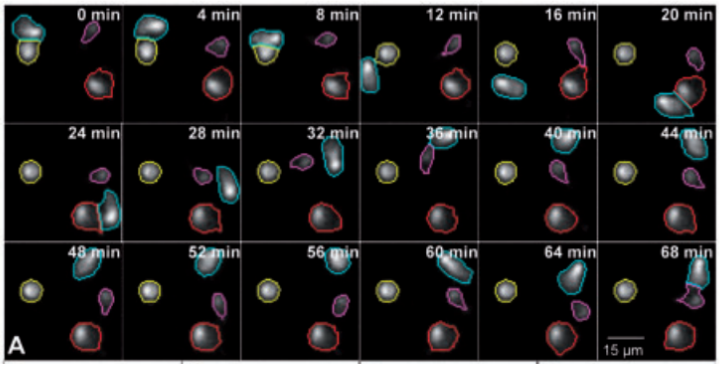

Figure 16: Tracking different bacteria using fluoresecent microscopy and segmentation from A. Merouane et al. (2015).

This method of recognising bacteria using their shapes and sizes has been widely used as well. Smith. et al. (2018) uses this method in combination with CNN to obtain a high accuracy recognition [52]. In this paper over a 100.000 training images were used to recognise different bacteria even in blood samples. The different stages of CNN learning is shown in Figure 17. The first row represents the category known as background, the second the positive grams, the third the cluster of positives and lastly the negative grams. Using this method up to 95% accuracy was achieved.

Segmentation in combination with CNN is getting a rather promising accuracy and hence is combined in multiple toolboxes, which are widely available. MATLAB has some Deep Learning toolboxes but also image segmentation toolboxes [53, 54]. S. Stylianidou et al. uses both these MATLAB toolboxes to recognise bacteria using phase contrast images [55]. The training process is shown in Figure 18.

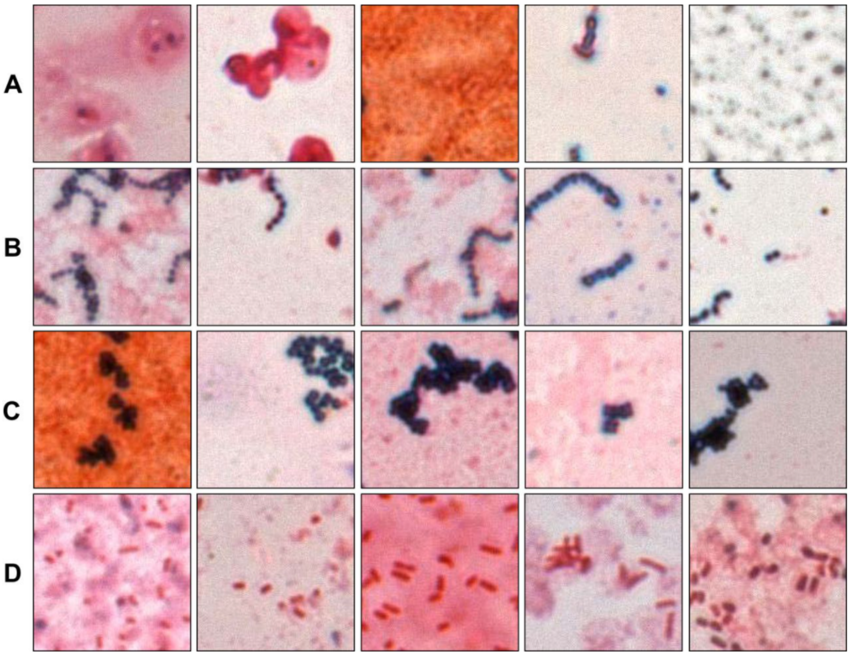

Figure 17: Different categories used in CNN training of blood samples from Smith et al. (2018)

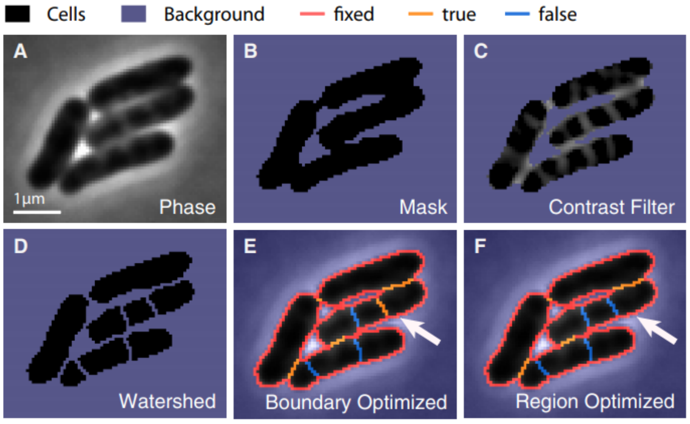

Image segmentation procedure in *SuperSegger*.
E. coli cells are shown as a representative example.
Panel A: Original phase image.
Panel B: Mask of cells using intensity thresholding.
Panel C: Phase image after the contrast (maximum principal curvature) filter and the mask are applied.
Panel D: Boundaries found using the watershed function.
Panel E: Boundaries after the boundary optimization and
Panel F: Boundaries after region optimization. Boundaries are divided into fixed boundaries (red), boundaries that the software classified as true (orange) and false (blue). In Panel E on the right side, there is a boundary incorrectly set as true after boundary optimization which is set to false after region optimization in Panel F.

Figure 18: Image segmentation process of E. coli from S. Stylianidou et al. (2017).

4.3.2 Discussion and conclusion

Literature shows there are multiple plausible approaches to locating single E.coli bacterium on a nanodrum, even extending up to 3D tracking of bacterium. However, in terms of rapid nanomotion detection, fluorescent microscopy is an additional step in the process, increasing the time duration of your experiments. Furthermore, we are looking at bacteria, which are adhered to graphene nanodrums, a 2D image should be enough to locate the bacteria, since the bacteria are not moving. However, the contrast between the nanodrums and the bacteria could be too low for only edge or shape detection to recognise a single bacteria on top of a drum. Moreover, Deep Learning hence might be a must in the locating of a single-cell.

5 Discussion

From the literature review, we can find that there is a need for rapid AST to fight the rise of the antibiotic resistance. There are a lot of different AST techniques available, however by evaluating its sensitivity, accuracy, cost and time consumption, the cantilever techniques are the most promising as discussed in section 2. In recent years the road was paved to extend this research in terms of material, size, shapes and different measurement modes. This slight movement opened doors to exhilarating designs like the suspended graphene nanodrums. Graphene has the characteristics of being fiercely strong and has all carbon atoms located on the surface, making it highly sensitive. In this literature review is looked at different methods to advance this design to a rapid and automated AST.

In subsection 4.1 the use of inkjet printing or printing biomaterial in general was evaluated and found to be a suitable starting point for placement of the bacteria and obtaining a relative small amount of cells. Though this method is prone to time consuming steps in the design phase, such as clogging and cleaning of the nozzle heads, literature shows that once this skill is acquired, a rather quick and precise method is available. Extensively, using a high-end printer like the Pixdro might already be able to print bacteria directly on the drum.

When looking at single-cell isolation methods that are available (subsection 4.2), it was found that the single-cell isolation technique with the most potential for getting a single bacterium at a graphene nanodrum is microfluidics due to its promising features such as high-throughput, simplicity and effectiveness. It is also a low-cost option and can be fabricated relatively easy. Other single-cell isolation methods such as FACS also have a high-throughput and accuracy but were not chosen due to the high-cost and the need for a high-end stage to place a single bacterium on a drum.

Live imaging was described in subsection 4.3. The toolboxes available in MATLAB are perfectly capable of recognising shapes and edges. This means that recognising the graphene nanodrums and the bacteria is not much of a concern. However, having a bacterium on top of a nanodrums might be difficult to detect shapes due to the amount of contrast between the two objects. Deep learning with extensive training should be able to solve this problem.

When all the approaches mentioned above are combined into a low-cost automated process that can be used for a rapid AST, this approach could be used all around the world to help the fight against antibiotic misuse. The current methods for AST are too time consuming and therefore this approach would be a significantly improvement. This means that the AST can be done in a few hours and hence the wrong antibiotic will not be prescribed. Next to being societal relevance, the scientific relevant can be found in opening new doors in the area of AST by moving away from classical cantilevers and combining different single-cell techniques to create a hybrid, intriguing the field of research to look futher than one toolbox.

6 Conclusion

The literature review shows there is knowledge gap in the area of rapid and effective AST. Not per se on the technical aspect, since the technology has been available to do so but merely on the combining of all these different aspects. If an automated AST could be designed that combines high-throughput and single-cell sensitivity, this would be a massive improvements in the field of AST. This design of suspended graphene nanodrums has not been used in the field of nanomotion detection. Therefore, a proposal is made for an automated design that can obtain single-cell sensitivity and rapid measurements. This emerges as a promising yet challenging research topic.

References

[1] Alanis A. J. Resistance to antibiotics: are we in the post-antibiotic era? *Archives of medical research*, 2005.

[2] Rebecca Thayer Horvat. Review of antibiogram preparation and susceptibility testing systems. *Hospital Pharmacy*, 45(11_suppl), 2010.

[3] Leonardo Venturelli, Anne-Céline Kohler, Petar Stupar, Maria I. Villalba, Aleksandar Kalauzi, Ksenija Radotic, Massimiliano Bertacchi, Simone Dinarelli, Marco Girasole, Milica Pešić, Jasna Banković, Maria E. Vela, Osvaldo Yantorno, Ronnie Willaert, Giovanni Dietler, Giovanni Longo, and Sandor Kasas. A perspective view on the nanomotion detection of living organisms and its features. *Journal of Molecular Recognition*, 2020.

[4] A.C. Kohler, L. Venturelli, G. Longo, G. Dietler, and S. Kasas. Nanomotion detection based on atomic force microscopy cantilevers. *The Cell Surface*, 5, 2019.

[5] Ivan Yin, Yunpeng Zhao, C. Lin, H.-H Tsai, Y. Juang, and Gerald Urban. Development of a microfluidic device with microcantilever sensor array for probing single cancer cells mechanics. *2011 16th International Solid-State Sensors, Actuators and Microsystems Conference, TRANSDUCERS'11*, pages 1216–1219, 06 2011.

[6] Sandor Kasas, Francesco Simone Ruggeri, Carine Benadiba, Caroline Maillard, Petar Stupar, Hélène Tournu, Giovanni Dietler, and Giovanni Longo. Detecting nanoscale vibrations as signature of life. *Proceedings of the National Academy of Sciences*, 112(2):378–381, 2015.

[7] J.W.A Rossen et al. A. van Belkum, C.D. Burnham. Innovative and rapid antimicrobial susceptibility testing systems. *Nature Reviews Microbiology*, 18:299–311, 2020.

[8] G. Lüdke et al. A.van Belkum, T.T. Bachmann. Developmental roadmap for antimicrobial susceptibility testing systems. *Nature Reviews Microbiology*, 17:51–62, 2019.

[9] Jungil Choi, Jungheon Yoo, Mincheol Lee, Eun-Geun Kim, Ji Soo Lee, Seungok Lee, Seik Joo, Sang Hoon Song, Eui-Chong Kim, Jung Chan Lee, Hee Chan Kim, Yong-Gyun Jung, and Sunghoon Kwon. A rapid antimicrobial susceptibility test based on single-cell morphological analysis. *Science Translational Medicine*, 6(267):267ra174–267ra174, 2014.

[10] Sixuan Wu Yan Liang Kaixiang Zhang, Shangshang Qin and Jinghong Li. Microfluidic systems for rapid antibiotic susceptibility tests (asts) at the single-cell level. *Chemical science*, 11:6352–6361, 2020.

[11] Webber M. Baylay A. Blair, J. Molecular mechanisms of antibiotic resistance. *Nature Reviews Microbiology*, 13:42–51, 2015.

[12] Khan M. Kaur K. et al. Etayash, H. Microfluidic cantilever detects bacteria and measures their susceptibility to antibiotics in small confined volumes. *Nature communications*, 7, 2016.

[13] Olcum S. Delgado F. et al. Cermak, N. High-throughput measurement of single-cell growth rates using serial microfluidic mass sensor arrays. *Nature biotechnology*, 34:1052–1059, 2016.

[14] Rotem S. Gur D. et al. Zahavy, E. Rapid antibiotic susceptibility determination for yersinia pestis using flow cytometry spectral intensity ratio (sir) fluorescence analysis. *Journal of Fluorescence*, 28:1151–1161, 2018.

[15] ThermoFischer scientific. 2020 attune nxt flow cytometer. Accessed: oktober 2020.

[16] Ferran Pujol-Vila, Rosa Villa, and Mar Alvarez. Nanomechanical sensors as a tool for bacteria detection and antibiotic susceptibility testing. *Frontiers in Mechanical Engineering*, 6, 2020.

[17] Blake N. Johnson and Raj Mutharasan. Biosensing using dynamic-mode cantilever sensors: A review. *Biosensors and Bioelectronics*, 32, 2012.

[18] Ravi Sankar A. Mathew, R. A review on surface stress-based miniaturized piezoresistive su-8 polymeric cantilever sensors. *Nano-Micro Lett.*, 2018.

[19] George Gerald Stoney. The tension of metallic films deposited by electrolysis. *Proc. R. Soc. Lond.*, 1909.

[20] Giovanni Longo, Livan Alonso-Sarduy, Laura Rio, A Bizzini, Andrej Trampuz, J Notz, Giovanni Dietler, and Sandor Kasas. Rapid detection of bacterial resistance to antibiotics using afm cantilevers as nanomechanical sensors. *Nature nanotechnology*, 8, 2013.

[21] A.C. Kohler, L. Venturelli, G. Longo, G. Dietler, and S. Kasas. Nanomotion detection based on atomic force microscopy cantilevers. *The Cell Surface*, 5:100021, 2019.

[22] Amer N. Meyer G. Novel optical approach to atomic force microscopy. *Applied Physics Letters*, 53:2400–2402, 1988.

[23] Hely González-Rivera and G.Eduardo Sandoval-Romero. Nanometric displacement measurement based on interference fringes deflection. *Vibroengineering Procedia*, 11, 2017.

[24] Isaiah David. How do piezoresistive pressure sensors work. Accessed: oktober 2020.

[25] Mohsen Safaei, Henry A Sodano, and Steven R Anton. A review of energy harvesting using piezoelectric materials: state-of-the-art a decade later (2008–2018). *Smart Materials and Structures*, 28(11):113001, oct 2019.

[26] Joan Bausells. Piezoresistive cantilevers for nanomechanical sensing. *Microelectronic Engineering*, 145:9 – 20, 2015.

[27] B. Ilic, D. Czaplewski, M. Zalalutdinov, H. G. Craighead, P. Neuzil, C. Campagnolo, and C. Batt. Single cell detection with micromechanical oscillators. *Journal of Vacuum Science*, 19(6):2825–2828, 2001.

[28] Gossett A. Campbell and Raj Mutharasan. A method of measuring escherichia coli o157:h7 at 1 cell/ml in 1 liter sample using antibody functionalized piezoelectric-excited millimeter-sized cantilever sensor. *Environmental Science & Technology*, 41(5):1668–1674, 2007.

[29] Godin M. Knudsen S. et al. Burg, T. Weighing of biomolecules, single cells and single nanoparticles in fluid. *Nature*, 446:1066–1069, 2007.

[30] H. et al. Etayash. Real-time detection of breast cancer cells using peptide-functionalized microcantilever arrays. *Sci. Rep.*, 5, 2015.

[31] H. Sirringhaus, T. Kawase, R. H. Friend, T. Shimoda, M. Inbasekaran, W. Wu, and E. P. Woo. High-resolution inkjet printing of all-polymer transistor circuits. *Science*, 290(5499):2123–2126, 2000.

[32] Rabbani M. Mohammadi, Z. Bacterial bioprinting on a flexible substrate for fabrication of a colorimetric temperature indicator by using a commercial inkjet printer. *Journal of medical signals and sensors*, 8:170–174, 2018.

[33] Jia Li, Fabrice Rossignol, and Joanne Macdonald. Inkjet printing for biosensor fabrication: Combining chemistry and technology for advanced manufacturing. *Lab on a Chip*, 15, 04 2015.

[34] Tao Xu, Sevastioni Petridou, Eric H. Lee, Elizabeth A. Roth, Narendra R. Vyavahare, James J. Hickman, and Thomas Boland. Construction of high-density bacterial colony arrays and patterns by the ink-jet method. *Biotechnology and Bioengineering*, 85(1):29–33, 2004.

[35] Chuang JS Merrin J, Leibler S. Printing multistrain bacterial patterns with a piezoelectric inkjet printer. *PLoS ONE*, 2, 2007.

[36] Rick Waasdorp, Oscar van den Heuvel, Floyd Versluis, Bram Hajee, and Murali Krishna Ghatkesar. Accessing individual 75-micron diameter nozzles of a desktop inkjet printer to dispense picoliter droplets on demand. *RSC Adv.*, 8:14765–14774, 2018.

[37] Andre Gross, Jonas Schoendube, Stefan Zimmermann, Maximilian Steeb, Roland Zengerle, and Peter Koltay. Technologies for single-cell isolation. *International journal of molecular sciences*, 16:16897–919, 07 2015.

[38] Zhang W. Xin H. Deng G. Hu, P. Single cell isolation and analysis. *Frontiers in cell and developmental biology*, 4, 2016.

[39] Danna E. A. Krutzik P. O. Nolan G. P. Schulz, K. R. Single-cell phospho-protein analysis by flow cytometry. *Current protocols in immunology*, 2012.

[40] Heiby M. Pierobon M. Liotta L. A. Espina, V. Laser capture microdissection technology. *Expert review of molecular diagnostics*, 7:647–657, 2007.

[41] Steven A. Fuller, Miyoko Takahashi, and John G.R. Hurrell. Cloning of hybridoma cell lines by limiting dilution. *Current Protocols in Molecular Biology*, 1(1):11.8.1–11.8.2, 1988.

[42] Johnson E. A. Brehm-Stecher, B. F. Single-cell microbiology: tools, technologies, and applications. *Microbiology and molecular biology reviews*, 68:538–559, 2004.

[43] G. Whitesides. The origins and the future of microfluidics. *Nature*, 442:368–373, 2006.

[44] Eric Brouzes, Martina Medkova, Neal Savenelli, Dave Marran, Mariusz Twardowski, J Hutchison, Jonathan Rothberg, Darren Link, Norbert Perrimon, and Michael Samuels. Droplet microfluidic technology for single-cell high-throughput screening. *Proceedings of the National Academy of Sciences of the United States of America*, 106:14195–200, 08 2009.

[45] Rafael Gómez-Sjöberg, Anne A. Leyrat, Dana M. Pirone, Christopher S. Chen, and Stephen R. Quake. Versatile, fully automated, microfluidic cell culture system. *Analytical Chemistry*, 79(22):8557–8563, 2007.

[46] Dino Di Carlo, Liz Y. Wu, and Luke P. Lee. Dynamic single cell culture array. *Lab on a Chip*, 6:1445–1449, 2006.

[47] Tibbe A. G. Stevens M. Katika M. R. van Dalum J. Tong H. D. van Rijn C. J. Terstappen L. W. Swennenhuis, J. F. Self-seeding microwell chip for the isolation and characterization of single cells. *Lab on a Chip*, 15:3039–3046, 2015.

[48] Fikri Abali, Joska Broekmaat, Arjan Tibbe, Richard B. M. Schasfoort, Leonie Zeune, and Leon W. M. M. Terstappen. A microwell array platform to print and measure biomolecules produced by single cells. *Lab Chip*, 19:1850–1859, 2019.

[49] Kang Ren, Jianhua Zhou, and Hongkai Wu. Materials for microfluidic chip fabrication. *Accounts of chemical research*, 46:2396–2406, 11 2013.

[50] Gude S. Tans S. Shimizu T.S. Taute, K. High-throughput 3d tracking of bacteria on a standard phase contrast microscope. *Nature Communications*, 6:8776, 2015.

[51] Amine Merouane, Nicolas Rey-Villamizar, Yanbin Lu, Ivan Liadi, Gabrielle Romain, Jennifer Lu, Harjeet Singh, Laurence J.N. Cooper, Navin Varadarajan, and Badrinath Roysam. Automated profiling of individual cell–cell interactions from high-throughput time-lapse imaging microscopy in nanowell grids (TIMING). *Bioinformatics*, 31(19):3189–3197, 06 2015.

[52] Kenneth P. Smith, Anthony D. Kang, and James E. Kirby. Automated interpretation of blood culture gram stains by use of a deep convolutional neural network. *Journal of Clinical Microbiology*, 56(3), 2018.

[53] Mathworks. Deep learning with images. Accessed: november 2020.

[54] Mathworks. Detect cell using edge detection and morphology. Accessed: november 2020.

[55] Stella Stylianidou, Connor Brennan, Silas B. Nissen, Nathan J. Kuwada, and Paul A. Wiggins. Supersegger: robust image segmentation, analysis and lineage tracking of bacterial cells. *Molecular Microbiology*, 102(4):690–700, 2016.

A Timeline

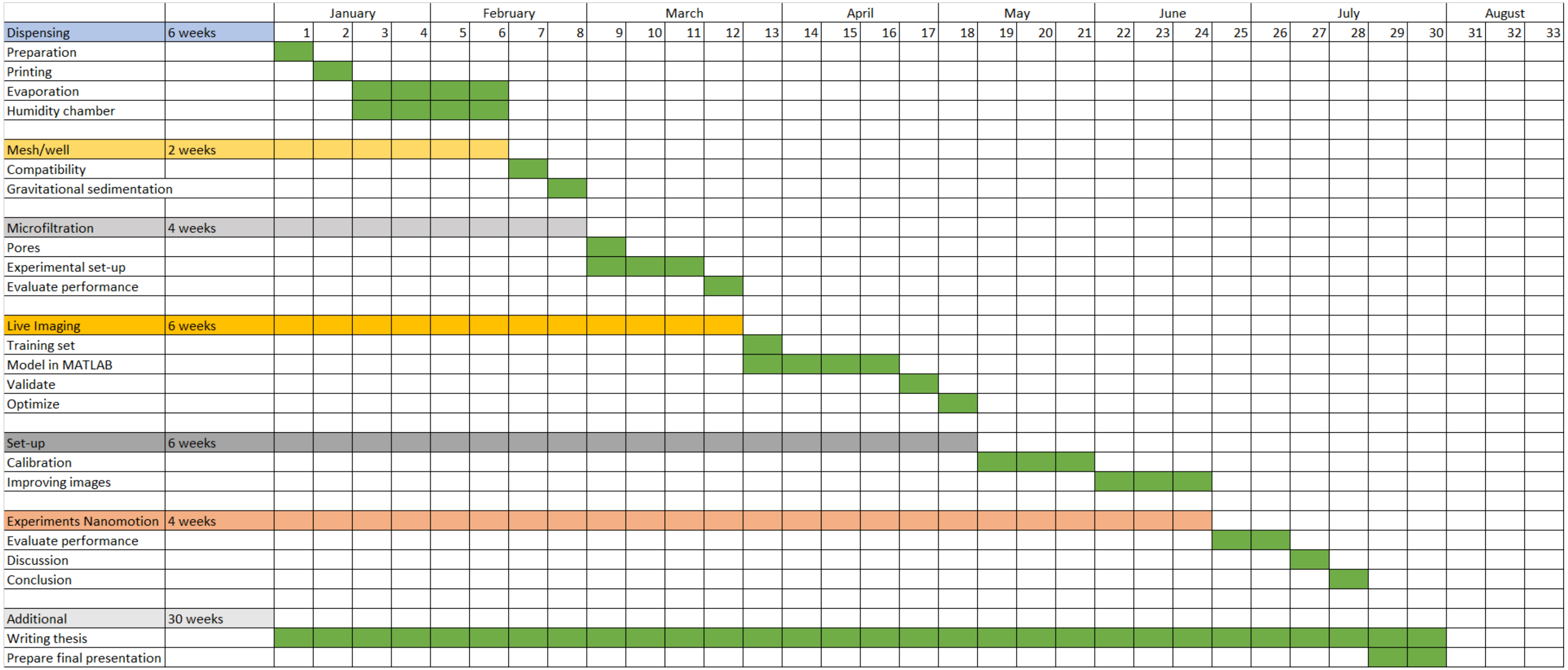

		January				February				March					April				May				June				July					August		
Dispensing	6 weeks	1	2	3	4	5	6	7	8	9	10	11	12	13	14	15	16	17	18	19	20	21	22	23	24	25	26	27	28	29	30	31	32	33
Preparation		🟩																																
Printing			🟩																															
Evaporation				🟩	🟩	🟩	🟩																											
Humidity chamber				🟩	🟩	🟩	🟩																											
Mesh/well	2 weeks	▨	▨	▨	▨	▨	▨																											
Compatibility								🟩																										
Gravitational sedimentation									🟩																									
Microfiltration	4 weeks	▨	▨	▨	▨	▨	▨	▨	▨																									
Pores										🟩																								
Experimental set-up										🟩	🟩	🟩																						
Evaluate performance													🟩																					
Live Imaging	6 weeks	▨	▨	▨	▨	▨	▨	▨	▨	▨	▨	▨	▨																					
Training set														🟩																				
Model in MATLAB														🟩	🟩	🟩	🟩																	
Validate																		🟩																
Optimize																			🟩															
Set-up	6 weeks	▨	▨	▨	▨	▨	▨	▨	▨	▨	▨	▨	▨	▨	▨	▨	▨	▨	▨															
Calibration																				🟩	🟩	🟩												
Improving images																							🟩	🟩	🟩									
Experiments Nanomotion	4 weeks	▨	▨	▨	▨	▨	▨	▨	▨	▨	▨	▨	▨	▨	▨	▨	▨	▨	▨	▨	▨	▨	▨	▨	▨									
Evaluate performance																										🟩	🟩							
Discussion																												🟩						
Conclusion																													🟩					
Additional	30 weeks																																	
Writing thesis		🟩	🟩	🟩	🟩	🟩	🟩	🟩	🟩	🟩	🟩	🟩	🟩	🟩	🟩	🟩	🟩	🟩	🟩	🟩	🟩	🟩	🟩	🟩	🟩	🟩	🟩	🟩	🟩	🟩	🟩			
Prepare final presentation																														🟩	🟩			

Figure 19: Timeline for the rest of the thesis.

COLOPHON

This document was typeset using LaTeX. The document layout was generated using the arsclassica package by Lorenzo Pantieri, which is an adaption of the original classicthesis package from André Miede.